Electric Field Control of Magnetic Properties in Multiferroic Heterostructures

Wei-Gang Yang

Thesis submitted for the degree of

Doctor of Philosophy

January 2016

Department of Materials Science and Engineering

The University of Sheffield

Abstract

Recently, the use of an electric field (E-field) to control the magnetic properties of thin magnetic films has drawn intensive interest due to their important potential applications such as magnetoelectric random access memory (MERAM) devices and magnetoelectric (ME) sensor.

In this thesis, the work first includes a study of the strain-mediated ME coupling strength manipulation by either changing ferromagnetic layer thickness (30-100 nm) or inserting a thin Ti buffer layer (0-10 nm). A large remanence ratio (M_r/M_s) tunability of 95% has been demonstrated in the 65 nm CoFe/PMN-PT heterostructure, corresponding to a giant ME constant (α) of 2.5×10^{-6} s/m, when an external E-field of 9 kV/cm was applied. Also, a record high remanence ratio (M_r/M_s) tunability of 100% has been demonstrated in the 50 nm CoFe/8 nm Ti/PMN-PT heterostructure, corresponding to a large ME constant α of 2.1×10^{-6} s/m, when the E-field of 16 kV/cm was applied. Furthermore, the E-field induced magnetic response was repeatable and quick even after 30 repeats were made.

Secondly, a study of non-volatile magnetization change has been demonstrated in the 65 nm CoFe/24 nm Metglas/PMN-PT. In this heterostructure, the E-field created two new non-volatile remanence states, although the as-grown magnetic anisotropy was altered permanently, when the E-field between -6 kV/cm to +6 kV/cm was applied. Based on giant magnetoresistance (GMR) or anisotropic magnetoresistance (AMR), the MERAM memory cell was proposed for the fast, low-power and high-density information storage.

Publications and Presentations

The work in this thesis has been published on international journals [1–4] and presented in conferences [5,6] as follows:

[1] **Yang W-G**, Morley N A, Sharp J, Tian Y and Rainforth W M 2016 Strain-mediated converse magnetoelectric coupling strength manipulation by a thin titanium layer *Appl. Phys. Lett.* 108 012901

[2] **Yang W-G**, Morley N A and Rainforth W M 2015 Electric field-controlled magnetization in bilayered magnetic films for magnetoelectric memory *J. Appl. Phys.* 118 034102

[3] **Yang W-G**, Morley N A, Sharp J and Rainforth W M 2015 Giant electric field tunable magnetic properties in a $Co_{50}Fe_{50}$/lead magnesium niobate–lead titanate multiferroic heterostructure *J. Phys. D. Appl. Phys.* 48 305005

[4] Morley N A, Finkel A C, **Yang W** and Reeves-mclaren N 2014 Magnetic and Structural Characterization of NiFe/$Fe_{30}Co_{70}$ Bilayers *IEEE Trans. Magn.* 50 2503704

[5] 2015 Institute of Physics Magnetism (Leeds, UK)

[6] 2013 Postgraduate Magnetism Techniques Workshop (York, UK)

Acknowledgements

Above all, I would very much like to sincerely appreciate my two supervisors: Prof. W Mark Rainforth and Dr. Nicola A Morley for all their support and guidance throughout my PhD research period. I am also really grateful for their valuable time and efforts on the discussion and correction of three published papers. Here, I would also like to thank Prof. M. R. J. Gibbs for his help in my first year of PhD study.

Here, I would like to thank the whole magnetics group, SCAMMD, for providing me with a fantastic experimental conditions and research environment. I would like to thank everyone in this warm big family for your memorable accompanies and firm support. Especially, I would like to thank Prof. Dan Allwood and Dr. Tom Hayward for their valuable suggestions on my projects. In addition, I also especially thank Dr. Matthew Hodges, Dr. James Wheelwright, Miss Ruth Bradley and Mr Jonathan Wood for their help on both my study and life in Sheffield, UK.

I would like to thank the related technical staffs in the department of Materials Science and Engineering, Sorby Centre and Nanoscience and Technology Centre for their training on the experimental facilities. I would also like to thank Dr. Joanne Sharp and Dr. Tian Ye for their help with transmission electron microscopy (TEM) imaging on a JEOL R005 and piezoelectric strain measurements, respectively.

I would like to thank my family members for their supporting and understanding in my PhD study period. Especially, I would like to express my most sincere gratitude to my wife for her selfless dedication to this family. I would not have been able to achieve what I have now without her efforts during my three years. I would also like to thank my daughter Emma Yang for giving me happiness during my tough time.

List of Symbols

T_c	Curie temperature
E_e	Exchange energy
E_{zeeman}	Zeeman Energy
H_d	Demagnetizing field
E_{ms}	Magnetostatic energy
N_d	Demagnetizing factor
E_{mc}	Magnetocrystalline anisotropy energy
K	Anisotropy constant
E_{me}	Magnetoelastic energy
E_{charge}	Charging induced surface anisotropy energy
E_{uni}	Uniaxial magnetic anisotropy energy
H	Magnetic field
M	Magnetization
M_s	Saturation magnetization
M_r	Remanant magnetization
H_c	Coercive field
H_s	Saturation field
H_k	Anisotropy field
H_{keff}	Effective anisotropy field
E	Electric field
d_{ij}	Piezoelectric constant
σ	Stress

ε	Strain
P	Electric polarization
Y	Young's modulus
ν	Poisson's ratio
α	Magnetoelectric coupling constant

Contents

Chapter 1

1 Introduction

Recently, the use of an electric field (E-field) to control the magnetic properties in multiferroic (MF) materials [1] (Converse magnetoelectric effect, CME [2]) rather than a magnetic field (H-field) generated by a current [3] or the current itself [4] has drawn intensive interest due to their important potential applications such as magnetoelectric random access memory (MERAM) devices [5–8] and magnetoelectric sensor [9,10].

Single phase MF materials are rare in nature [11] and almost all of them show only a weak magnetoelectric (ME) coupling below room temperature [2]. Therefore, most research has focused on MF composites [12,13]. Many papers have reported the strain-induced magnetization changes in a wide range of the MF layered composites (ferromagnetic (FM) films/ferroelectric (FE) substrates) such as Fe-Ga/(110) PMN-PT (lead magnesium niobate-lead titanate) [14], CoFe/PMN-PT [15], $Ni_{80}Co_{20}$/(110) PZN-PT (lead zinc niobate-lead titanate) [16], FeGaB/(110) PZN-PT [17], FeGaB/(110) PMN-PT [18], Fe_3O_4/PZN-PT [19], $NiFe_2O_4$/(001) PMN-PT [20], $Fe_{50}Co_{50}$-Hf/PZN-PT [21] and Ni/(110) PMN-PT [22]. Large magnetization changes were induced by an external E-field in these systems, as shown in **Fig. 1.1**. This provides great opportunities for E-field controlling magnetic devices.

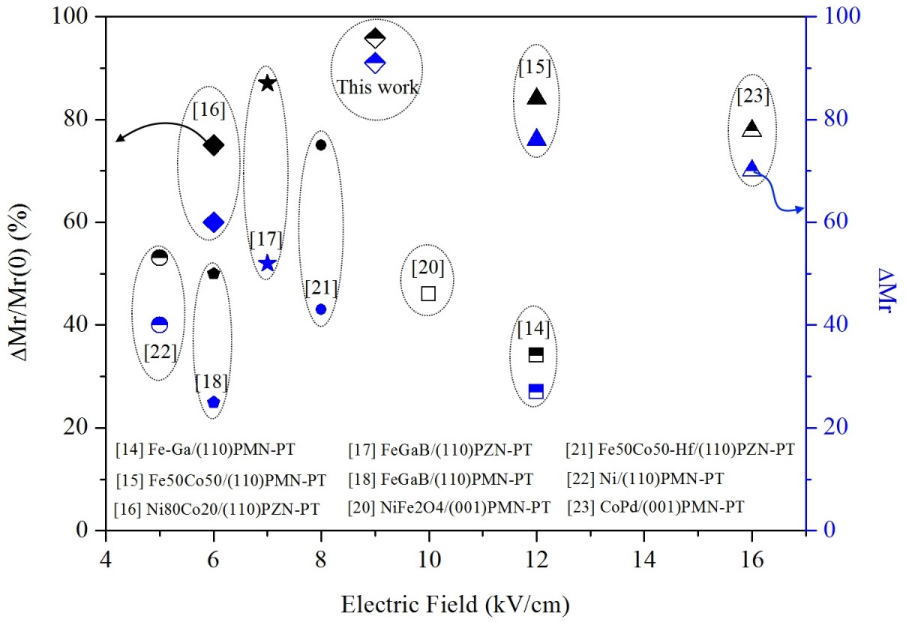

Fig. 1.1 A comparison and contrast of the E-field induced the normalized remanent magnetization (ΔM_r) (blue symbols) and the relative remanent magnetization (black symbols) change in some already published papers and that in this thesis. Here, the normalized $\Delta M_r = M_r/M_s\ (E) - M_r/M_s\ (0)$ and $\Delta M_r/M_r(0) = [M_r/M_s\ (E) - M_r/M_s\ (0)]/\ M_r/M_s\ (0)$.

The manipulation of ME coupling strength has been investigated in MF composites has yet to be studied extensively. Kim et al. [23] tried to manipulate ME coupling strength by varying the composition and thickness of the Co_xPd_{1-x} film with an out of plane anisotropy. A large ME coupling strength was found for 10 nm $Co_{0.25}Pd_{0.75}$ film due to a high magnetostriction. However, ME coupling strength can be improved further. In this thesis, the ME coupling strength was manipulated by either changing ferromagnetic layer thicknesses or inserting a thin Ti buffer layers. A record high remanance ratio (M_r/M_s) tunability of 100% was demonstrated in a 50nm CoFe/8nm Ti/PMN-PT heterostructure, corresponding to a large ME constant α of 2.1×10^{-6}s/m, when an E-field of 16kV/cm was applied.

Magnetoelectric random access memory (MERAM), i.e., E-field controlled magnetic random access memory (MRAM) [24] has been proposed to drastically reduce the write energy in the recording process, which is important for further miniaturization. However, so far, most magnetization and magnetic anisotropy changes induced by the E-field are volatile. In other words, the magnetization returns to its initial state after the E-field is removed. This is clearly not practically useful for novel memory and logic device applications. Non-volatile magnetization changes induced by the E-field have been demonstrated in multiferroic heterostructures with single layer magnetic films [22,25–28]. However, E-field-controlled non-volatile magnetization changes in bilayered magnetic films have not been studied. In this thesis, non-volatile magnetization changes were demonstrated in a 65nm CoFe/24nm Metglas/PMN-PT heterostructure.

1.1 Thesis outline

This thesis includes eight chapters, which are briefly introduced as follows:

Chapter 2 introduces the basic theory related to this project, with a particular focus on the magnetic energies and the effect of elastic strain on domain wall motion.

Chapter 3 reviews the research progress on multiferroic material fabrication, mechanism studies and practical applications in the past few decades. Some challenges in the future are also identified.

Chapter 4 introduces the main experimental techniques used in this project. It includes sample preparation, microstructural characterization and magnetic characterization.

Chapter 5, 6 and 7 are three experimental chapters.

Chapter 5 studies the effect of magnetic layer thickness on the ME coupling strength. The ME constant α has been improved obviously by reducing the magnetic layer thickness in multiferroic heterostructures.

Chapter 6 demonstrates a non-volatile magnetization change induced by the E-field in multiferroic heterostructures with bilayered magnetic films.

Chapter 7 investigates the effect of buffer layer thickness on the ME coupling strength. A record high remanance ratio (M_r/M_s) tunability of 100% has been obtained in a 50 nm CoFe/8 nm Ti/PMN-PT heterostructure.

Chapter 8 summarizes this thesis and also proposes some future work.

1.2 References

[1] W. Eerenstein, N.D. Mathur, J.F. Scott, Nature 442 (2006) 759–765.

[2] J. Ma, J.M. Hu, Z. Li, C.W. Nan, Adv. Mater. 23 (2011) 1062–1087.

[3] G.A. Prinz, Science 282 (1998) 1660–1663.

[4] E.B. Myers, D.C. Ralph, J.A. Katine, R.N. Louie, R.A. Buhrman, Science 285 (1999) 867–870.

[5] X. Chen, A. Hochstrat, P. Borisov, W. Kleemann, Appl. Phys. Lett. 89 (2006) 202508.

[6] J.M. Hu, Z. Li, L.Q. Chen, C.W. Nan, Nat. Commun. 2 (2011) 553.

[7] M. Bibes, A. Barthélémy, Nat. Mater. 7 (2008) 425–426.

[8] J.M. Hu, Z. Li, L.Q. Chen, C.W. Nan, Adv. Mater. 24 (2012) 2869–2873.

[9] J.Y. Zhai, Z.P. Xing, S.X. Dong, J.F. Li, D. Viehland, Appl. Phys. Lett. 88

(2006) 062510.

[10] C. Israel, N.D. Mathur, J.F. Scott, Nat. Mater. 7 (2008) 93–94.

[11] N.A. Hill, J. Phys. Chem. B 104 (2000) 6694–6709.

[12] G. Srinivasan, Annu. Rev. Mater. Res. 40 (2010) 153–178.

[13] C. Nan, Phys. Rev. B 50 (1994) 6082–6088.

[14] Y. Zhang, Z. Wang, Y. Wang, C. Luo, J. Li, D. Viehland, J. Appl. Phys. 115 (2014) 084101.

[15] T.L. Jin, L. Hao, J.W. Cao, M.F. Liu, H.G. Dang, Y. Wang, D.P. Wu, J.M. Bai, F.L. Wei, Appl. Phys. Express 7 (2014) 043002.

[16] M. Liu, S.D. Li, O. Obi, J. Lou, S. Rand, N.X. Sun, Appl. Phys. Lett. 98 (2011) 222509.

[17] M. Liu, Z.Y. Zhou, T.X. Nan, B.M. Howe, G.J. Brown, N.X. Sun, Adv. Mater. 25 (2013) 1435–1439.

[18] J. Lou, D. Reed, C. Pettiford, M. Liu, P. Han, S. Dong, N.X. Sun, Appl. Phys. Lett. 92 (2008) 262502.

[19] M. Liu, O. Obi, J. Lou, Y.J. Chen, Z.H. Cai, S. Stoute, M. Espanol, M. Lew, X. Situ, K.S. Ziemer, V.G. Harris, N.X. Sun, Adv. Funct. Mater. 19 (2009) 1826–1831.

[20] J.H. Park, Y.K. Jeong, S. Ryu, J.Y. Son, H.M. Jang, Appl. Phys. Lett. 96 (2010) 192504.

[21] S. Li, M. Liu, W. Shao, J. Xu, S. Chen, Z. Zhou, T. Nan, N.X. Sun, J.-G. Duh, J. Appl. Phys. 113 (2013) 17C727.

[22] T. Wu, A. Bur, P. Zhao, K.P. Mohanchandra, K. Wong, K.L. Wang, C.S. Lynch, G.P. Carman, Appl. Phys. Lett. 98 (2011) 012504.

[23] J.H. Kim, K.S. Ryu, J.W. Jeong, S.C. Shin, Appl. Phys. Lett. 97 (2010) 252508.

[24] C. Chappert, A. Fert, F.N. Van Dau, Nat. Mater. 6 (2007) 813–823.

[25] J.W. Lee, S.C. Shin, S.K. Kim, Appl. Phys. Lett. 82 (2003) 2458–2460.

[26] A. Brandlmaier, S. Geprägs, G. Woltersdorf, R. Gross, S.T.B. Goennenwein, J. Appl. Phys. 110 (2011) 043913.

[27] Z. Li, J. Wang, Y. Lin, C.W. Nan, Appl. Phys. Lett. 96 (2010) 162505.

[28] S.W. Yang, R.C. Peng, T. Jiang, Y.K. Liu, L. Feng, J.J. Wang, L.Q. Chen, X.G. Li, C.W. Nan, Adv. Mater. 26 (2014) 7091–7095.

Chapter 2

2 Theoretical Background

2.1 Magnetism and Magnetic Materials

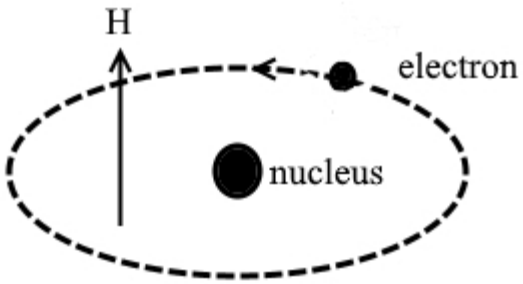

Fig. 2.1 Schematic of the origin of magnetism from the electronic structure in a free atom.

The origin of magnetism is first understood in a free atom that has a magnetic dipole moment [1] even without an external magnetic field. This can be attributed to the electronic structure existing in the free atom [2], as shown **Fig. 2.1**. Firstly, unpaired electrons circulating the nucleus in the atomic orbitals have orbital angular momenta, which create the atomic magnetic moment. This is similar to the circulating currents made from charged particles producing a magnetic field. Secondly, each individual electron has an angular momentum, which also creates the "spin" magnetic moment. Moreover, both magnetic moments, as a result of electrons orbital motion and spin themselves respectively, can be coupled, which is called spin-orbit coupling [2]. The coupling also includes orbit-orbit coupling and spin-spin coupling among electrons,

which give a total atomic magnetic moment. After understanding the atomic origin of the magnetism, the next focus is on the magnetic materials, although only brief introduction is made except for ferromagnetic materials.

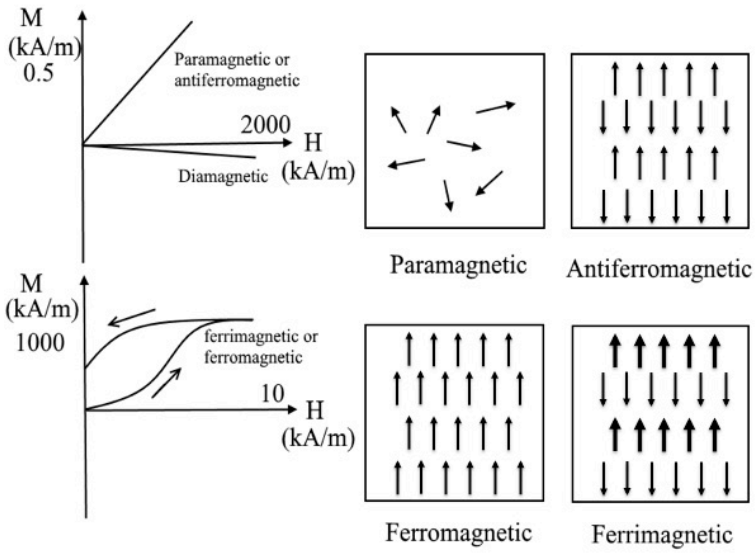

Fig. 2.2 Schematic magnetization curves and magnetic orderings for magnetic materials

Diamagnetic materials refer to the materials only exhibiting a diamagnetic response when an external magnetic field is applied. In fact, all materials exhibit a weak diamagnetic response but some magnetic materials possess a stronger magnetic response to the field. Diamagnetic materials do not have a net atomic magnetic moment (i.e. total magnetic moment is zero) due to either completely filled or empty atomic orbitals. The induced magnetic moment in the atom is created by electromagnetic induction and opposes the applied magnetic field (**Fig. 2.2**). When the field is removed, the net magnetic moment returns to zero. Therefore, diamagnetic materials do not have a wide range of applications due to their lack of the permanent magnetic moment. Different from diamagnetic materials,

paramagnetic materials have the net atomic magnetic moments but these magnetic moments only have very weak interaction, thus all the moments have a random arrangement due to thermal agitations (**Fig. 2.2**). When an external field (1000 kA/m) is applied, only a weak magnetization (0.5 kA/m) occurs. Similarly, paramagnetic materials do not have the wide range of applications. Ferromagnetic and ferrimagnetic materials at temperatures above the Curie temperature (T_c) will become paramagnetic [3].

Fortunately, ferromagnetic materials have a wide range of applications in modern device technologies. Firstly, the large magnetization strength (~ 1000 kA/m) can be achieved even under the effect of the small field (~ few kA/m), which is as a consequence of the strong interactions between atomic magnetic moments. The strong internal interactions overcome the thermal energy effects and align the magnetic moments parallel to each other, which produces a spontaneous magnetization even in the absence of an external magnetic field [4]. Moreover, the spontaneous magnetization tends to point to some preferred directions, which is associated with the magnetocrystalline anisotropy (further information will be given on the magnetocrystalline energy introduction in section 2.2.3). Secondly, the ferromagnetic magnetization shows a hysteresis characterization (**Fig. 2.2**), which means that the magnetization can fully or partly remain even when the field is removed completely. This provides great opportunities for information storage applications. The reason can be understood based on domain theory (see section 2.3.1) and the magnetization process (see section 2.3.2).

Two other forms of magnetic materials are antiferromagnetic materials and ferrimagnetic materials. Both of them have the spontaneous magnetization, which is

similar to the ferromagnetic materials. However, strong internal interactions between magnetic moments arrange adjacent moments antiparallel to each other. In antiferromagnetic materials, the spontaneous magnetization is completely cancelled out due to opposite directions having the same total magnetic moments. Therefore, in antiferromagnets, the net spontaneous magnetization is zero. They show a similar linear magnetization relationship against the external field as paramagnets. In ferrimagnetic materials, although the part of the spontaneous magnetization is also cancelled out from magnetic moments in opposite directions, one direction moment is larger than the other direction, hence they have an overall magnetization. Ferrimagnetic materials have similar magnetization behaviour (i.e. magnetic hysteresis characterization, as shown in **Fig. 2.2**) to ferromagnetic materials.

2.2 Magnetic Energy

In section 2.1, a brief introduction about the magnetic materials has been made. It is seen that ferromagnetic materials possess a strong magnetization compared to the other forms of magnetism and has magnetic hysteresis characterization, which allows them to have a wide range of applications. In this section, magnetic energy is introduced for the ferromagnetic system, as it is important to understand spontaneous magnetization, the formation of domains and the domain wall structure, along with magnetic anisotropy.

2.2.1 Exchange Energy

As mentioned in section 2.1, the exchange interaction between atomic magnetic moments aligns them parallel to each other so that the exchange energy (E_e) is minimized. In equation 2.1, E_e refers to the energy between all nearest neighbouring magnetic moment pairs in a unit volume [5].

$$E_e = -J\vec{S_i}.\vec{S_j} \tag{2.1}$$

where J is the exchange constant and. $\vec{S_i}$ and $\vec{S_j}$ are the spin vectors. It is seen that when the magnetic moments are parallel to each other, the E_e will reach the minimal value. When the ferromagnetic system is solely determined by the exchange energy, all magnetic dipoles will be aligned into the same direction. However, within a magnetic material the moments will not be always be parallel due to several different forms of energy that compete with each other and finally determine the magnetic system.

2.2.2 Magnetostatic Energy

Firstly, the concept of demagnetizing field (H_d) is introduced here. A magnetic field produced by a magnetized magnet will exert a field on the magnet in the opposite direction from its own magnetization, thus the magnetic field is known as the demagnetizing field. The demagnetizing field causes the magnetostatic energy (E_{ms}). The E_{ms} per unit volume is calculated by the equation [6]:

$$E_{ms} = \frac{1}{2}\mu_0 H_d M \tag{2.2}$$

where the M is the magnetization. A larger demagnetizing field will give a larger magnetostatic energy. The demagnetizing field H_d is proportional to the magnitude of the magnetization M, given by the equation [2]:

$$H_d = -N_d M \tag{2.3}$$

where the N_d is demagnetizing factor, which is determined by the sample geometry (the ratio of long axis and short axis). The N_d is ≤ 1 for all geometries. In terms of a two-dimension object, the demagnetizing factor N_d along a short axis is larger than

along the long axis. As a result the demagnetizing field H_d is larger along a short axis. For a three-dimension object, there are N_{dx}, N_{dy} and N_{dz} along three directions respectively and also $N_{dx} + N_{dy} + N_{dz} = 1$. The equation (1.2) can be rewritten in terms of N_d:

$$E_{ms} = \frac{1}{2}\mu_0 N_d M^2 \tag{2.4}$$

The short axis will have a higher E_{ms}, thus the magnetization more likely to lie along the long axis, as it has the lower E_{ms}. Thus the short axis known as the hard axis and the long axis known as the easy axis when the shape anisotropy is dominant in a magnetic system. For example, in a film system, the easy magnetization direction is within the film plane while the hard magnetization direction is normal to the film plane due to the large shape anisotropy.

For a prolate rod shape, the E_{ms} is given [6]:

$$E_{ms} = K_s \sin^2\theta + \cdots \tag{2.5}$$

where K_s is the shape anisotropy constant and θ is the angle between the magnetization direction and the semi-major axis c of the rod. When the semi-major axis equals the semi-minor axis, the K_s is zero and the shape anisotropy disappears.

2.2.3 Magnetocrystalline Energy

In ferromagnetic single crystals, the magnetization prefers to be along one crystallographic direction, i.e. (100) or (111), which is known as the easy axis. When an external magnetic field is applied along this direction, it is easy to saturate the magnetization. This means that for the other crystallographic directions, it requires a larger magnetic field for a saturate state to be reached. The crystallographic direction which requires the largest field to saturate is the hard axis, while the other directions

are the intermediate axis. For example, for body centered cubic (bcc) iron, the easy directions are six cube edge orientations, i.e. [100], [010], [001], [-100], [0-10] and [00-1] [2], while the hard directions are four body diagonal orientations, i.e. [111], [-111], [1-11] and [11-1]. For the different ferromagnetic materials, the preferred crystallographic direction can be different, for example face centered cubic (fcc) Ni easy direction is [111]. The anisotropy associated with the crystal structure is called magnetocrystalline anisotropy. The magnetocrystalline anisotropy energy [2] (E_{mc}) is defined as the energy difference between energy required to saturate along the easy axis and the energy required to saturate along the hard axis. The anisotropy energy also refers to the energy, which overcomes the magnetocrystalline anisotropy and moves the magnetization away from the easy direction. In cubic crystals such as iron, the E_{mc} can be given [2]:

$$E_{mc} = K_1(\alpha_1^2\alpha_2^2 + \alpha_2^2\alpha_3^2 + \alpha_3^2\alpha_1^2) + K_2(\alpha_1^2\alpha_2^2\alpha_3^2) + \cdots \quad (2.6)$$

Where K_1 and K_2 are the anisotropy constants and α_i is a series of the direction cosines between the magnetization direction and the crystal axis.

For a uniaxial anisotropy energy in hexagonal crystals such as Cobalt (Co), the E_{mc} can be given [2]:

$$E_{mc} = K_0 + K_1\sin^2\theta + K_2\sin^4\theta + \cdots \quad (2.7)$$

where K_0, K_1 and K_2 are the anisotropy constants and θ is the angle between the magnetization vector and the magnetocrystalline easy axis.

2.2.4 Magnetoelastic Energy

Magnetoelastic energy is also called magnetostrictive energy, which arises from the magnetostriction effect. Basically, the magnetostriction [7] effect refers to the

change in length of a ferromagnetic material that occurs when an external magnetic field is applied. Materials such as Fe have a positive magnetostriction, i.e. elongating along the magnetic field direction, whereas other materials such as Ni have a negative magnetostriction, i.e. contracting along the magnetic field direction. The change in length is small, around tens of parts per million (ppm). In ferromagnetic systems, there are many different orientation domains (see section 2.3.1). Moreover, they tend to elongate or contract along the different directions, which are unable to occur at the same time and thus the system creates the magnetoelastic energy. In addition, an external stress can induce a change in the magnetoelastic energy, which can dominate the magnetization process. This is the important reason why a piezoelectric strain induced by an electric field can control the magnetization in ferromagnetic films. More detailed statement will be exhibited in section 2.3.3. The magnetoelastic energy (E_{me}) is given by [6]

$$E_{me} = -\frac{3}{2}\lambda_s \sigma \cos^2\theta \tag{2.8}$$

where λ_s is the saturation magnetostriction constant, σ is the external stress, and θ is the angle between the saturation magnetization (M_s) and the stress (σ).

2.3 Magnetization in Ferromagnets

2.3.1 Magnetic Domains and Domain Walls

To understand the magnetization process in ferromagnetic materials, the origin of ferromagnetic domains and domain walls [8] have to be introduced. In ferromagnetic materials the small regions where all the atomic magnetic dipoles have a parallel alignment to each other [2] are known as ferromagnetic domains. The overall magnetization direction varies from a domain to another domain [9]. The formation

of domains occurs to minimize the total magnetic energy within a ferromagnet. Although the domain structure in the ferromagnet increases the exchange energy due to the unparallel magnetic moment alignment between the domains, it significantly decreases the magnetostatic energy (see section 2.2.2) due to the reduced demagnetizing field. Thus, the total magnetic energy in the system is lowered. The boundary (like a grain boundary) or transition area between two adjacent domains is called a domain wall. The formation of domain walls is determined by a compromise between the different magnetic energy contributions. A wide domain wall will reduce the exchange energy contribution as there is a gradual change between each magnetic moment rather than a sharp transition. For example, a 180^o domain wall will have the magnetic moments rotate gradually from 0^o to 180^o. But, the wide domain wall will also increase the magnetocrystalline energy (see section 2.2.3) contribution due to more magnetic moments not along the preferred crystallographic directions (i.e. easy axis). Conversely, a narrow wall will increase the exchange energy but decrease the magnetocrystalline energy, thus the total energy is optimized between the two energies.

2.3.2 Magnetization process

Briefly, the magnetization process involves both domain wall motion and domain rotation, which can occur simultaneously by an external magnetic field at any level of the magnetization (M). But, a rough division [6] is that the domain wall motion predominates when the magnetization is far away from saturate magnetization (M_s) or close to zero magnetization while the domain rotation predominates when the magnetization is close to saturation. The description below of the magnetization process is based on this.

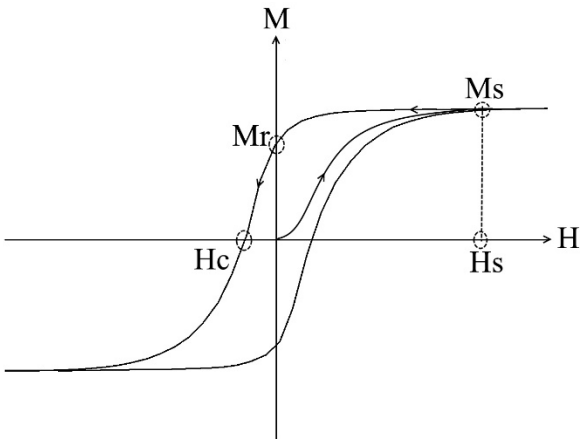

Fig. 2.3 Magnetic hysteresis loop for a ferromagnet.

Initially, in the demagnetized state at zero applied field, all domains are arranged randomly and the total magnetization is cancelled to zero. When the magnetic field is applied, the domain walls start to move so that some domains grow, which are those in which the spontaneous magnetization is nearest to the applied field direction. As a result, the other domains whose spontaneous magnetization is not close to the applied field direction become smaller and smaller. During the motion process, the domain wall can come across defects in the material, which results in domain wall pinning [9]. The external field has to provide the domain walls motion with the energy to overcome the pinning sites. Once the domain walls are separated, a sharp change in the magnetization occurs due to a discontinuous domain wall motion. Then, as the field keeps increasing, eventually it will eliminate all domain walls, thus it ends up with a single domain within the material. Further increasing the magnetic field to saturate field (H_s) causes the magnetic moments in the single domain to rotate from the magnetization easy axis to the applied field direction hence the magnetization reaches saturation (M_s). When the magnetic field is removed, the magnetic moments rotate back to their initial easy magnetization direction due to the

magnetocrystalline anisotropy. However, the domain walls do not always move back to their initial positions because the demagnetizing field is not sufficient to overcome the energy barrier encountered by the domain walls due to the defects in material. Thus a remanent magnetization state (M_r) is reached. Therefore, the magnetization exhibits a hysteresis characterization, as shown in **Fig. 2.3**. For reducing the magnetization to zero, a magnetic field in the opposite direction (i.e. coercive field, H_c) has to be applied.

2.3.3 The effects of elastic stress

In section 2.2.4, the magnetoelastic energy was introduced. If the magnetoelastic energy is larger than the other energies within the material then the elastic stress can have an effect on the magnetization process (see section 2.3.2). For example, in polycrystalline magnetic films, there is not a preferred orientation due to the grain random arrangement, thus the magnetocrystalline anisotropy energy is small. The effect of elastic stress on magnetization is called the inverse magnetostrictive effect. The applied elastic stress will alter the domain structure and create a new anisotropy competing with the other anisotropies. The effect of elastic stress on magnetization can be understood based on the minimizing magnetoelastic energy (equation 2.8) in the magnetic system.

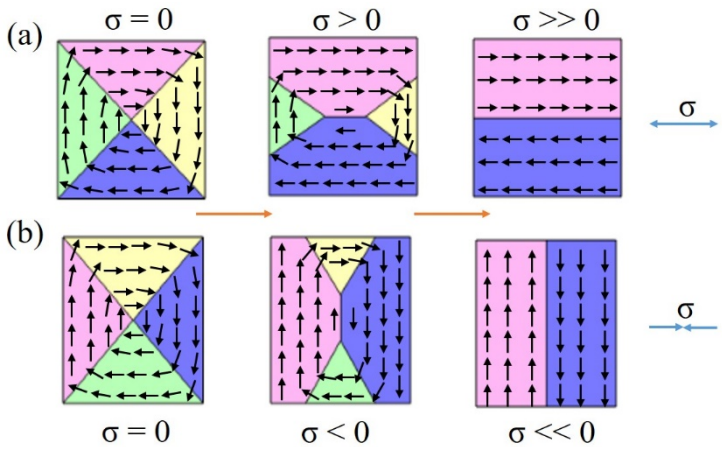

Fig. 2.4 Schematic of domain wall motion in a ferromagnetic material with positive magnetostriction under tensile stress (a) and compressive stress (b).

To minimize the magnetoelastic energy in a material, which has a positive λ, the external tensile stress (i.e. $\sigma > 0$, **Fig. 2.4** (a)) causes more magnetic moments to align along this tensile stress direction (i.e. $\theta = 0^o$). When an applied magnetic field is along this tensile stress direction, a lower field will be required to saturate the sample due to the relatively easy 180^o wall motion [6]. This means that a tensile stress produces a preferred magnetization direction. In contrast, when a compressive stress is applied (i.e. $\sigma < 0$, **Fig. 2.4** (b)) this causes more magnetic moments to align perpendicular to this compressive direction (i.e. $\theta = 90^o$). Thus, when the applied magnetic field is along this compressive direction, a higher magnetic field is required to rotate the magnetic moments 90^o into the field direction. In fact, the stress field plays the same role to move the domain wall in the magnetization process (see section 2.3.2) as that of the magnetic field.

2.4 Multiferroics

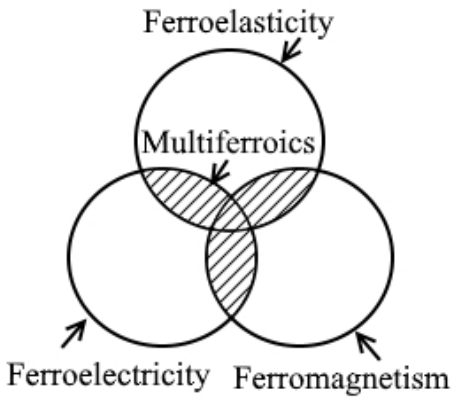

Fig. 2.5 Multiferroic materials with the coexistence of at least two ferroic properties.

Multiferroics [2,10,11] refers to a combination of several kinds of "ferroic" orders in a system such as ferromagnetism, ferroelectricity and ferroelasticity. Briefly, in these ferroics, there is a switchable domain structure. A field such as a magnetic field, an electric field or a stress field can switch between two system states in these ferroics. Multiferroic materials include at least two different ferroic orders, as shown **Fig. 2.5**. In particular, a combination of ferromagnetism and ferroelectricity is appealing due to the magnetoelectric effect (see section 2.4.2). However, in nature this rarely occurs in materials, which exhibit simultaneously magnetic polarization and electric polarization, i.e. single-phase multiferroic materials. Therefore, the multiferroic composites are designed artificially by combining ferroelectric and ferromagnetic phases together. More detailed information about multiferroic materials including their research progress and potential applications are found in Chapter 3. Here, only the multiferroics concept is introduced.

2.4.1 Ferroelectrics

In ferromagnetic materials, below a critical temperature, there is a spontaneous magnetization (M) or magnetic polarization, which is switched by an applied magnetic field (H). Similarly, in ferroelectric materials, there is a spontaneous electric polarization (P) below a fixed temperature, known as the Curie temperature, which is switched by an applied electric field (E). There are also other similarities [2]. The ferroelectric P-E hysteresis loop and the ferromagnetic M-H hysteresis loop are similar. The domains exist in both ferroelectric and ferromagnetic materials. Both transition from ferroelectric to paraelectric phase and from ferromagnetic to paramagnetic phase occur at a critical temperature (T_c). Also, ferromagnets have the piezomagnetic effect, whereas the ferroelectrics have the piezoelectric effect. However, the piezoelectric effect is much larger than the piezomagnetic effect. The former induced strain can be at the order of 10^3 ppm, while the later induced strain can be at the order of 10 ppm.

2.4.2 Magnetoelectric effect

In multiferroic materials, the coexistence of and coupling interaction between two "ferroic" phases can create additional functionalities. For example, the magnetoelectric effect is created by a coexistence of the ferroelectric phase and the ferromagnetic phase [12] An applied magnetic field can control the electric polarization through the so-called direct magnetoelectric effect (DME). Similarly, an applied electric field can control the magnetization through the so-called converse magnetoelectric effect (CME). They can be expressed as follows [12]:

$$\text{DME: } \Delta P = \alpha \Delta H \tag{2.9}$$

$$\text{CME: } \Delta M = \alpha \Delta E \tag{2.10}$$

where α is magnetoelectric coupling coefficient, P is the electric polarization, M is the magnetization or magnetic polarization, H is the magnetic field and E is the electric field. Specifically, in multiferroic composites, the magnetoelectric effect is a product property because neither ferroelectric phase nor ferromagnetic phase possesses the magnetoelectric effect, but the composites have the effect. The magnetoelectric effect is the product of the magnetostrictive effect in the ferromagnetic phase and the piezoelectric effect in the ferroelectric phase, i.e. [13]

$$\text{DME: } \frac{\text{magnetic}}{\text{mechanical}} \times \frac{\text{mechanical}}{\text{electric}} \tag{2.11}$$

$$\text{CME: } \frac{\text{electric}}{\text{mechanical}} \times \frac{\text{mechanical}}{\text{magnetic}} \tag{2.12}$$

Specifically, when a magnetic field is exerted to a composite, a shape change is produced due to magnetostriction effect. Then the mechanical strain is passed to ferroelectric phase, which causes the electric polarization change and vice versa.

Ideally, the electric polarization (P) and magnetization (M) show a hysteresis characterization with the manipulation of magnetic field (H) and electric field (E), respectively (**Fig. 2.6**), which is similar to the ferroelectric and ferromagnetic hysteresis loops. Therefore, the magnetoelectric effect shows many potential applications, such as magnetoelectric sensors [14-15] and magnetoelectric memory [16-19] devices.

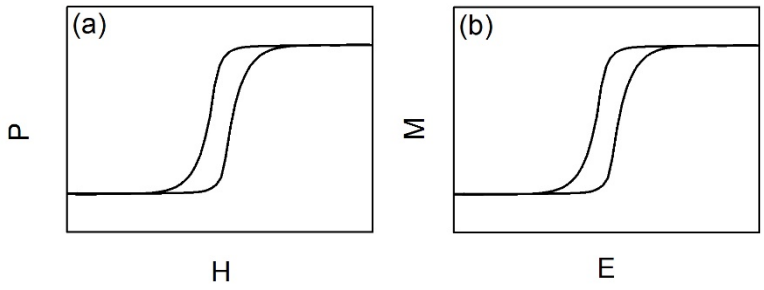

Fig. 2.6 Schematic illustration of ideal direct ME effect (a) and converse ME effect (b).

2.5 References

[1] B.D. Cullity, Introduction to Magnetic Materials, Addison-Wesley Publishing Company, 1972.

[2] N.A. Spaldin, Magnetic Materials Fundamentals and Applications, Cambridge University Press, 2011.

[3] C. Heck, Magnetic Materials and Their Applications, Hungary, 1974.

[4] A.H. Morrish, The Physical Principles of Magnetism, John Wiley & Sons, Inc, 1965.

[5] J.P. Jakubovics, Magnetism and Magnetic Materials, The Institute of Metals, 1987.

[6] B.D. Cullity, C.D. Graham, Introduction to Magnetic Materials, Hoboken : Wiley, 2009.

[7] R.S. Tebble, D.J. Craik, Magnetic Materials, J. W. Arrowsmith Ltd., 1969.

[8] A. Hubert, R. Schäfer, Magnetic Domains The Analysis of Magnetic Microstructures, Springer, 1998.

[9] D. Jiles, Introduction to Magnetism and Magnetic Materials, Chapman & Hall, 1991.

[10] M. Fiebig, J. Phys. D. Appl. Phys. 38 (2005) R123.

[11] W. Eerenstein, N.D. Mathur, J.F. Scott, Nature 442 (2006) 759.

[12] J. Ma, J.M. Hu, Z. Li, C.W. Nan, Adv. Mater. 23 (2011) 1062.

[13] C. Nan, Phys. Rev. B 50 (1994) 6082.

[14] J.Y. Zhai, Z.P. Xing, S.X. Dong, J.F. Li, D. Viehland, Appl. Phys. Lett. 88 (2006) 062510.

[15] C. Israel, N.D. Mathur, J.F. Scott, Nat. Mater. 7 (2008) 93.

[16] J.M. Hu, Z. Li, L.Q. Chen, C.W. Nan, Adv. Mater. 24 (2012) 2869.

[17] X. Chen, A. Hochstrat, P. Borisov, W. Kleemann, Appl. Phys. Lett. 89 (2006) 202508.

[18] M. Bibes, A. Barthélémy, Nat. Mater. 7 (2008) 425.

[19] J.M. Hu, Z. Li, L.Q. Chen, C.W. Nan, Nat. Commun. 2 (2011) 553.

Chapter 3

3 Literature Review

In Chapter 2, multiferroic materials and magnetoelectric coupling effect were briefly introduced. In this chapter, multiferroic materials including single-phase (see section 3.1) and composite materials (see section 3.2) will be described in detail. Both of them include bulk and nanostructure materials. In addition, the research progress on materials fabrication, mechanism studies and practical applications in the past few decades will be reviewed. Lastly, some challenges researchers need to meet in this field will be proposed and hence the aims of this project are presented.

3.1 Single-Phase Multiferroic Materials

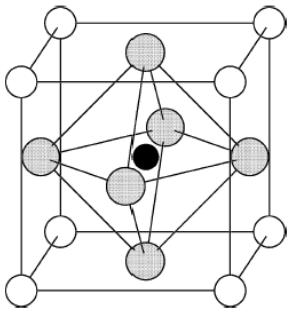

Fig. 3.1 Schematic illustration of the ABO_3 perovskite structure. A cations (white) occupy the corners of the unit cell. B cations (black) are at the centre of an octahedron of oxygen anions (grey) [1].

Single-phase multiferroic materials exist in nature or are synthesized in the laboratory and show an intrinsic magnetoelectric effect (see section 2.4.2). Single-phase multiferroic materials include ferroelectric polarization and ferromagnetic magnetization in the same phase [2]. Therefore, the magnetization can be controlled by an applied electric field and likewise the ferroelectric polarization can be controlled by an applied magnetic field. However, there are rarely any single-phase multiferroic materials. The first discovered multiferroic material was nickel iodine boracite ($Ni_3B_2O_{13}I$) [3], although some other multiferroic boracite compounds were synthesized afterwards. The multiferroic materials of (1-x)$PbFe_{0.66}W_{0.33}O_3$-x$PbMg_{0.5}W_{0.5}O_3$ (PFW-PMW) was first synthesized by the replacement of B site cations (**Fig. 3.1**) in ferroelectric perovskite oxides by magnetic cations (Fe^{3+}) [4]. Similarly, the B site replacement also produced Pb_2(Co, W)O_6 and Pb_2FeTaO_6 multiferroic materials. For these synthesized multiferroic materials, they all show very low Curie or Néel temperatures (<<273 K) [4]. Afterwards, significant progress was made on the study of various oxides, such as Bi-based compounds ($BiMnO_3$ [5–7] and $BiFeO_3$ [8,9]) and rare earth magnates ($TbMn_2O_5$ [10] and $YMnO_3$ [11]).

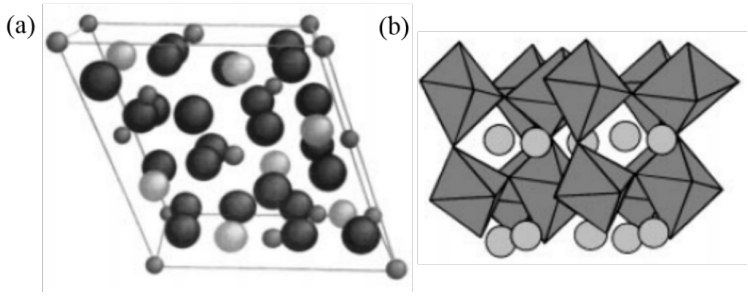

Fig. 3.2 Schematic illustration of the crystal structure of $BiMnO_3$. (a) Unit cell view: large, O^{2-}, middle, Bi^{3+} and small, Mn^{3+}. (b) A part of the crystal structure based on the perovskite unit. MnO_6 octahedra and bismuth cation are shown [5].

$BiMnO_3$ has a simple B site cation (**Fig. 3.2**) and is both ferromagnetic and ferroelectric due to the covalent bonding between Bi and O atoms [1]. $BiMnO_3$ is ferromagnetic with a transition temperature at about 105 K and ferroelectric with a Curie temperature at about 450 K [7]. $BiFeO_3$ (BFO) is antiferromagnetic with a high Néel temperature at 380 ^oC and ferroelectric with a high Curie temperature at 810 ^oC [4]. Palkar et al. [12] reported the Tb doped $BiFeO_3$ ($Bi_{0.9-x}Tb_xLa_{0.1}FeO_3$ compound) was ferromagnetic at room temperature. As shown in **Fig. 3.3**, the magnetoelectric coupling was observed by the changes of dielectric constant induced by the magnetic field.

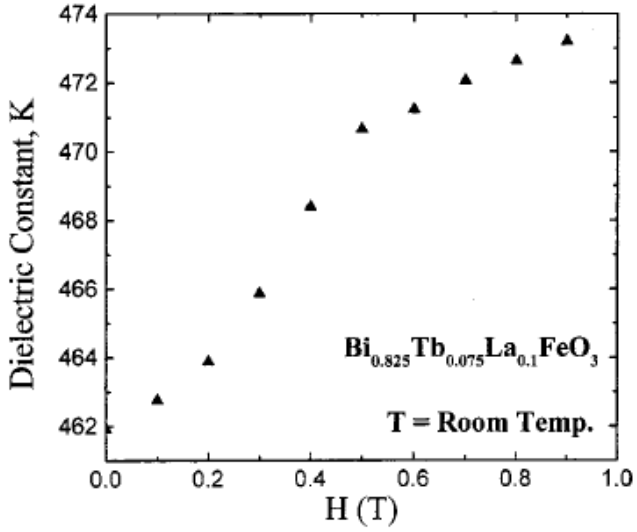

Fig. 3.3 Dielectric constant (K) versus the magnetic field for the $Bi_{0.9-x}Tb_xLa_{0.1}FeO_3$ compound at x = 0.075 [12].

Rare earth (RE) perovskite manganate compounds ($REMnO_3$, RE = Y, Ho, Er, Tm, Yb, Lu) are produced by the substitution of A site cation (**Fig. 3.1**). In **Fig. 3.4**, Lorenz et al. [13] demonstrated a decrease of up to 8% in the dielectric constant

tuned by an external magnetic field of 7 T for $HoMnO_3$ compound, which clearly provided the evidence of the strong magnetodielectric coupling in these compounds. Van Aken et al. [14] demonstrated the magnetoelectric coupling was weak in $LuMnO_3$ due to the predominant magnetic exchange coupling in the a b plane of the MnO_5 trigonal bipyramids and the electric dipole moments originating in the LuO_7 polyhedra along the hexagonal c axis.

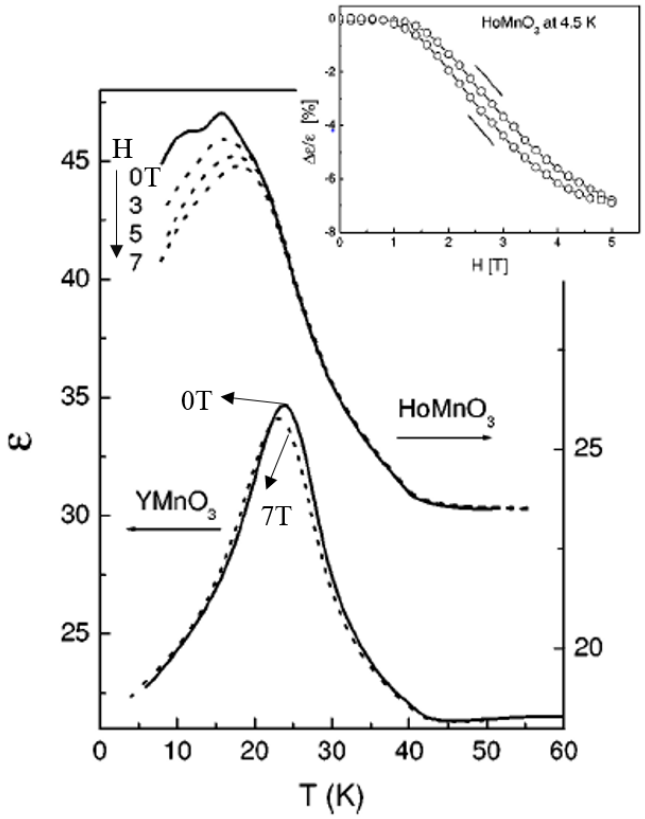

Fig. 3.4 Magnetodielectric effect in $YMnO_3$ and $HoMnO_3$. The inset shows the relative change of dielectric constant versus the magnetic field for $HoMnO_3$ at 4.5 K [13].

Recently, it was discovered that the family $REMn_2O_5$ [15,16] also showed multiferroic properties. In $REMn_2O_5$ compounds, the ferroelectric transition

temperature and antiferromagnetic transition temperature are around 25 K-39 K and 39 K-45 K, respectively [17]. Hur et al. [16] studied the detailed magnetic field dependence of the electric polarization and dielectric constant in (Tb, Dy, Ho)Mn_2O_5 and demonstrated an intimate coupling between magnetic and ferroelectric transitions. As shown in **Fig. 3.5**, the large dielectric constant change of 109 % was observed with applied magnetic field at 3 K in $DyMn_2O_5$).

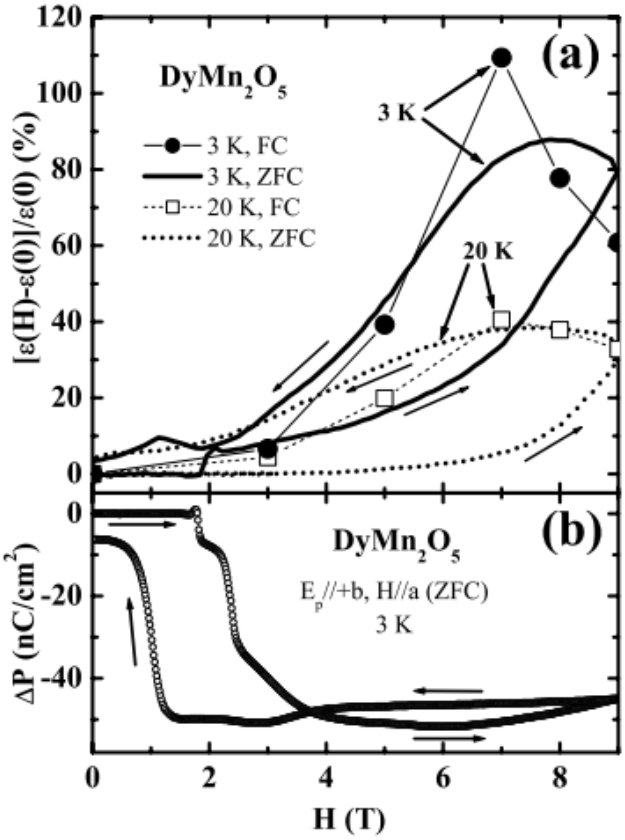

Fig. 3.5 (a) The variation of dielectric constant as a function of applied magnetic field for $DyMn_2O_5$ crystal at 3 K and 20 K. (b) The variation of the electric polarization by applied magnetic field at 3 K [16].

Bulk single-phase multiferroic materials have been studied widely as mentioned above. In addition, thin films of these materials ($BiMnO_3$ [18–20], $BiFeO_3$ [21–23] and $YMnO_3$ [24,25]) were also obtained for practical applications such as modern multifunctional devices. Epitaxial $BiMnO_3$ thin films were grown on (111) $SrTiO_3$ substrates by pulsed laser deposition (PLD) [18]. In **Fig. 3.6**, a clean interface between the film and substrate was observed in high-resolution transmission electron microscopy (HRTEM), which suggested that there was no impurity or amorphous phases. However, it was also seen the $BiMnO_3$ film surface was rough due to an island growth mode.

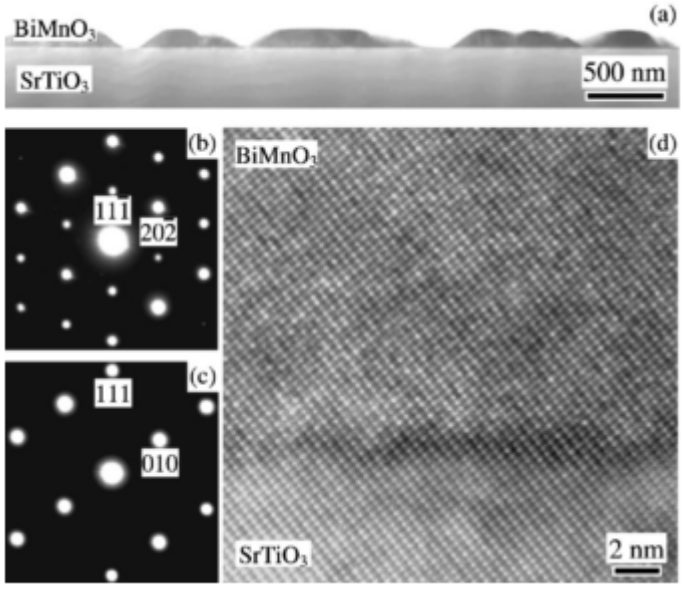

Fig. 3.6 (a) Cross-sectional TEM image of $BiMnO_3/SrTiO_3$ heterostructure. (b) and (c) selected-area electron diffraction (SAED) pattern of $BiMnO_3$ film and $SrTiO_3$ substrate. (d) HRTEM image of the interface between $BiMnO_3$ and $SrTiO_3$ [18].

Single-phase multiferroic materials have been widely investigated in both the forms of bulk and film. The intrinsic magnetoelectric effect in most of these materials only exists below room temperature. Strong magnetoelectric coupling above room temperature has not been found in any of these compounds, which limits the practical applications of single-phase multiferroic materials. Therefore, multiferroic composites with greater design flexibility and stronger magnetoelectric coupling at room temperature have drawn significant interest in recent years.

3.2 Multiferroic Composites

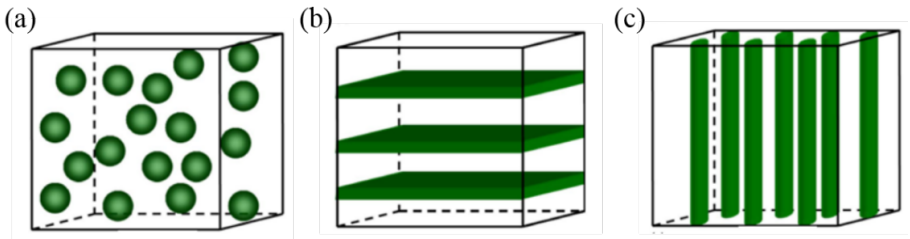

Fig. 3.7 Schematic illustration of three types of bulk composites: (a) particulate composites, (b) type laminate composites and (c) fibre or rod composites [26].

A multiferroic composite incorporates both a ferroelectric phase and antiferromagnetic or ferromagnetic phase. It produces giant magnetoelectric coupling response. For example, it is several orders of higher magnitude than that in single-phase multiferroic materials so far available [26] at room temperature. Therefore, they have huge potential applications as multifunctional devices. Since the concept of composite magnetoelectric effect was first proposed in 1972 [27], various multiferroic composites from bulk to thin film have been investigated, such as ceramic composites (piezoelectric ceramic and ferrites) [28–32], magnetic alloy-

based composites [33–36], polymer-based composites [37–40] and nanostructured composites [41–44]. Based on the concept of phase connectivity [45], there are particulate composites (**Fig. 3.7** (a)) with ferroelectric or magnetic oxide particles diffused in another phase matrix, laminate composites (**Fig. 3.7** (b)) consisting of ferroelectric and magnetic layers and fibre or rod composites (**Fig. 3.7** (c)) with ferroelectric or magnetic fibre or rod embedded another phase matrix to describe the structures of two phase composites [46].

The bulk multiferroic ceramic composites were first made via co-sintering ferroelectric oxides and ferrites, which created interfacial inter-diffusion and reaction problems, which deteriorated the magnetoelectric response. To solve these problems, chemical solution processing, spark-plasma sintering (SPS) [47] and microwave sintering [48] have been used. When an electric field (E-field) is applied to the ferroelectric matrix, a shape change of the ferroelectric phase is caused due to the E-field induced ferroelectric domain movement. Thus, a strain is exerted to the ferromagnetic phase diffused in the matrix, which alters the magnetic anisotropy or domain structure of the ferromagnetic phase due to the converse magnetostriction effect. For the laminate composite, interface electrodes were introduced into the composite to reduce magnetoelectric response loss due to poorly conductive ferrite layers. Similarly, to avoid interfacial inter-diffusion and reaction, film deposition techniques were utilized instead of high temperature co-sintering. For example, $Pb(ZrTi)O_3$ (PZT) films were directly grown on highly dense $CoFe_2O_4$ (CFO) ceramics by a simple solution spin coating and afterwards annealed at around 600 ^{o}C-700 ^{o}C [49].

Compared to the multiferroic ceramic-based bulk composites discussed above, magnetic alloy-based composites consist of a magnetostrictive alloy such as Terfenol-D ($Tb_{1-x}Dy_x Fe_2$) and Metglas (FeBSiC) layer and a ferroelectric layer such as PMN-PT (lead magnesium niobate-lead titanate). They show a stronger magnetoelectric coupling effect. Generally, the ferroelectric layer and magnetic alloy layer are bonded together by using an epoxy resin, followed by annealing at around 80-100 ^oC. The interfacial binders significantly affect the magnetoelectric effect of the composites [50], including possible adhesive fatigue and aging effect. Therefore, to eliminate these influences, the magnetic alloy layer is deposited onto the ferroelectric layer by sputtering [51,52] and electro-deposition [53]. 4 μm thick TbTe/FeCo multilayers were sputtered onto a PMN-PT piezoelectric single crystal. A magnetoelectric coupling value of 13 mV/(Oe cm) was achieved when a dc bias magnetic field of 2 mT was exerted [52]. Much larger magnetoelectric coupling value of 33 V/(Oe cm) at the electromechanical resonance frequency was also demonstrated in 0.4 mm Ni/0.25 mm PZT/0.4 mm Ni heterostructure by the electro-deposition method because the electromechanical produced a tight bonding between Ni and PZT [53].

In comparison with the multiferroic ceramic-based and magnetic alloy-based bulk composites, polymer-based composites [54,55] are easier to prepare by a traditional low-temperature processing into various forms and also show better mechanical properties. For example, a simple magnetoelectric composite was made by embedding a single PZT rod into a Terfenol-D/epoxy matrix. This composite showed larger magnetoelectric coupling than multiferroic composites with PZT rod arrays [55].

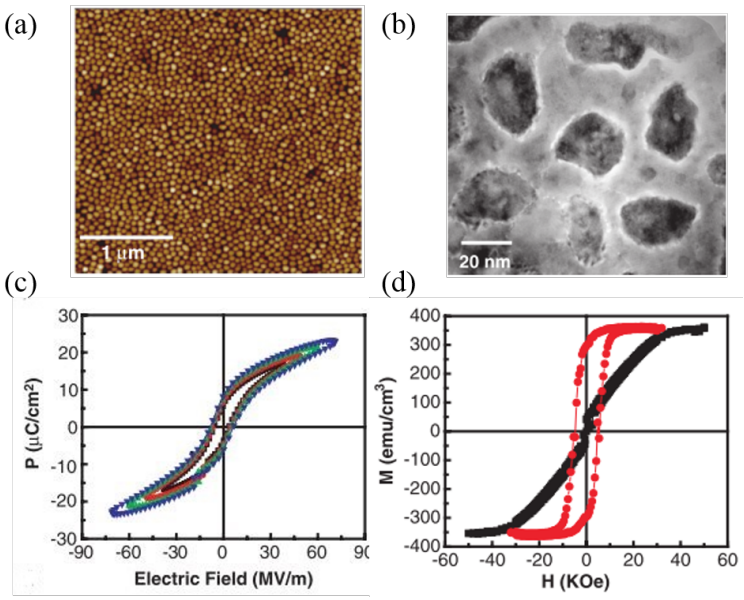

Fig. 3.8 Atomic Force Microscopy (AFM) topography image (a) and TEM planar view image (b) of the film. Polarization-electric field hysteresis loop (c) and out-of-plane (red) and in-plane (black) magnetic hysteresis loops (d) [44].

Nanostructured composite thin films have been developed as new routes to investigate the physical mechanism of magnetoelectric coupling effect in the nanoscale. Compared to the bulk multiferroic composites mentioned above, the nanostructured thin films combine different phases at the atomic level. Here, the nanostructured composite thin films refer to systems where both the ferroelectric and magnetic phases are nanoscale. For example, self-assembled $CoFe_2O_4$ (CFO) nanopillars [44] was embedded into the $BaTiO_3$ (BTO) thin film matrix deposited by pulsed laser deposition. As shown in **Fig. 3.8** (a) and (b). In **Fig. 3.8** (c) and (d), ferroelectric and magnetic measurements showed a saturation polarization of ~ 23 $\mu C/cm^2$ and a saturation magnetization of ~ 350 emu/cm^3, respectively. The piezoelectric measurement revealed the piezoelectric constant d_{33} of the BTO matrix

was ~ 50 pm/V, compared with the single crystal BTO ~ 130 pm/V, which was due to the clamping effects from both STO substrate and CFO nanopillar arrays [44].

3.3 Electric-field Control of Magnetism in Magnetic Thin Films

Recently, the use of an electric field to control the magnetic properties in magnetoelectric materials (converse magnetoelectric effect) rather than a magnetic field generated by a current [56] or the current itself [57] has drawn intensive interest due to their important potential applications such as magnetoelectric random access memory (MERAM) devices [58–61] (see section 3.4.1) and magnetoelectric sensor [62,63]. The magnetoelectric coupling in magnetoelectric composite thin films can be realized by three different mechanisms, i.e. charge-mediated magnetoelectric effect [64–69], exchange bias-mediated magnetoelectric effect [70–73] and strain-mediated magnetoelectric effect.

3.3.1 Charge-mediated Magnetoelectric Coupling

In magnetoelectric layered heterostructure containing ultrathin ferromagnetic films (< 5 nm), an electric field causes the accumulation of spin-polarized electrons at the interface and thus creates an interface magnetization change [46]. The influence of electric field on magnetization is only at the interface and therefore the ferromagnetic films have to be ultrathin. In an electrolytic cell containing 2 nm thick FePt film, a maximum coercivity change of -4.5 % was demonstrated with a voltage change of -600 mV, which was attributed to a change in the number of unpaired *d* electrons due to the electric field [66]. However, for 4 nm thick FePt film, a smaller change of -1 % was observed. In addition, the coercivity change in response to the voltage was essentially reversible, suggesting that the observed effect was intrinsic and not caused by film contamination or electrochemical reaction [66]. To avoid

involving liquid electrolyte, an all-solid-state bcc 0.48 nm (001) Fe/ 10 nm (001) MgO junction was fabricated, where a large change of ~ 40% in the magnetic anisotropy was observed due to the change in the relative occupation of 3 *d* orbitals of Fe atoms adjacent to the MgO barrier [65]. In Fe/$BaTiO_3$ (BTO) multiferroic heterostructure [68], the physical mechanism of the magnetoelectric coupling was explained that a change in ferroelectric-ferromagnetic interfacial bonding resulted in the change in the interfacial magnetization when the electric field was applied. Interfacial atomic displacements due to ferroelectric instability changed the overlap between atomic orbitals and thus changed the interfacial magnetization. As shown in **Fig. 3.9** (a) and (b), the overlap between Ti and Fe electronic clouds were distinct for two opposite electric polarizations in BTO. The *d* orbital hybridization between Ti and Fe was stronger for the former.

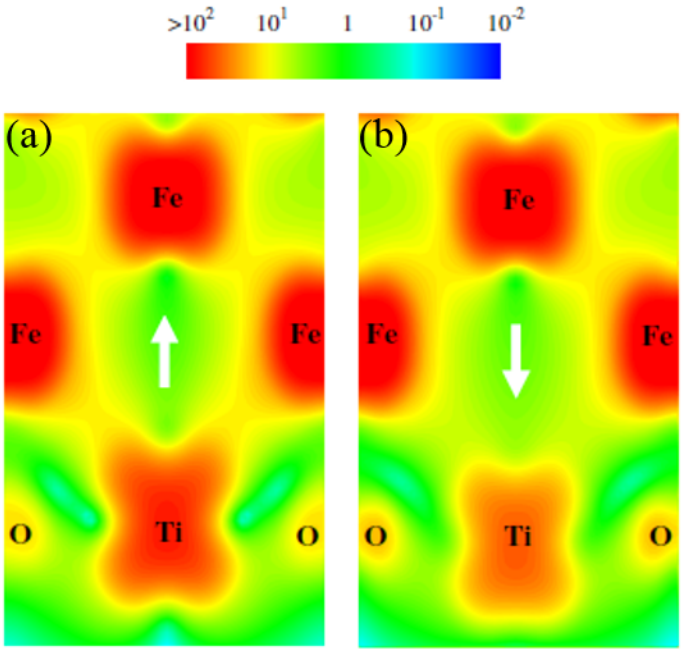

Fig. 3.9 Minority-spin charge density at the Fe/BTO interface for two opposite electric polarizations in BTO. The arrows indicate the directions of electric polarizations [68].

More recently, Molegraaf et al. [64] demonstrated a large charge-driven magnetoelectric coupling in 4 nm $La_{0.8}Sr_{0.2}MnO_3$/250 nm $PbZr_{0.2}Ti_{0.8}O_3$ (PZT) composite structure where the magnetism was directly controlled via the charge-carrier concentration modulation. In **Fig. 3.10**, the magnetic behaviour of the composite structure showed a hysteresis response to an applied electric field. A magnetoelectric coupling coefficient α of 0.8×10^{-3} Oe cm V^{-1} was obtained at 100 K. However, the much larger coefficient of 25×10^{-3} Oe cm V^{-1} [74] was reported in the same system but via strain-mediated mechanism rather than charge-mediated mechanism. In addition, electric field controlled the spin polarization of Fe layer at the Fe/BTO interface was also observed in Fe/BTO/$La_{0.67}Sr_{0.33}MnO_3$ (LSMO) multiferroic tunnel junction due to electrically switching ferroelectric polarization state in BTO [69]. A repeatable manipulation of tunnel magnetoresistance (TMR) by the ferroelectric polarization was obtained, which provided a low-power approach for spin-based information control [69].

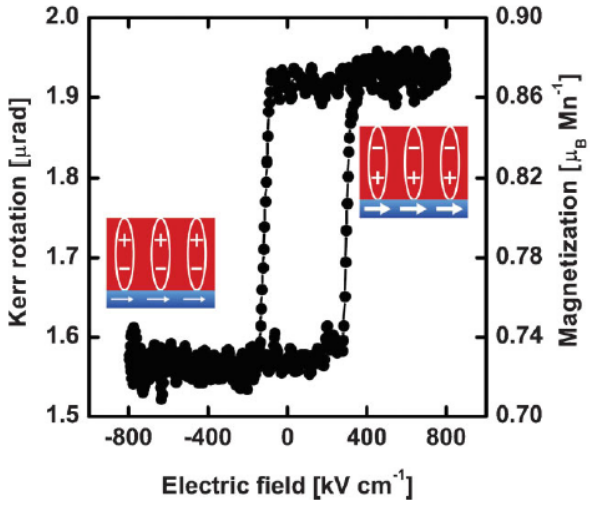

Fig. 3.10 The magnetic response of the PZT/LSMO system as a function of the applied electric field at 100 K. The insets show electric and magnetic states of PZT and LSMO

layers, respectively. The size of arrows indicates qualitatively the amplitude of magnetization. The two y-axes refer to MOKE data and the corresponding data from SQUID magnetometry, more details in [64].

3.3.2 Exchange Bias-mediated Magnetoelectric Coupling

The exchange bias results from the exchange coupling between the antiferromagnetic layer and the ferromagnetic layer, which has also been used for the electric field controlled magnetization in ferromagnetic films [46]. A characteristic feature is a shift in the magnetic hysteresis loop when the exchange coupling occurs. The detailed mechanism of the exchange bias can be found in [75]. An approach to achieve exchange-bias-mediated magnetoelectric coupling is to combine ferroelectric/antiferromagnetic multiferroics ($BiFeO_3$, BFO) with ferromagnetic thin films. Chu et al. [71] demonstrated an electric field controlled local magnetism in $Co_{0.9}Fe_{0.1}$/BFO heterostructure based on the presence of two coupling mechanisms, which included the first magnetoelectric coupling between antiferromagnetism and ferroelectricity in BFO and the second exchange interactions between the ferromagnetism and antiferromagnetism at the interface between $Co_{0.9}Fe_{0.1}$ and BFO.

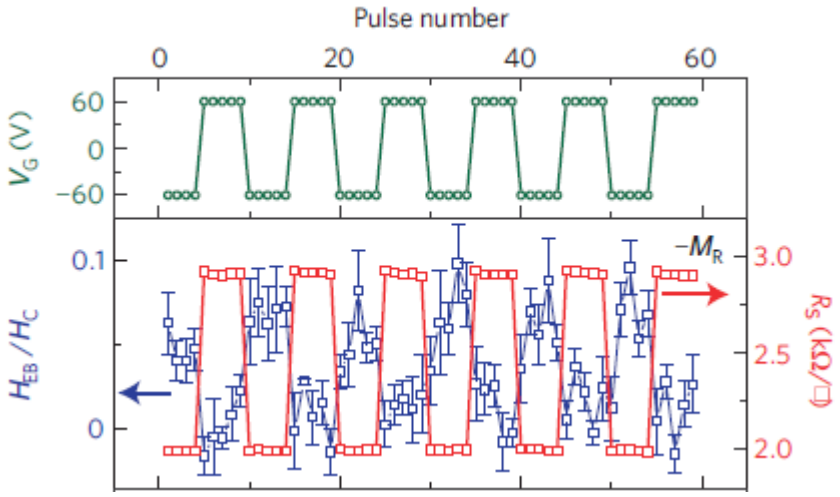

Fig. 3.11 Measurements of normalized exchange bias to the coercivity H_c and peak resistance for the gate-pulse sequence [72].

More recently, as shown in **Fig. 3.11**,it was observed two distinct exchange-bias states were reversibly switched by switching the ferroelectric polarization of BFO in BFO/LSMO heterostructures [72]. Two ferroelectric polarization states were alternated after every five voltage pulses. The exchange bias (H_{EB}) was thus changed between a high H_{EB} and a low H_{EB}, corresponding a low or high resistance R_S. The maximum H_{EB} change was about 0.15 H_c, i.e. about 125 Oe. For **Fig. 3.11**, the remanent magnetization was set into a negative state, i.e. $-M_r$. When the remanent magnetization was set into a positive state, i.e. M_r, the H_{EB} and R_S were also switched by the voltage pulses between high and low values, more information can be found in the reference [72].

To understand the possible mechanism for electric field controlled exchange bias, the exchange bias origin was studied. The mechanism for exchange bias in such structures was thought to be the formation of ferromagnetic moments at the BFO interface due to interfacial orbital reconstruction. The consequent exchange bias

modulation by the electric field was due to the carrier movement by the electric field, which modified the magnetic properties of LSMO.

3.3.3 Strain-mediated Magnetoelectric Coupling

Compared to the magnetoelectric coupling mechanisms discussed above, the strain-mediated mechanism is the main and effective route for the magnetoelectric coupling. Briefly, an external electric field induces a change in the shape of ferroelectric phase due to the converse piezoelectric effect and then the piezoelectric strain is passed on to magnetic phase, which alters the magnetization in magnetic phase due to the magnetostriction effect. Substantial experimental work [76–90] on strain-mediated ME effect has been published in recent years. Most of them are focused on ferromagnetic film/ ferroelectric substrate heterostructures (**Fig. 3.12**), such as such as Fe-Ga/(110) PMN-PT [77], $Ni_{80}Co_{20}$/(110) PZN-PT (lead zinc niobate-lead titanate) [86], FeGaB/(110) PZN-PT [85], Fe_3O_4/PZN-PT [87], $NiFe_2O_4$/(001) PMN-PT [82], CFO/PMN-PT [88], Ni/(110) PMN-PT [80], CoPd/PZT [90] and Ni/BTO [89]. As shown in these heterostructures, the magnetic films include either metallic films such as FeGa and CoFe or oxide-based such as Fe_3O_4 and LSMO, while the ferroelectric substrates include single crystals such as BTO, PZT, PMN-PT and PZN-PT or ceramics.

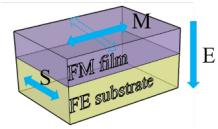

Fig. 3.12 A schematic of ferromagnetic film/ ferroelectric substrate heterostructure. The external electric field (E) is applied on ferroelectric substrate and thus a strain (S) is created

due to converse piezoelectric effect. The strain passes on to the ferromagnetic film, which alters the magnetisation (M) due to magnetostriction effect.

The electric field induced magnetization change based on the strain-mediated magnetoelectric coupling mechanism was first observed in the LSMO/BTO heterostructure [91]. 40 nm epitaxial LSMO films were grown on 0.5 mm (001) BTO substrates by PLD. A giant, sharp and persistent magnetization change with magnetoelectric coupling coefficient α up to $2.3 \times 10^{-7} sm^{-1}$ was observed due to the electric field induced ferroelectric domain structure change and the resulting deformation transmitted to the LSMO film. Similarly, 20-50 nm thick LSMO films were also grown on (001) PMN-PT substrates. An electric field controlled magnetization was observed in the LSMO/PMN-PT heterostructure [74], with a maximum magnetoelectric coupling coefficient α of 6×10^{-8} sm^{-1}. Interestingly, the electric field induced magnetization change curve showed a "butterfly" shape (**Fig. 3.13** (b)) which is same as the piezoelectric strain curve (**Fig. 3.13** (a)). This suggests the piezoelectric strain played an important role in the electric field controlled magnetization process.

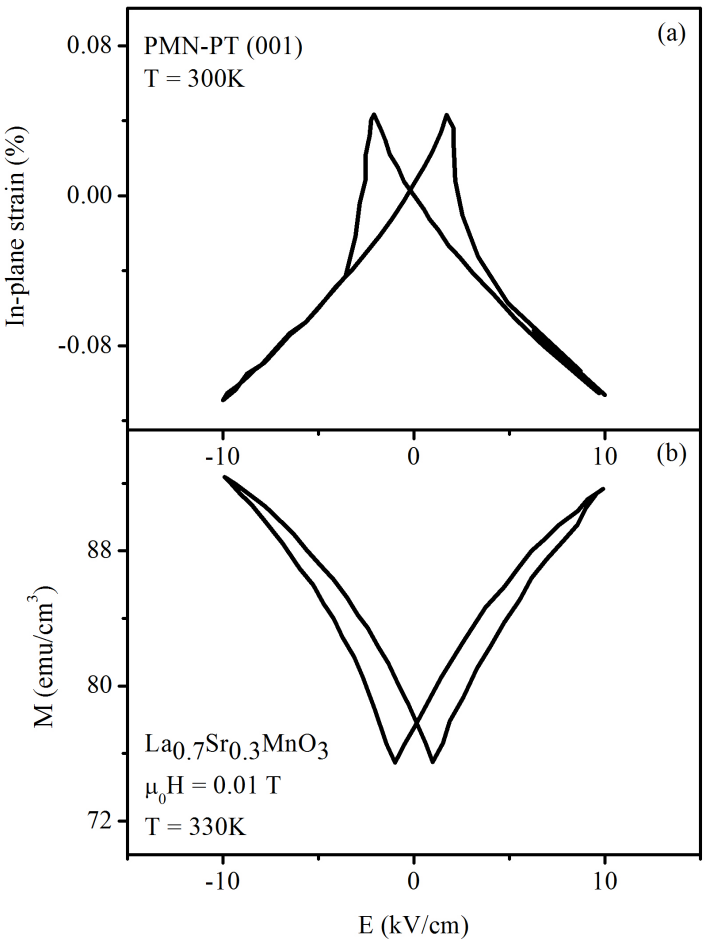

Fig. 3.13 (a) The in-plane piezoelectric strain curve along [100] of (001) PMN-PT. (b) The electric field induced magnetization change along [100] curve of the LSMO film [74].

As mentioned above, the ferromagnetic metallic films were also deposited on the ferromagnetic oxide substrates. 10 nm thick Fe thin film grown on a BTO single crystal showed a large magnetization change in response to both applied electric fields and temperature change [92]. The reason was due to ferroelectric switching and structural transitions of BTO induced by the applied field and temperature, respectively. Up to a 120 % coercive field change was induced by the temperature change, whereas a 20 % coercive field change was created by the applied field. 25 μm thick amorphous Metglas ribbon (Metglas Inc. 2605C0, $Fe_{67}Co_{18}B_{14}Si_1$) fixed to

the PMN-PT substrate showed the electric tunability of magnetic parameters such as 54 % decrease in the remanence and 170 % increase in the coercivity by the applied electric field [93].

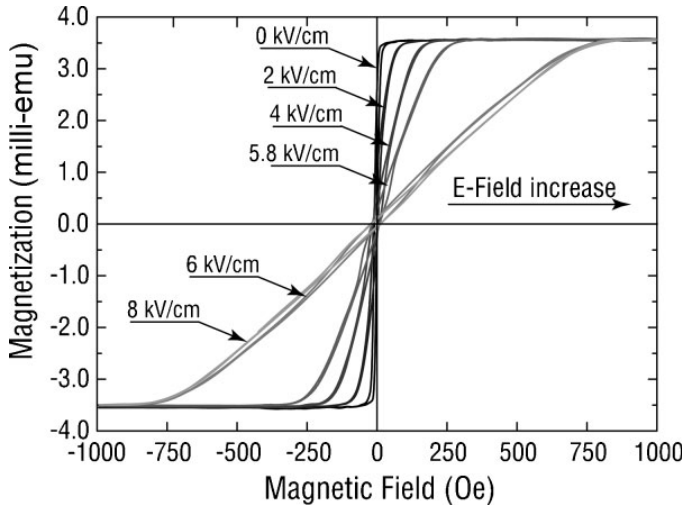

Fig. 3.14 The electric dependence of magnetic hysteresis loops for the 100 nm FeGaB thin film grown on the PZN-PT substrate [84].

Similarly to the electric field modified magnetization and coercive field, the magnetic anisotropy field could also be altered by the applied external electric field. As shown in **Fig. 3.14**, the magnetic hysteresis loops are greatly tuned by the applied electric field. A highly magnetostrictive 100 nm FeGaB film was grown on the PZN-PT substrate using a magnetron sputtering method [84]. A large electric field induced effective magnetic anisotropy field of about 686 Oe (54.6 kA/m) was observed in the heterostructure when the electric field of 8 kV/cm was applied. Here, the effective magnetic anisotropy field refers to the difference between the anisotropy field with and without the electric field.

To understand the electric controlled magnetic property changes, microscopic measurements have also been done. For example, Chung et al. [94] reported a reversible magnetic domain-wall motion in 100 nm Ni/ 1.28 μm PZT bilayer thin films. The electric field induced magnetic stripe-domain pattern changed in the Ni layer were observed using Magnetic Force Microscopy (MFM). Moreover, after removing the electric field, the domain patterns returned to their initial configuration.

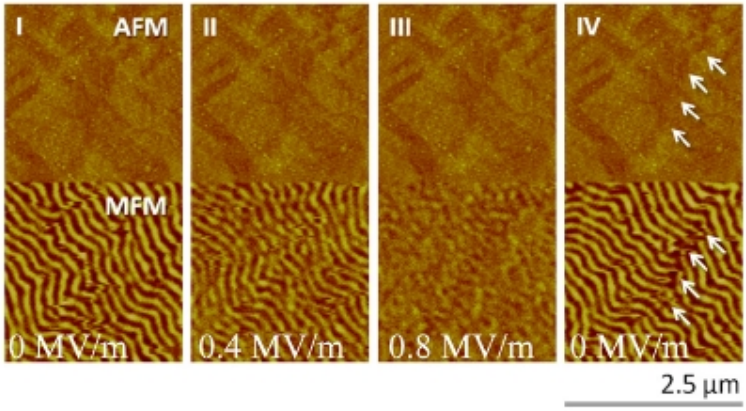

Fig. 3.15 AFM and MFM images of 60 nm Ni thin film grown on (001) PMN-PT substrate under different electric fields: 0 MV/m, 0.4 MV/m and 0.8 MV/m [95].

More recently, Hsu et al. [95] reported magnetoelectric manipulation of the domain structure in 60 nm Ni thin film grown on (001) PMN-PT substrate, as shown in **Fig. 3.15**. The stripe domain pattern was eliminated by the electric field induced isotropic in-plane compressive strain of around 1000 ppm. After removing the electric field, the domain patterns returned to their initial configuration but some domain walls were pinned due to the surface roughness of the PMN-PT substrate. Atomic Force Microscope (AFM) images showed a height difference between the adjacent

ferroelectric domains of around 2 nm. These microscopic measurements suggested that the electric field controlled magnetic properties such as the remanence, coercive field and anisotropy field, were associated with the strain induced domain wall motion.

3.3.4 The remaining Challenges

As reviewed above, multiferroic materials have been drawing more attention from many researchers due to their appealing applications potential (see section 3.4) in the past few decades. A lot of research has been done, including improving the magnetoelectric coupling and the microscopic mechanism understanding. However, there are still many problems and challenges people need to investigate and understand. Especially, the multiferroic thin film composites which are a popular research topic but still in the infant stage [46]. For example, in strain-mediated magnetoelectric heterostructures:

- ✓ Firstly, a well-defined interface between ferroelectric and ferromagnetic phases is important to the magnetoelectric coupling but hard to obtain. The reason is due to the large lattice misfit between the two phases and a rough surface of ferroelectric substrates arising from ferroelectric domains and polishing scratches;
- ✓ Secondly, the magnetoelectric coupling strength still needs to be improved by optimizing and designing multiferroic heterostructures such as optimizing the film thickness to improve the strain relaxation and introducing a buffer layer to improve interfacial coupling.
- ✓ Finally, the magnetoelectric coupling mechanism needs to be explored further. In a system, there may be several competing mechanism and they may combine and contribute to the coupling at the same time. For example, the combination of the

strain-mediated and exchange-bias mediated magnetoelectric coupling in the $Co_{0.9}Fe_{0.1}$/BFO heterostructure [71].

3.4 Applications

Multiferroic materials have many important potential applications such as magnetoelectric random access memory (MERAM) devices [58–61] (see section 3.4.1) and magnetoelectric sensor [62,63] (see section 3.4.2).

3.4.1 Magnetoelectric Memory

In multiferroic materials, an electric field controlling the magnetic properties can be applied in magnetoelectric random access memory (MERAM) devices [58–61]. The possible MERAM has important advantages over magnetic random access memory (MRAM) such as a fast writing speed and reduced energy consumption. In commercial magnetic storage devices, hard magnetic materials (i.e. having a high coercive field) are required to be used so that the data storage is stable. But, this means that a high writing magnetic field produced by a high current is needed with a high energy consumption and a low writing speed. In contrast, in MERAM, the electric field is applied to the ferroelectric layer, the magnetization state in ferromagnetic layer can be changed when the magnetoelectric coupling is strong enough. In this process, no current is involved and thus no heat is produced. A MERAM element [60] has been proposed and also has been demonstrated experimentally.

3.4.2 Magnetoelectric Sensor

The magnetoelectric coupling effect in multiferroic materials also can be applied in magnetoelectric sensors. It has been experimentally demonstrated [63] that a

commercial multilayer capacitor (MLC) can be used as a magnetic field sensor due to the magnetoelectric coupling effect. In fact, the MLC includes a multiferroic laminate ferromagnetic Ni/ferroelectric $BaTiO_3$ (BTO) heterostructures, where Ni is the electrodes. When the magnetic field is applied on the MLC, the magnetostrictive Ni layer creates a strain due to the magnetostriction effect and then the strain is transferred to the ferroelectric BTO layer. In the BTO layer, an electric voltage is produced due to the piezoelectric effect and then it can be detected. In the MLC, a maximum sensitivity is that the electric voltage of 7 mV generated by the magnetic field of 0.1 T. Although it is less sensitive than a superconducting quantum interference device (SQUID), the MLC is operated in room temperature and can be produced cheaply only 1 cent [63].

3.5 References

[1] N.A. Hill, K.M. Rabe, Phys. Rev. B 59 (1998) 8759–8769.

[2] H. Schmid, Ferroelectrics 162 (1994) 317.

[3] E. Ascher, H. Rieder, H. Schmid, H. Stössel, J. Appl. Phys. 37 (1966) 1404–1405.

[4] W. Prellier, M.P. Singh, P. Murugavel, J. Phys. Condens. Matter 17 (2005) R803–R832.

[5] T. Atou, H. Chiba, K. Ohoyama, Y. Yamaguchi, Y. Syono, J. Solid State Chem. 145 (1999) 639–642.

[6] A. Moreira Dos Santos, A. Cheetham, T. Atou, Y. Syono, Y. Yamaguchi, K. Ohoyama, H. Chiba, C. Rao, Phys. Rev. B 66 (2002) 064425.

[7] A. Moreira Dos Santos, S. Parashar, A.R. Raju, Y.S. Zhao, A.K. Cheetham,

C.N.R. Rao, Solid State Commun. 122 (2002) 49–52.

[8] M.M. Kumar, V.R. Palkar, K. Srinivas, S. V Suryanarayana, Appl. Phys. Lett. 76 (2000) 2764–2766.

[9] Y.P. Wang, L. Zhou, M.F. Zhang, X.Y. Chen, J.M. Liu, Z.G. Liu, Appl. Phys. Lett. 84 (2004) 1731–1733.

[10] N. Hur, S. Park, P. a Sharma, J.S. Ahn, S. Guha, S.-W. Cheong, Nature 429 (2004) 392–395.

[11] A. Filippetti, N. Hill, Phys. Rev. B 65 (2002) 195120.

[12] V.R. Palkar, D.C. Kundaliya, S.K. Malik, S. Bhattacharya, Phys. Rev. B 69 (2004) 212102.

[13] B. Lorenz, Y.Q. Wang, Y.Y. Sun, C.W. Chu, Phys. Rev. B 70 (2004) 212412.

[14] B.B. Van Aken, T.T.M. Palstra, Phys. Rev. B 69 (2004) 134113.

[15] D. Higashiyama, S. Miyasaka, N. Kida, T. Arima, Y. Tokura, Phys. Rev. B 70 (2004) 174405.

[16] N. Hur, S. Park, P.A. Sharma, S. Guha, S.W. Cheong, Phys. Rev. Lett. 93 (2004) 107207.

[17] I. Kagomiya, K. Kohn, T. Uchiyama, Ferroelectrics 280 (2002) 297–309.

[18] A. Sharan, J. Lettieri, Y. Jia, W. Tian, X. Pan, D.G. Schlom, V. Gopalan, Phys. Rev. B 69 (2004) 214109.

[19] J.Y. Son, B.Q. Kim, C.H. Kim, J.H. Cho, Appl. Phys. Lett. 84 (2004) 4971–4973.

[20] A. Sharan, I. An, C. Chen, R.W. Collins, J. Lettieri, Y. Jia, D.G. Schlom, V. Gopalan, Appl. Phys. Lett. 83 (2003) 5169–5171.

[21] J. Li, J. Wang, M. Wuttig, R. Ramesh, N. Wang, B. Ruette, a. P. Pyatakov, a. K. Zvezdin, D. Viehland, Appl. Phys. Lett. 84 (2004) 5261–5263.

[22] J. Wang, J.B. Neaton, H. Zheng, V. Nagarajan, S.B. Ogale, B. Liu, D. Viehland, V. Vaithyanathan, D.G. Schlom, U. V Waghmare, N. a Spaldin, K.M. Rabe, M. Wuttig, R. Ramesh, Science 299 (2003) 1719–1722.

[23] V.R. Palkar, J. John, R. Pinto, Appl. Phys. Lett. 80 (2002) 1628–1630.

[24] N. Fujimura, T. Ishida, T. Yoshimura, T. Ito, Appl. Phys. Lett. 69 (1996) 1011–1013.

[25] D. Ito, N. Fujimura, T. Yoshimura, T. Ito, J. Appl. Phys. 93 (2003) 5563–5567.

[26] C.W. Nan, M.I. Bichurin, S. Dong, D. Viehland, G. Srinivasan, J. Appl. Phys. 103 (2008) 031101.

[27] J. Vansucht, Philips Res. Reports 27 (1972) 28.

[28] S.L. Kadam, K.K. Patankar, V.L. Mathe, M.B. Kothale, R.B. Kale, B.K. Chougule, Mater. Chem. Phys. 78 (2003) 684–690.

[29] R.S. Devan, S.A. Lokare, D.R. Patil, S.S. Chougule, Y.D. Kolekar, B.K. Chougule, J. Phys. Chem. Solids 67 (2006) 1524–1530.

[30] Y.J. Li, X.M. Chen, Y.Q. Lin, Y.H. Tang, J. Eur. Ceram. Soc. 26 (2006) 2839–2844.

[31] J.P. Zhou, H.C. He, Z. Shi, G. Liu, C.W. Nan, J. Appl. Phys. 100 (2006)

094106.

[32] R.S. Devan, S.B. Deshpande, B.K. Chougule, J. Phys. D. Appl. Phys. 40 (2007) 1864–1868.

[33] S. Dong, J.F. Li, D. Viehland, Appl. Phys. Lett. 85 (2004) 2307–2309.

[34] S. Dong, J.F. Li, D. Viehland, J. Cheng, L.E. Cross, Appl. Phys. Lett. 85 (2004) 3534–3536.

[35] P. Li, Y. Wen, L. Bian, Appl. Phys. Lett. 90 (2014) 022503.

[36] X.M. Yin, N. Zhang, J.C. Bao, Phys. Lett. A 361 (2007) 434–436.

[37] N. Cai, C.W. Nan, J. Zhai, Y. Lin, Appl. Phys. Lett. 84 (2004) 3516–3518.

[38] J.G. Wan, J.M. Liu, H.L.W. Chand, C.L. Choy, G.H. Wang, C.W. Nan, J. Appl. Phys. 93 (2003) 9916–9919.

[39] C.W. Nan, N. Cai, Z. Shi, J. Zhai, G. Liu, Y. Lin, Phys. Rev. B 71 (2005) 014102.

[40] Z. Shi, J. Ma, Y. Lin, C.W. Nan, J. Appl. Phys. 101 (2007) 043902.

[41] J. Zhou, H. He, Z. Shi, C.-W. Nan, Appl. Phys. Lett. 88 (2006) 013111.

[42] P. Murugavel, P. Padhan, W. Prellier, Appl. Phys. Lett. 85 (2004) 4992–4994.

[43] F. Zavaliche, H. Zheng, L. Mohaddes-Ardabili, S.Y. Yang, Q. Zhan, P. Shafer, E. Reilly, R. Chopdekar, Y. Jia, P. Wright, D.G. Schlom, Y. Suzuki, R. Ramesh, Nano Lett. 5 (2005) 1793–1796.

[44] H. Zheng, J. Wang, S.E. Lofland, Z. Ma, L. Mohaddes-Ardabili, T. Zhao, L. Salamanca-Riba, D.G. Schlom, M. Wuttig, A. Roytburd, R. R., Science 303

(2004) 661–663.

[45] R.E. Newnham, D.P. Skinner, L.E. Cross, Mater. Res. Bull. 13 (1978) 525–536.

[46] J. Ma, J.M. Hu, Z. Li, C.W. Nan, Adv. Mater. 23 (2011) 1062–1087.

[47] Q.H. Jiang, J. Ma, Y.H. Lin, C.-W. Nan, Z. Shi, Z.J. Shen, Appl. Phys. Lett. 91 (2007) 022914.

[48] S. Agrawal, J. Cheng, R. Guo, A.S. Bhalla, R. a. Islam, S. Priya, Mater. Lett. 63 (2009) 2198–2200.

[49] J. Wang, L. Wang, G. Liu, Z. Shen, Y. Lin, C.W. Nan, J. Am. Ceram. Soc. 92 (2009) 2654–2660.

[50] C.W. Nan, G. Liu, Y. Lin, Appl. Phys. Lett. 83 (2003) 4366–4368.

[51] D. Seguin, M. Sunder, L. Krishna, A. Tatarenko, P.D. Moran, J. Cryst. Growth 311 (2009) 3235–3238.

[52] S. Stein, M. Wuttig, D. Viehland, E. Quandt, J. Appl. Phys. 97 (2005) 10Q301.

[53] D.A. Pan, Y. Bai, W.Y. Chu, L.J. Qiao, J. Phys. Condens. Matter 20 (2008) 025203.

[54] J. Ma, Z. Shi, C.W. Nan, J. Phys. D. Appl. Phys. 41 (2008) 155001.

[55] J. Ma, Z. Shi, C.W. Nan, Adv. Mater. 19 (2007) 2571–2573.

[56] G.A. Prinz, Science 282 (1998) 1660–1663.

[57] E.B. Myers, D.C. Ralph, J.A. Katine, R.N. Louie, R.A. Buhrman, Science 285 (1999) 867–870.

[58] J.M. Hu, Z. Li, L.Q. Chen, C.W. Nan, Adv. Mater. 24 (2012) 2869–2873.

[59] X. Chen, A. Hochstrat, P. Borisov, W. Kleemann, Appl. Phys. Lett. 89 (2006) 202508.

[60] M. Bibes, A. Barthélémy, Nat. Mater. 7 (2008) 425–426.

[61] J.M. Hu, Z. Li, L.Q. Chen, C.W. Nan, Nat. Commun. 2 (2011) 553.

[62] J.Y. Zhai, Z.P. Xing, S.X. Dong, J.F. Li, D. Viehland, Appl. Phys. Lett. 88 (2006) 062510.

[63] C. Israel, N.D. Mathur, J.F. Scott, Nat. Mater. 7 (2008) 93–94.

[64] H.J.A. Molegraaf, J. Hoffman, C.A.F. Vaz, S. Gariglio, D. Van Der Morel, C.H. Ahn, J.M. Triscone, Adv. Mater. 21 (2009) 3470–3474.

[65] T. Maruyama, Y. Shiota, T. Nozaki, K. Ohta, N. Toda, M. Mizuguchi, A.A. Tulapurkar, T. Shinjo, M. Shiraishi, S. Mizukami, Y. Ando, Y. Suzuki, Nat. Nanotechnol. 4 (2009) 158–161.

[66] M. Weisheit, S. Fähler, A. Marty, Y. Souche, C. Poinsignon, D. Givord, Science 315 (2007) 349–351.

[67] C.G. Duan, J.P. Velev, R.F. Sabirianov, Z. Zhu, J. Chu, S.S. Jaswal, E.Y. Tsymbal, Phys. Rev. Lett. 101 (2008) 137201.

[68] C.G. Duan, S.S. Jaswal, E.Y. Tsymbal, Phys. Rev. Lett. 97 (2006) 047201.

[69] A.B. V. Garcia, M. Bibes, L. Bocher, S. Valencia, F. Kronast, A. Crassous, X. Moya, S. Enouz-Vedrenne, A. Gloter, D. Imhoff, C. Deranlot, N. D. Mathur, S. Fusil, K. Bouzehouane, Science 327 (2010) 1106–1110.

[70] H. Béa, M. Bibes, F. Ott, B. Dupé, X.H. Zhu, S. Petit, S. Fusil, C. Deranlot, K.

Bouzehouane, A. Barthélémy, Phys. Rev. Lett. 100 (2008) 017204.

[71] Y.-H. Chu, L.W. Martin, M.B. Holcomb, M. Gajek, S.-J. Han, Q. He, N. Balke, C.-H. Yang, D. Lee, W. Hu, Q. Zhan, P.-L. Yang, A. Fraile-Rodríguez, A. Scholl, S.X. Wang, R. Ramesh, Nat. Mater. 7 (2008) 478–82.

[72] S.M. Wu, S.A. Cybart, P. Yu, M.D. Rossell, J.X. Zhang, R. Ramesh, R.C. Dynes, Nat. Mater. 9 (2010) 756–761.

[73] P. Yu, J.S. Lee, S. Okamoto, M.D. Rossell, M. Huijben, C.H. Yang, Q. He, J.X. Zhang, S.Y. Yang, M.J. Lee, Q.M. Ramasse, R. Erni, Y.H. Chu, D. a. Arena, C.C. Kao, L.W. Martin, R. Ramesh, Phys. Rev. Lett. 105 (2010) 027201.

[74] C. Thiele, K. Dörr, O. Bilani, J. Rödel, L. Schultz, Phys. Rev. B 75 (2007) 054408.

[75] N.A. Spaldin, Magnetic Materials Fundamentals and Applications, Cambridge University Press, 2011.

[76] F. Zavaliche, T. Zhao, H. Zheng, F. Straub, M.P. Cruz, P.L. Yang, D. Hao, R. Ramesh, Nano Lett. 7 (2007) 1586–1590.

[77] Y. Zhang, Z. Wang, Y. Wang, C. Luo, J. Li, D. Viehland, J. Appl. Phys. 115 (2014) 084101.

[78] G.D. Zhu, K.L. Wong, J. Zhao, P.K. Amiri, K.L. Wang, J. Hockel, G.P. Carman, J. Zhu, I. Krivorotov, J. Appl. Phys. 112 (2012) 033916.

[79] S.W. Yang, R.C. Peng, T. Jiang, Y.K. Liu, L. Feng, J.J. Wang, L.Q. Chen, X.G. Li, C.W. Nan, Adv. Mater. 26 (2014) 7091–7095.

[80] T. Wu, A. Bur, P. Zhao, K.P. Mohanchandra, K. Wong, K.L. Wang, C.S. Lynch, G.P. Carman, Appl. Phys. Lett. 98 (2011) 012504.

[81] T. Wu, A. Bur, K. Wong, P. Zhao, C.S. Lynch, P.K. Amiri, K.L. Wang, G.P. Carman, Appl. Phys. Lett. 98 (2011) 262504.

[82] J.H. Park, Y.K. Jeong, S. Ryu, J.Y. Son, H.M. Jang, Appl. Phys. Lett. 96 (2010) 192504.

[83] T.X. Nan, Z.Y. Zhou, J. Lou, M. Liu, X. Yang, Y. Gao, S. Rand, N.X. Sun, Appl. Phys. Lett. 100 (2012) 2010–2013.

[84] J. Lou, M. Liu, D. Reed, Y. Ren, N.X. Sun, Adv. Mater. 21 (2009) 4711–4715.

[85] M. Liu, Z.Y. Zhou, T.X. Nan, B.M. Howe, G.J. Brown, N.X. Sun, Adv. Mater. 25 (2013) 1435–1439.

[86] M. Liu, S.D. Li, O. Obi, J. Lou, S. Rand, N.X. Sun, Appl. Phys. Lett. 98 (2011) 222509.

[87] M. Liu, O. Obi, J. Lou, Y.J. Chen, Z.H. Cai, S. Stoute, M. Espanol, M. Lew, X. Situ, K.S. Ziemer, V.G. Harris, N.X. Sun, Adv. Funct. Mater. 19 (2009) 1826–1831.

[88] J.J. Yang, Y.G. Zhao, H.F. Tian, L.B. Luo, H.Y. Zhang, Y.J. He, H.S. Luo, Appl. Phys. Lett. 94 (2009) 212504.

[89] S. Geprägs, A. Brandlmaier, M. Opel, R. Gross, S.T.B. Goennenwein, Appl. Phys. Lett. 96 (2010) 142509.

[90] J.W. Lee, S.C. Shin, S.K. Kim, Appl. Phys. Lett. 82 (2003) 2458–2460.

[91] W. Eerenstein, M. Wiora, J.L. Prieto, J.F. Scott, N.D. Mathur, Nat. Mater. 6

(2007) 348–351.

[92] S. Sahoo, S. Polisetty, C.G. Duan, S.S. Jaswal, E.Y. Tsymbal, C. Binek, Phys. Rev. B - Condens. Matter Mater. Phys. 76 (2007) 092108.

[93] Y. Chen, T. Fitchorov, Z. Cai, K.S. Ziemer, C. Vittoria, V.G. Harris, J. Phys. D. Appl. Phys. 43 (2010) 155001.

[94] T.K. Chung, G.P. Carman, K.P. Mohanchandra, Appl. Phys. Lett. 92 (2008) 112509.

[95] C.-J. Hsu, J.L. Hockel, G.P. Carman, Appl. Phys. Lett. 100 (2012) 092902.

Chapter 4

4 Experimental Techniques

In this chapter, all the main experimental techniques used in this project are introduced. It is split into three sections: sample preparation, microstructural characterization and magnetic characterization. These techniques include radio frequency (RF) magnetron sputtering, Atomic Force Microscopy (AFM), X-ray diffraction (XRD), Focused Ion Beam (FIB), transmission electron microscopy (TEM) and magneto-optic Kerr effect (MOKE) measurement, including a high voltage set-up measurement designed specifically for this work.

4.1 Sample Preparation

The thin magnetic films ($Co_{50}Fe_{50}$ and Metglas $Fe_{81}B_{13.5}Si_{3.5}C_2$) were sputtered onto either 380 ± 50 μm thick (001) Si substrate with the native oxide in place or 500 μm ± 50 μm thick polished (001) and (011) lead magnesium niobate-lead titanate (PMN-PT) [1,2] substrates at room temperature by RF magnetron sputtering in a Nordiko NM2000 RF deposition system (section 4.1.1). To achieve a smooth surface, the PMN-PT was cold-mounted into an epoxy resin mixed with the epoxy hardener after being wrapped with Poly (methyl methacrylate) (PMMA). The cold-mounted PMN-PT was then polished on an Automet grind and polish equipment by using a series of polish suspensions. The PMMA was dissolved away using acetone and then the PMN-PT was taken out of the hardened resin. A mean surface roughness achieved 1.31±0.08 nm, measured by AFM (see section 4.2.1). The polished PMN-PT was cleaned prior to use with n-Butyl acetate, acetone and isopropanol (IPA).

The film thickness was determined by the growth rate, which was calculated by measuring a step height divided by the growth time. The step height was measured by AFM (section 4.2.1) in tapping mode and then confirmed by the cross-sectional TEM (section 4.2.4) image.

For the electric field (E-field) controlled magnetization measurement, top and bottom electrodes were made on the PMN-PT substrate. Conductive silver paint was used as the top electrode, which was brushed by hand leaving a space for the laser reflection for the MOKE measurement (section 4.3), as shown in **Fig. 4.1**. Au or Ag was used as the bottom electrode (Au electrode was made by the supplier and Ag electrode was made by the sintering process in Functional ceramic lab, University of Sheffield).

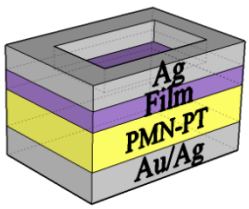

Fig. 4.1 Schematic of the prepared sample for E-field controlled magnetization measurement. Typical dimensions: PMN-PT (see Table 4.1), Au/Ag electrodes thickness (~ few tens μm) and the area for the laser reflection (~ 3 × 3 mm^2 or ~ 6 × 3 mm^2).

In addition, in this project, there were three different PMN-PT substrates used (named as PMN-PT1, PMN-PT2 PMN-PT3) classified by different composition and crystal cut, as listed in the **Table 4.1**. The PMN-PT1 substrate is (001) oriented and produces an isotropic strain (ε) along two in-plane directions [100] and [010] due to

the piezoelectric constant $d_{31} \approx d_{32} \approx -1000$, while both PMN-PT2 and PMN-PT3 are (011) oriented and produce an anisotropic ε along [100] and [01-1] due to an opposite sign of d_{31} and d_{32}. However, the piezoelectric response to the E-field for PMN-PT2 and PMN-PT3 are still different due to a possible compositional and manufacturing differences. **Fig. 4.2** shows the ε along different crystalline directions when a positive E-field is applied on the crystals. Here, the positive E-field is defined along the pre-poled direction of the ferroelectric crystal.

Table 4.1 A comparison of three different PMN-PT substrates used in the project.

Single crystal	**PMN-PT1**	**PMN-PT2**	**PMN-PT3**
PMN-xPT	x ≈ 0.28	x ≈ 0.28	x ≈ 0.30
Crystal orientation	(001)	(011)	(011)
Size (mm)	5 × 5 × 0.4	10 × 5 × 0.5	10 × 5 × 0.5
Piezoelectric constant (pC/N)	$d_{31} \approx d_{32} \approx -1000$ [3]	d_{31} = -1500 ~ -2000 d_{32} = 500 ~ 700	d_{31} = -1200 ~ -1800
Bottom electrode	Au	Ag	Au
Commercial Supplier	Morgan Technical Ceramics [4]	Atom Optics Co., Ltd. [5]	CTG Advanced Materials [6]

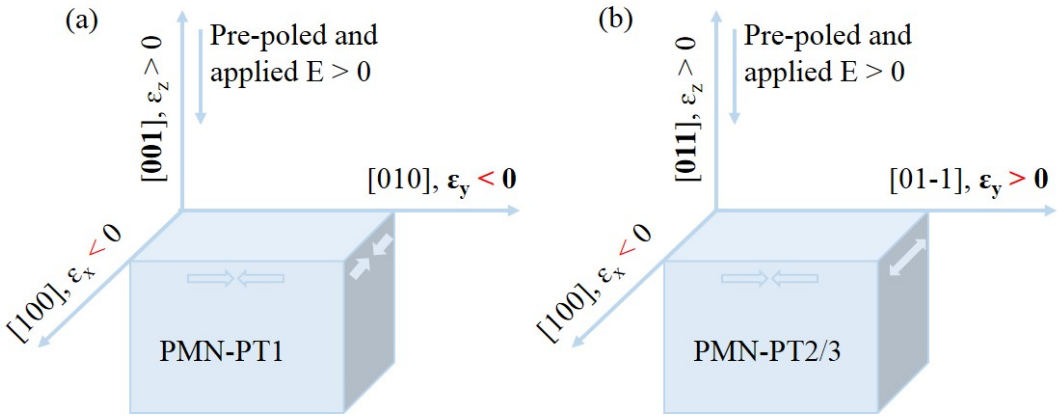

Fig. 4.2 The expected piezoelectric stain (ε) along x, y and z axis in the PMN-PT1 (a) and PMN-PT2/3 (b), according to the piezoelectric constants shown in Table 4.1. The positive sign of the ε represents a tensile strain while the negative sign represents a compressive strain.

4.1.1 RF Magnetron Sputtering

Sputtering is one of the most common physical vapour deposition (PVD) techniques for fabricating thin films onto substrates, because the sputtered films tend to be more uniform and dense with a fine grain size (~ 10 nm) compared to other PVD methods [7]. **Fig. 4.3** shows a schematic of a magnetron sputtering system. In this system, there is a cathode metal target (CoFe alloy, Metglas or Ti, in this project) to be deposited and an anode substrate (Si or PMN-PT, in this project). The former is connected to the negative terminal of a power supply, typically about few kilovolts (kV), while the latter may be grounded or biased positively [8]. The chamber is first pumped down to a vacuum with the base pressure about 10^{-7} Torr and then the working gas (normally, argon) is introduced and serves as a visible glow discharge medium between two electrodes. In the discharge, positive gas ions and electrons are produced and form a plasma. The ions strike the target and physically remove the

target atoms. The target atoms enter and pass through the plasma region to eventually deposit onto the substrate and to form the film [8]. The sputtering can be characterized by the sputtering yield [9], which is calculated by the number of emitted atoms divided by that of incident energetic ions [10]. Sputtering methods include commonly direct current (DC) (magnetron) sputtering and RF (magnetron) sputtering. Normally, the former is used to sputter conductive materials, while the latter is used to sputter non-conductive materials. For magnetron sputtering [11], electrons and ions are trapped near the target by a magnetic field (H-field) to increase the plasma density and thus the deposition rate.

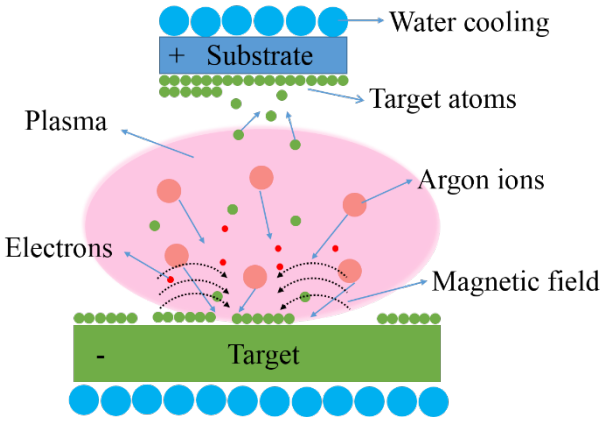

Fig. 4.3 A principle schematic of the RF magnetron sputtering system used. The target atoms are physically removed and eventually deposited onto the substrate.

The film properties are affected by various deposition parameters, such as working pressure, sputtering power, substrate material, temperature and substrate-target distance. The pd product is the working pressure (p) multiplied by the substrate-target distance (d) and has been shown to affect the stress in the film to be either

compressive or tensile, which then affects the magnetic properties of the film [12]. In addition, Thornton et al. [13] systematically studied the effect of the substrate temperature and the inert gas pressure on the microstructure of coating, as shown in **Fig. 4.4**. Basically, higher substrate temperature tends to favour the formation of larger grain boundaries because of grain re-crystallization, while higher inert gas pressure produces more voids in the film [14].

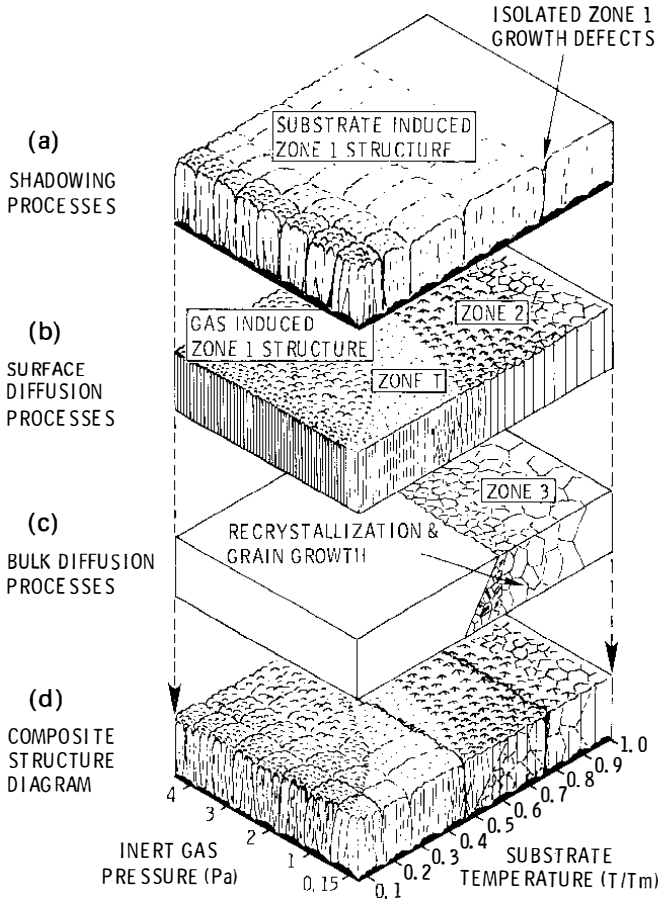

Fig. 4.4 Zone models proposed by Thornton et al. predicting coating microstructure dependence on both substrate temperature and working gas pressure. T: substrate temperature, T_m: the melting point of deposited materials [13].

In this project, the sputtering power parameter was experimentally studied. **Fig. 4.5** shows the effect of the sputtering power on the magnetic properties of the thin CoFe films. The coercive field of 3.34 kA/m at the sputtering power of 200 W is much larger than the coercive field of 0.88 kA/m for the sputtering power of 150 W. The power dependence of magnetic properties are discussed further in section 5.2 and section 6.1.

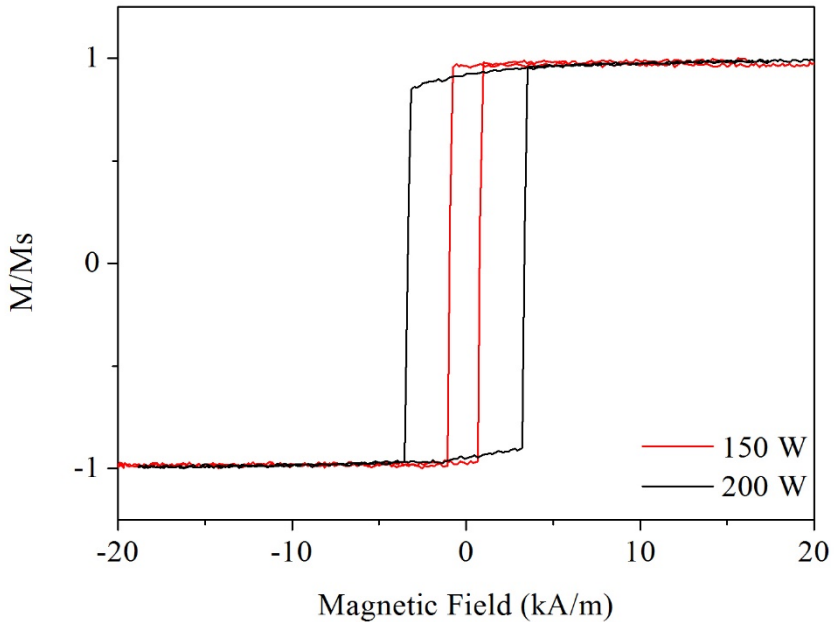

Fig. 4.5 An effect of the sputtering power (150 W and 200 W) on the magnetic properties of 65 nm CoFe on Si substrate.

In this project, the Nordiko RF magnetron sputtering system was chosen to sputter the CoFe and Metglas film onto the Si substrate with the native oxide layer present and the polished PMN-PT substrates. The Nordiko has an operating power range from 10 to 500 W and a working pressure range from 2 to 10 mTorr (Argon gas). For the Nordiko, the minimum working pressure where a stable plasma and uniform

film growth can be obtained is 4.5 mTorr. The targets used were polycrystalline $Co_{50}Fe_{50}$ alloy and amorphous METGLAS® 2605SC [15] foil with the $Fe_{81}B_{13.5}Si_{3.5}C_2$ composition. Before the film deposition, the targets were pre-sputtered for 15 min to remove the surface absorption and other impurities, so that high quality films were obtained. The sputtering power, working pressure and base pressure were 75W, 5.0 ± 0.1 mTorr and 1.2 ± 0.2 × 10^{-3} mTorr, respectively. The growth temperature was almost room temperature. An in-situ H-field of 65.3 kA/m was applied along an in-plane direction of the Si or PMN-PT substrate. The sample was not rotated during growth. To study the effect of a buffer layer on the magnetoelectric coupling strength (Chapter 7), a thin Ti layer (0-10 nm) was deposited on the explorer 14 coating system (located at Kroto Innovation centre), which is a customized vacuum deposition system and controlled by a programmable logic controller (PLC). The base pressure was 2 × 10^{-3} mTorr. The working gas flow rate was 60 sccm and the Dc current was 800 mAmps. The sample was rotated within the deposition process with a rotation speed of 50%. The pre-sputter time was 90 seconds.

4.2 Microstructural Characterization

To investigate the microstructure of the heterostructures, XRD measurements (section 4.2.2) were made using a Siemens D5000 X-ray diffractometer with CuK_α radiation (λ = 1.54056 Å). To further understand the microstructure and interface in the heterostructures in more detail, cross-sectional TEM (section 4.2.4) was undertaken on both FEI Tecnai T20 and Jeol 2010F operating at 200 kV. The TEM specimen was prepared by FIB (section 4.2.3) in a FEI Quanta 200 3D. The surface topography of the thin films was observed in the AFM tapping mode [16] (section

4.2.1).

4.2.1 Atomic Force Microscopy

AFM is a technique which allows the observation and measurement of sample surface structure with a high resolution (0.1 nm) in z direction and accuracy. For example, an arrangement of individual atoms or molecules can be shown in an AFM image. Besides, compared to the other techniques (SEM, TEM) AFM does not need any extreme conditions such as a vacuum environment. There are three main AFM modes discussed: contact mode, non-contact mode and tapping mode [17].

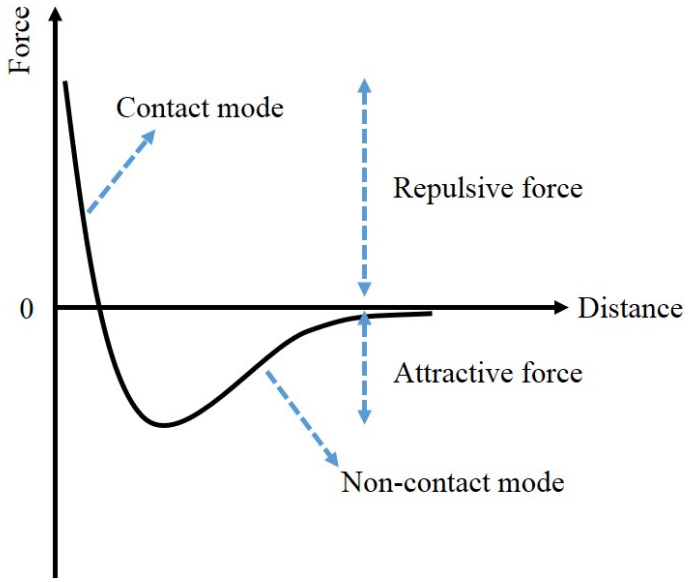

Fig. 4.6 Simplified Van der Waals force-distance curve showing both contact mode regime and non-contact mode regime.

AFM in contact mode is the simplest and first developed [18]. It can also rapidly image the sample topography because no oscillation measurements are required. In

contact mode, the tip attached to the end of a cantilever is always in contact with the sample surface. As the tip is gently scanned across the sample, the repulsive force, as shown in **Fig. 4.6**, causes the cantilever deformation to accommodate changes in sample height [17]. The deformation of the cantilever can be monitored using a position-sensitive photodetector which detects the laser reflection off the back of the cantilever as it changes, as shown in **Fig. 4.7**. This information is recorded and transferred as the topography of the sample. A piezoelectric scanner is driven by a feedback loop to compensate the change of the cantilever, i.e. moving the tip up or down, so to keep the deflection of the cantilever constant. However, for contact mode, both the tip and the sample can be damaged during the scanning process due to the forces involved between the tip and the sample surface.

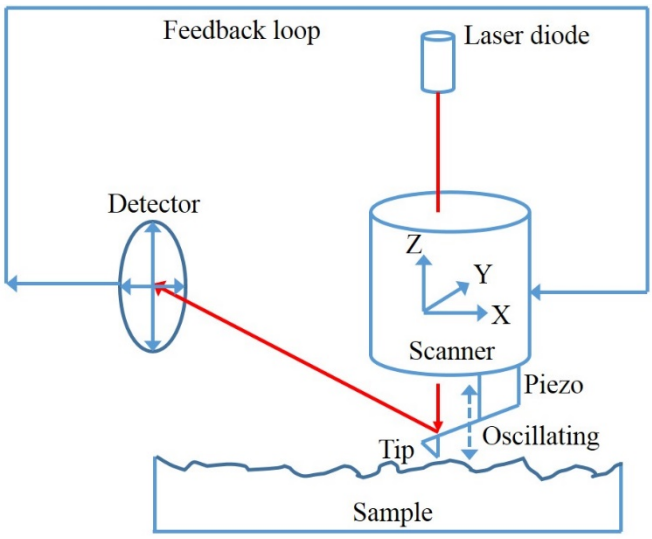

Fig. 4.7 Schematic of tapping mode AFM. The position-sensitive photodetector detects the cantilever deformation by the laser reflection off the back of the cantilever change. The piezoelectric scanner is driven to move up and down by the feedback loop to compensate the change of the cantilever.

In non-contact mode, a stiff AFM cantilever vibrates close to the sample surface spacing on the order of few to ten of nanometres. The vibration frequency of the cantilever is near its resonant frequency, typically 100-400 kHz [17]. The attractive force between the tip and the sample, as shown in **Fig. 4.6**, will cause changes in the cantilever's resonant frequency and vibration amplitude, which are detected by the system to determine the sample topography. Although the non-contact mode avoids the damage sample compared to the contact mode, a contamination layer present on most sample surfaces in air may lower the image resolution. Therefore, ultra-high vacuum non-contact AFM has been used for a true atomic resolution.

Tapping mode AFM is the most commonly used method among all AFM modes because it overcomes the part of the limitations of both non-contact and contact AFM. For example, tapping mode eliminates lateral forces and thus avoids damaging the sample surface and increases image resolution [17]. In tapping mode AFM, the tip oscillates as in non-contact mode, but its oscillation amplitude (typically, a few tens nanometres) is much larger than the non-contact mode amplitude. As a result tapping mode can allow the tip to pass through the contamination layer to contact the sample surface and measure a real sample topography at atmosphere.

In this project, the surface topography and thickness of thin films were obtained using tapping mode AFM on the Veeco Dimension 3100. The Si cantilever is coated by reflective Aluminium (Al) for enhancing the laser reflectivity, with the resonance frequency f_o of 270-313 kHz. The tip radius is about 7 nm, which is smaller than the typical grain size of thin films (> 10 nm) [19] and thus ensures the accurate measurement. The grain size, the root mean squared roughness (R_{rms} or R_q), the arithmetic roughness (R_a) and film thickness were obtained using the Nanoscope

software for AFM data analysis, as shown in **Fig. 4.9** (a), (b) and **Fig. 4.8**. For the film thickness measurement, a step was first created by putting one drop of PMMA onto the substrate before growing the thin film. After the deposition, the PMMA was dissolved in acetone and thus a hole was left. As the tip scanned across the hole, the step height was measured and used as the film thickness, as shown in **Fig. 4.8**, the film thickness was ~ 99.8 nm.

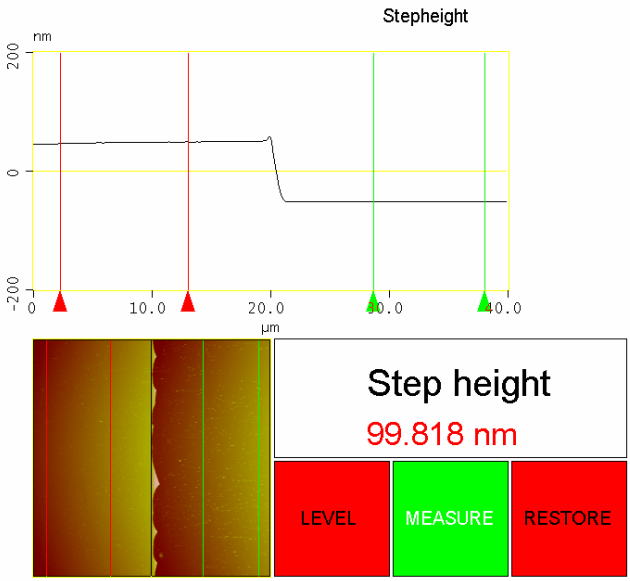

Fig. 4.8 AFM step height analysis with a scan area 30*30 μm^2. Two red lines were firstly moved to determine a level on one side of the step and then two green lines were moved to measure on the other side of the step.

The grain size was estimated by drawing a line through a few grains, along which two red triangle symbols were moved. Finally the surface distance gave an approximate grain size, 78.5 nm as shown in **Fig. 4.9** (a).

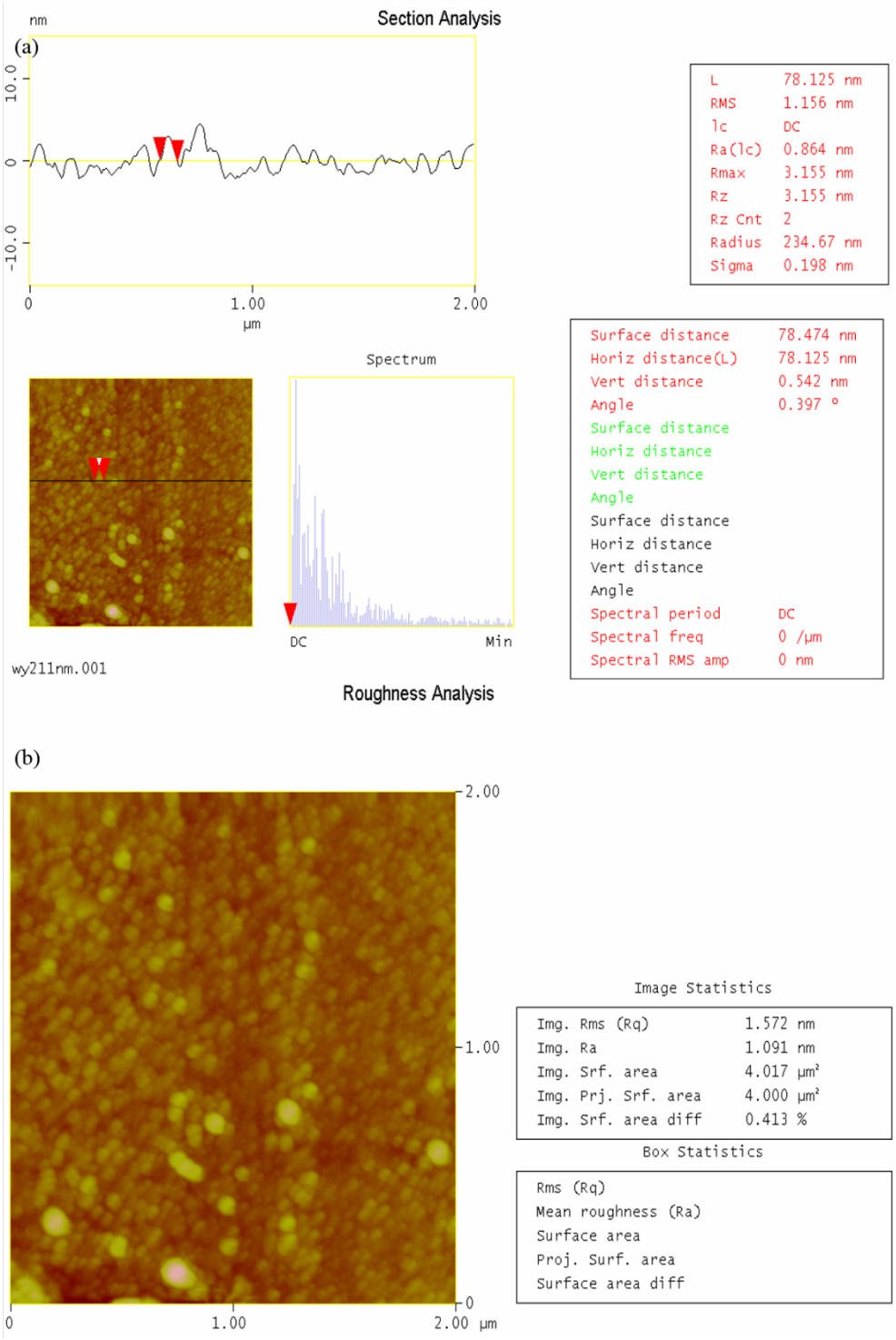

Fig. 4.9 Cross-sectional analysis (a) and roughness analysis (b) of the 211 nm thick NiFe film AFM.

4.2.2 X-ray Diffraction

When a monochromatic X-ray beam irradiates a family of atomic planes, the waves in the X-ray beam can be diffracted. The diffraction condition is that the path differences ($\delta = 2d_{hkl}\sin\theta$) between the waves scattered by the atomic planes obey Bragg's Law $2d\sin\theta = n\lambda$. The d_{hkl} is the interplanar distance. The θ and λ is the X-ray beam incident angle and the wavelength, respectively. The n is an integer representing the order of diffraction [20,21]. In this project, XRD measurements were made on the samples using a Siemens D5000 X-ray diffractometer with CuK_α radiation (λ = 1.54056 Å). A simplified schematic of X-ray diffractometer is shown in **Fig. 4.10**.

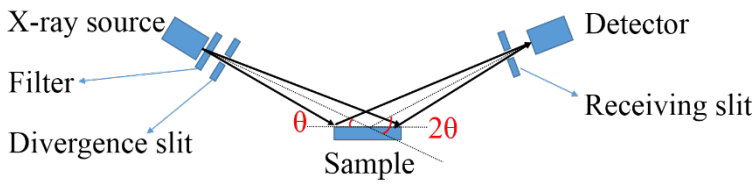

Fig. 4.10 Simplified schematic of X-ray diffractometer in θ-2θ Bragg reflection geometry.

First, for the Cu target in the X-ray tube, the X-ray beam has the Kβ radiation filtered out using a Ni filter. Before and after incidence on the sample the beam was collimated with both divergence slit and anti-scattering slit of 0.6° wide, which is set according to the dimension of the sample. The X-ray diffractometer was run at scan speed of 0.5 deg/min. The obtained XRD results from the diffractometer were analyzed by the PDF-4 + 2014 software. A typical XRD peak and the corresponding PDF card are shown in **Fig. 4.11**.

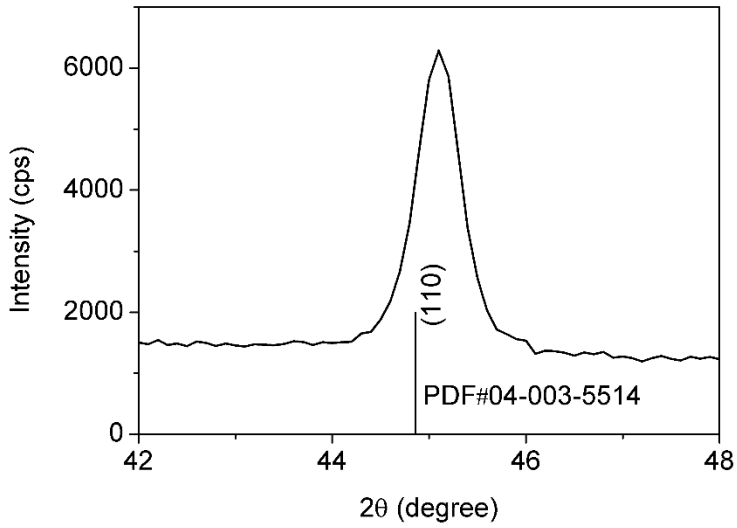

Fig. 4.11 A typical XRD peak of the 65 nm CoFe thin film sputtered at 200 W and 30 nm Metglas underlayer sputtered at 75 W on the Si substrate.

The structure phase, texture, lattice parameter and minimum grain size can be identified and estimated from the XRD pattern. For example, in a cubic crystal, the lattice constant (a) is calculated by the combination of Bragg law $2d\sin\theta = n\lambda$ and $d_{hkl} = \frac{a}{\sqrt{h^2+k^2+l^2}}$. The minimum grain size (t) is estimated by the Scherrer formula:

$$t = \frac{0.9\lambda}{B\cos\theta_B} \tag{4.1}$$

where the B is the full width at the half maximum (FWHM) of the diffraction peak, Bragg angle θ_B is the diffraction peak position and λ is the X-ray wavelength. In addition, the shift and broadening of diffraction peaks can indicate the presence of compressive or tensile stress in the films. For the homogeneous strain (i.e. uniform compressive or tensile strain), the diffraction peak position will shift to a higher or lower Bragg angle, respectively, because the lattice plane spacing (d) is reduced or increased, respectively according to Bragg law. However, for the inhomogeneous

strain, the diffraction peak is broadened because non-uniform strain causes non-uniform interplanar spacing.

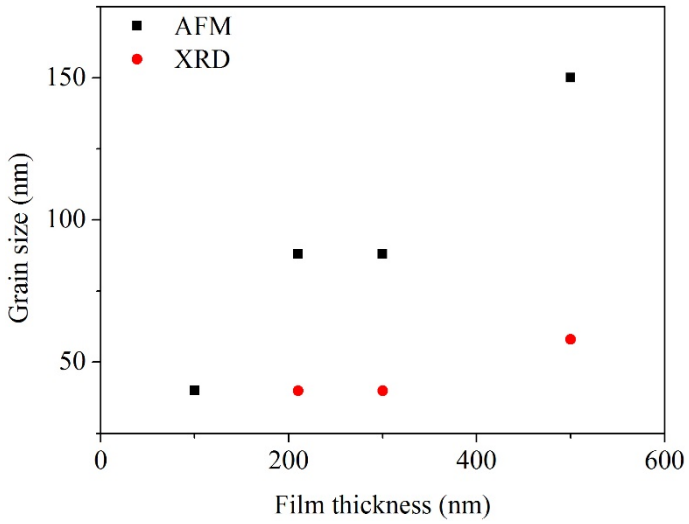

Fig. 4.12 The grain size observed from AFM (black square) and calculated from XRD results by Scherrer formula (red circle) with the varying film thickness from 100 nm to 500 nm NiFe films.

Fig. 4.12 shows that the grain size obtained from AFM is greater than that from the XRD results using the Scherrer formula. As mentioned above, the broadening of diffraction peak is contributed from both grain size effects and inhomogeneous strain effects. Therefore, the extra contribution from inhomogeneous strain causes the difference between AFM results and XRD results using Scherrer formula. Hence, only a minimum grain size can be determined from the XRD results. However, AFM results only reflect the grain size on the surface plane. Generally, a grain has three dimensions and thus the AFM results also cannot give a true grain size. Therefore, in

this project, the grain size measured from the cross-sectional TEM image is regarded as the real grain size.

4.2.3 Focus Ion Beam (FIB)

FIB was used to prepare TEM samples, as it has a number of advantages, which include being able to prepare large site-specific samples with uniform thickness required for TEM observation [22]. Moreover, most materials can be prepared by the FIB method, such as metals, ceramics and composites. However, FIB also has its disadvantages, these include the milling process that can cause ion implantation, damage and artifacts [23] to the remaining material [22]. The damage can be reduced by using broad low-energy Ar ion beam milling [24,25] or low-energy FIB [25].

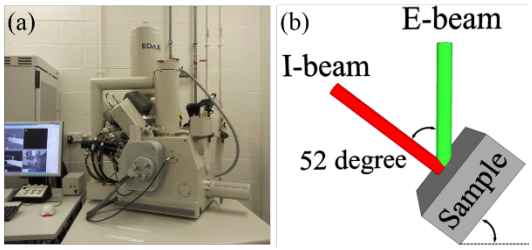

Fig. 4.13 (a) A photograph of FEI Quanta 200 3D at Sorby center, University of Sheffield. (b) A schematic (not to scale) of Ion-beam (I-beam) and Electron-beam (E-beam) when the sample was tilted 52^{o} at the eucentric height for the ion milling.

In this project, cross-sectional TEM specimens were prepared by FIB in FEI Quanta 200 3D (**Fig. 4.13** (a)) which combines a scanning electron microscope (SEM) operating at 20 kV and a FIB microscope operating at 30 kV. These two microscopes observe the sample from two different directions (**Fig. 4.13** (b).) and thus allows 3D

characterization, which is important in the operation for the TEM specimen preparation.

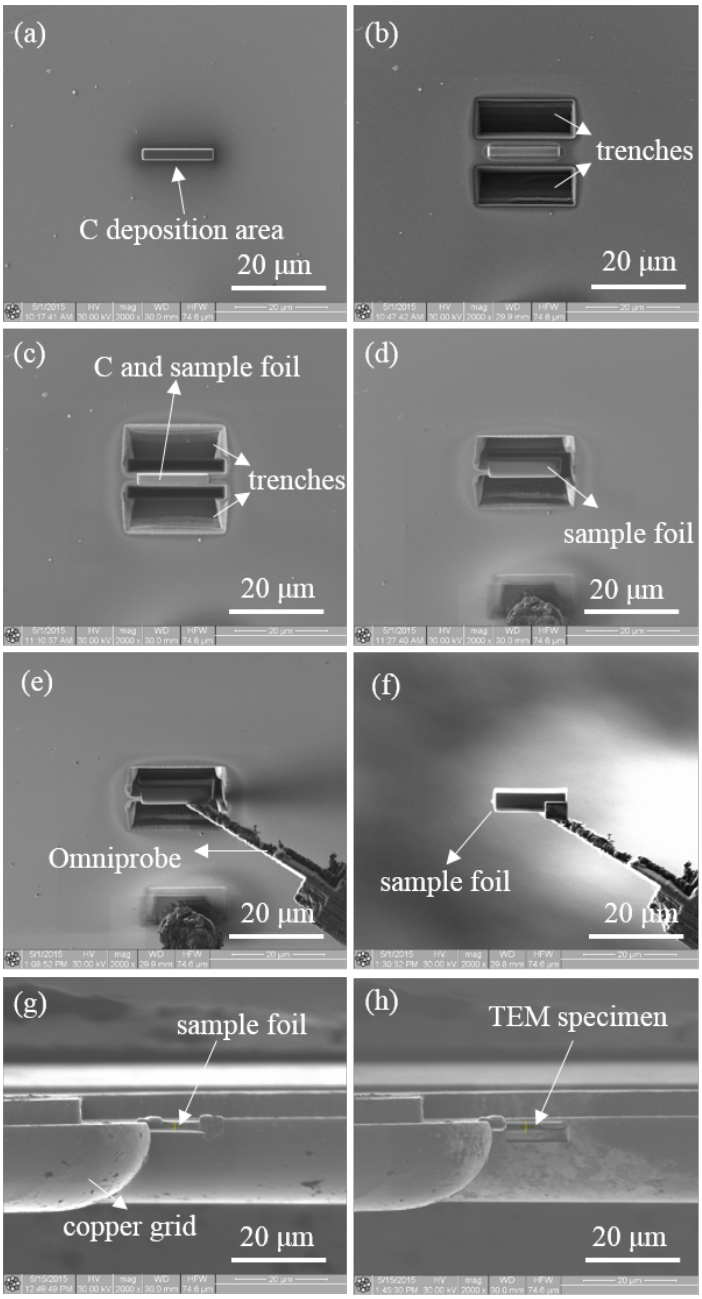

Fig. 4.14 Ion beam images of the different TEM specimen preparation stages. (a) A carbon deposition strip (typically, 15 × 2 × 2 μm^3) as a protective cover by a heated up Gas injector on the sample surface. (b) and (c) Both trenches above and below the deposition strap dug

by high currents' ion beams (5 nA and 3 nA). (d) The sample foil cut out along underneath and the right edge. (e) The Omniprobe driven to contact a sample foil. (f) The sample foil lifted out. (g) The sample foil attached on the cantilever of a TEM copper grid. (h) The sample foil finally milled by a series of low currents' ion beams from 0.5 nA to 30 pA.

The FIB system can not only produce high resolution images but also can precisely mill the sample material, due to the gallium (Ga^+) ion beam (energy range typically from 25-50 keV [26]) hitting the sample surface and sputtering the sample material little by little. The sputtering rate depends on how large the current is used. Although, some sputtered material can be redeposited on another part of the sample.

In the preparation process (shown in **Fig. 4.14**), firstly, an area of 15 × 2 μm^2 on the sample (**Fig. 4.14** (a)) is covered with a 2 μm thick carbon layer by inserting the carbon Deposition Gas Injector System (GIS). Two 20 × 8 × 4 μm^3 trenches about 1 μm away from the deposited strap (**Fig. 4.14** (b)) were dug by the ion milling with a high ion current of 5 nA. Then, these two trenches were expanded to the edges of the C strap (**Fig. 4.14** (c)) by the ion milling with a relative low ion current of 3 nA. To cut off the sample foil from underneath, the sample stage was tilted back from 52 degrees to 7 degrees, and then foil was cut through along the whole underneath and the right edge (**Fig. 4.14** (d)). Next, the Omniprobe was driven to touch the foil (**Fig. 4.14** (e)), and then sample was connected to the probe by C deposition. Following this, the left edge was cut out so that the foil was only attached to the probe and ready for lifting out. In **Fig. 4.14** (f), the sample foil was lifted out by dropping the sample stage and retracting the probe. Then the sample foil was stuck to the cantilever of a TEM grid (**Fig. 4.14** (g)) again by C deposition. Finally, it was

gradually thinned by varying current ion beam from 0.5 nA to 30 pA (**Fig. 4.14** (h)). At the stage of final milling, the foil was tilted around 52°, which means the milling was carried out at almost a glancing angle (< 1°) for reducing the Ga implantation into the foil to a minimum.

4.2.4 Transmission Electron Microscopy

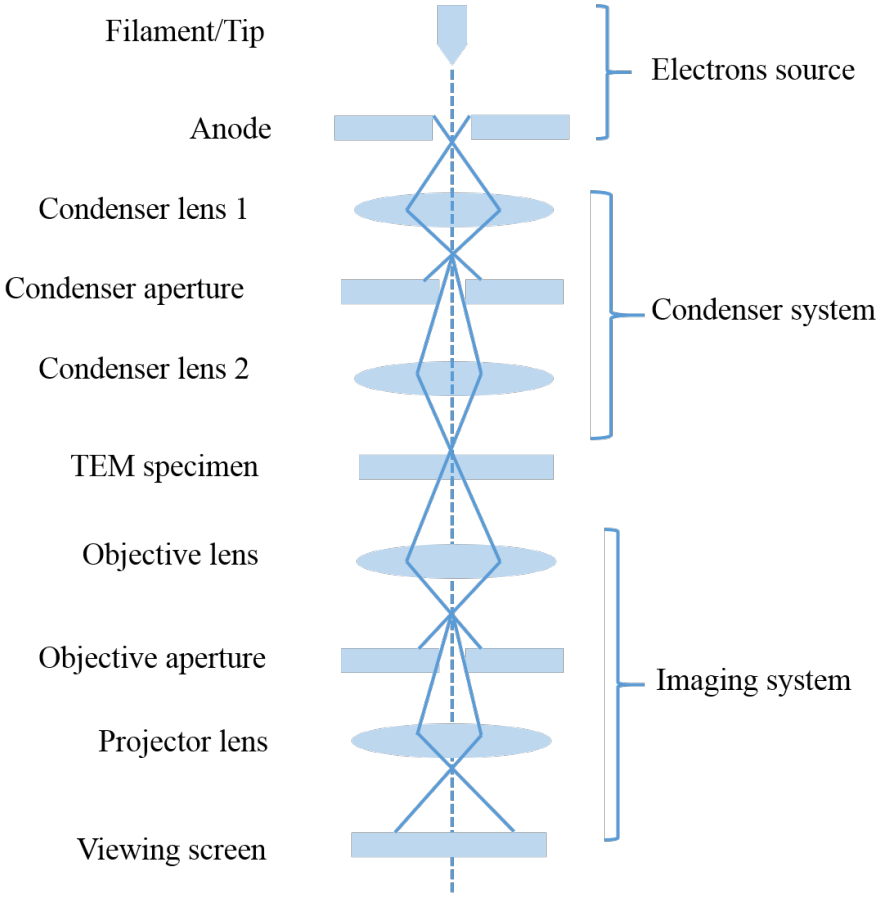

Fig. 4.15 A schematic of basic components in a TEM. There are main three systems: Electron gun, Condenser system and Imaging system.

Cross-sectional TEM was undertaken to investigate the microstructure and interfaces in the heterostructures. **Fig. 4.15** shows the basic structure of a TEM. Firstly, an E-

beam is produced by accelerating the electrons in the electron gun. There are two kinds of electron sources which are the thermionic electron gun and the field emission electron gun [27]. The latter can give a much higher source brightness than the former but it requires a very good vacuum [28]. The accelerated E-beam is concentrated by the condenser lens before it reaches the ultrathin specimen. Then, the E-beam passes through the specimen and interacts with it, as shown in **Fig. 4.16**. Next, an image is formed by the objective lens and then is further magnified by the subsequent projector lens and finally displayed onto the viewing electron-fluorescent screen or CCD [27].

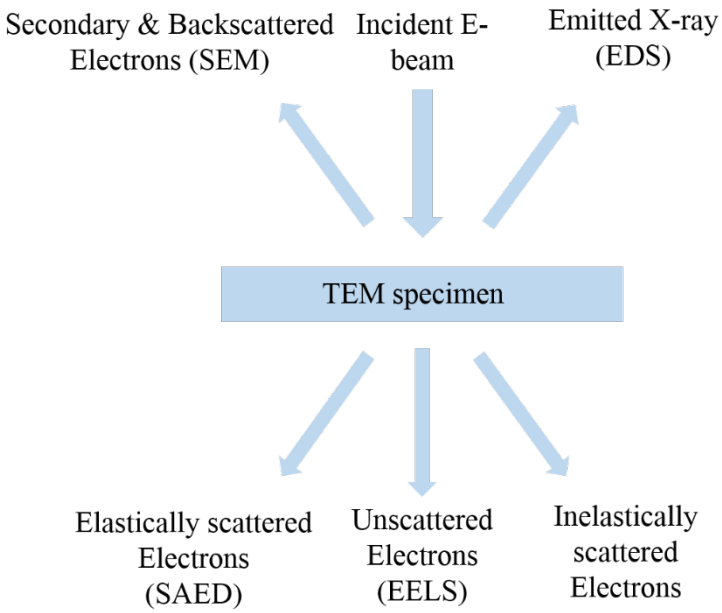

Fig. 4.16 A simplified summary of the interaction with the TEM specimen when the E-beam transmits through the specimen.

The interaction of the E-beam with the TEM specimen produces many useful effects [29], which can be used to analysis and characterize materials. For example,

elastically scattered electrons are diffracted by the crystal planes and thus form diffraction patterns. Based on the diffraction results, structural information about the crystals can be deduced. Similar to the X-ray diffraction, Bragg's Law $2d\sin\theta_e = \lambda_e$ is also applicable for electrons diffraction. Besides, the θ_e is much smaller in the electrons diffraction than that in the X-ray diffraction due to the two orders smaller λ_e value for the E-beam. For the small diffraction angle θ_e, Bragg equation is rewritten as:

$$2d\sin\theta_e = 2d\theta_e = \lambda_e \tag{4.2}$$

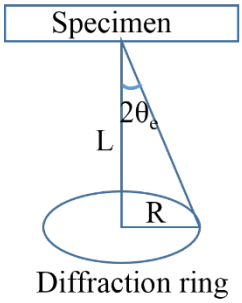

Fig. 4.17 A schematic diagram indicating the geometry of diffraction patterns formation. θ_e: diffraction angle, R: diffraction ring radius and L: camera length.

Similarly, based on the diffraction geometry (**Fig. 4.17**) of the TEM, another equation can be determined in terms of λ_e and is written as:

$$\frac{R}{L} = \tan 2\theta_e = 2\theta_e \tag{4.3}$$

Combining the equation 3.2 and the equation 3.3, a third equation relating the lattice spacing and the diffraction ring radius observed is given by [27]:

$$Rd = L\lambda_e \tag{4.4}$$

where the $L\lambda_e$ is the camera constant (e.g. $L\lambda_e$ = 860 mm used on the FEI Tecnai T20). The R and d are the radius of the diffraction ring and the crystal plane space, respectively. Therefore, the d can be calculated when the R is measured. For the cubic crystal, the d can be described by the crystal plane indices as [30]:

$$d_{hkl} = \frac{a}{\sqrt{h^2 + k^2 + l^2}} \tag{4.5}$$

where the a is crystal lattice parameter and the (hkl) is the crystal plane Miller indices. The indices can be deduced when the d is calculated.

Based on the theory described above, the crystal plane indices can be identified, as shown in **Fig. 4.18** (b). The CoFe film showed a polycrystalline structure with the (110) texture. Also, columnar growth structure of CoFe film was observed in **Fig. 4.18** (a). Therefore, the TEM is a powerful technique to determine the microstructure of thin films.

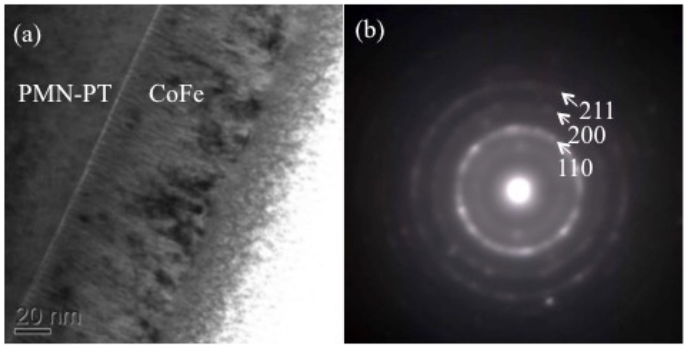

Fig. 4.18 A TEM image (a) and a diffraction pattern (b) of CoFe thin film grown on PMN-PT substrate.

4.3 Magneto-Optical Kerr Effect Magnetometer

A MOKE magnetometer [31] is a simple, non-destructive instrument, which is operated at room temperature and is used to determine the normalized magnetization loop of a magnetic film [32]. When a light beam is incident on a magnetic sample, the electromagnetic waves in the light are subjected to a Lorentz force generated by the magnetization in the sample. Thus the polarization of the reflected light is rotated. The alteration of the polarization state can be detected and used to show the magnetization variation.

There are three basic configurations (polar, longitudinal and transverse) of the MOKE magnetometer classified by the relative orientation of the magnetization (M) with the incident light plane [33]. In both polar MOKE and longitudinal MOKE, the orientation of the M is parallel to the incident plane, while in transverse MOKE, it is perpendicular to the incident plane. The difference between polar MOKE and longitudinal MOKE is that the M direction for the former is out-of-plane, while that for the latter is in-plane, as shown in **Fig. 4.19**.

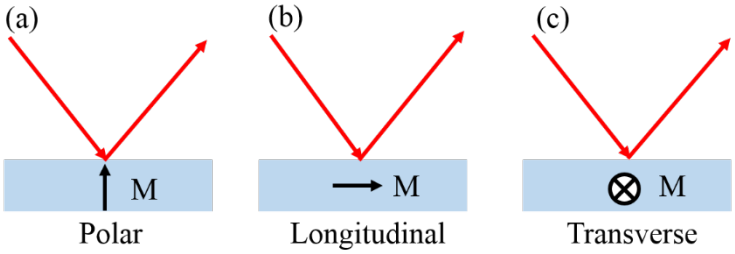

Fig. 4.19 Three basic geometries of magneto-optical Kerr effect. The red arrows represent the direction of the incident light and the reflective light.

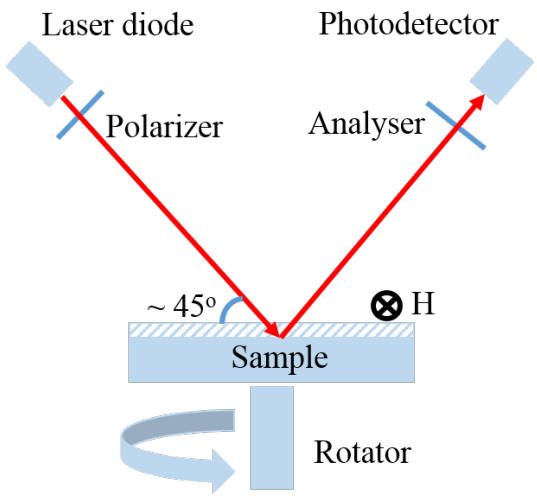

Fig. 4.20 A schematic of transverse MOKE magnetometer used in this study. The shaded area represents the depth of laser penetration or the skin depth.

In this project, the transverse geometry MOKE was used for magnetic characterization, which is sensitive to the in-plane component of magnetization perpendicular to the plane of laser incidence. The Kerr signal measured close to the extinction point is linearly proportional to the Kerr effect and thus the magnetization of the film. [14] The MOKE set-up used (**Fig. 4.20**) includes a solid state laser diode of wavelength 635 nm. The skin depth of the laser is about ~ 30 nm at this wavelength for metallic films. The laser first passes through a polarizer before hitting the film. The polarizer angle was set at a certain value so that the laser has s and p mixed polarization. After reflecting from the film, the laser beam passed through an analyser. The analyser angle was set close to the extinction point (normally deviating about 2^{o}) for a symmetric hysteresis loop. Finally, the reflected laser was detected by a photodetector. The sample was mounted on a sample stage with a precise angle rotator, which allows the sample to be rotated between 0-360^{o} in a uniform H-field, this allows magnetic anisotropy to be investigated. Also, a well-

polished substrate surface was required to avoid laser scattering and to enhance the signal to noise ratio.

4.3.1 Magnetostriction Measurement

Magnetostriction measurements [34,35] include a direct measurement and an inverse measurement. For the direct measurement, cantilever bending is used as a high-precision technique [34]. The sample is first cut to be a long cantilever (typically 38 mm × 8 mm) that is then clamped at one end by a sample holder. When a H-field is applied parallel or perpendicular to the cantilevered sample, it will be deflected due to the magnetostriction effect. The deflection of the sample can be measured using a position sensitive optical detector that detects an angular change of a reflective laser off the free end of the cantilever.

Compared to the direct measurement, the inverse measurement does not have a limitation to the size and shape of the sample. When an anisotropic stress (σ) is applied to the thin film sample, a change in the anisotropy field (ΔH_k) occurs due to the inverse magnetostriction effect (i.e. the Villari effect). The relationship between the ΔH_k and the saturation magnetostriction constant (λ_s) can be given by [34]

$$\Delta H_k = 3\frac{\lambda_s}{M_s}\,\sigma \tag{4.6}$$

where M_s is the saturation magnetization and σ is the applied mechanical stress.

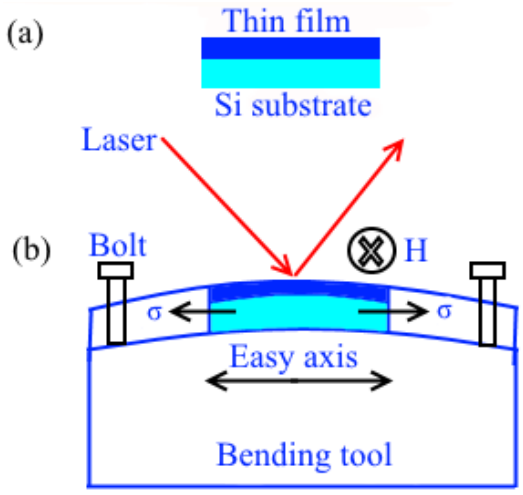

Fig. 4.21 A schematic of the bending process for the magnetostriction measurement. (a) A sample without bending and (b) The sample with bending.

In this project, the effective saturation magnetostriction constants (λ_{eff}) of polycrystalline films were measured using a technique [36,37] based on the Villari effect, as shown in **Fig. 4.21**. The sample was strained along the easy axis by bending tools with different known radii R, i.e. 500 mm, 400 mm and 300 mm. MOKE measurements were taken along the hard axis at each bend radius. With decreasing radius, the σ gradually increases and thus the magnetization along the hard axis becomes harder and harder due to a positive magnetostriction value of the CoFe and the Metglas films, as shown in **Fig. 4.22**.

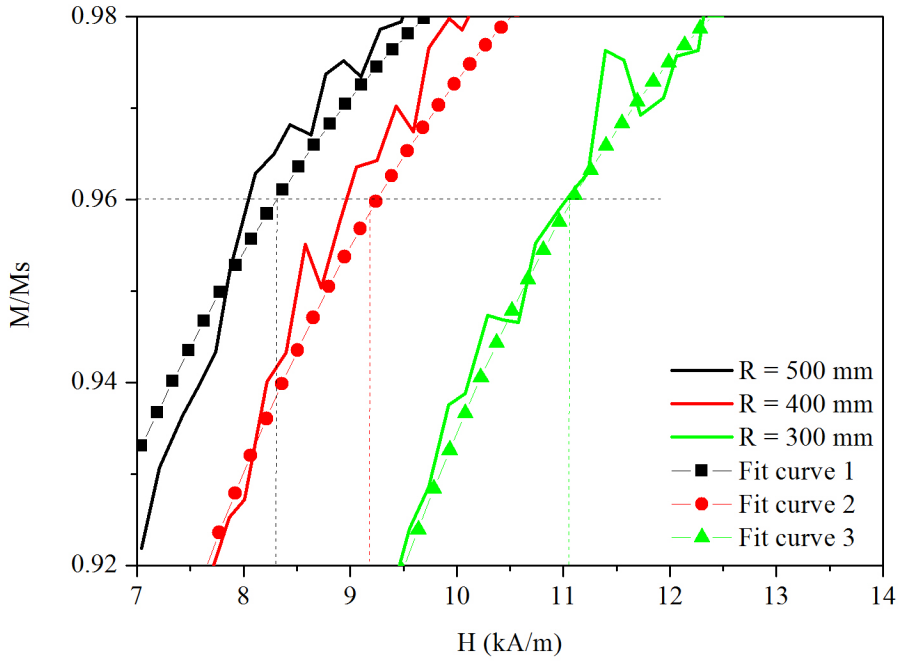

Fig. 4.22 A part of MOKE loops measured along the hard axis. A polynomial curve was fitted for the acquisition of an accurate H_{eff}.

In **Fig. 4.22**, for each loop, the effective saturation fields H_{eff} were taken at M_r/M_s = 0.96, 0.97 and 0.98 where the H_{eff} was close to the anisotropy field H_k at M_r/M_s = 1. Besides, MOKE signal at these values was less noisy than that close to saturation state and thus it was relatively precise to determine H_{eff} at M_r/M_s = 0.96, 0.97 and 0.98. These H_{eff} were plotted as a function of the inverse band radii (1/R). In order to accurately obtain the value of $dH_{eff}/d(1/R)$, a linear fit analysis was made for these three M_r/M_s values in the Originpro 8 plotting software, as shown in **Fig. 4.23**.

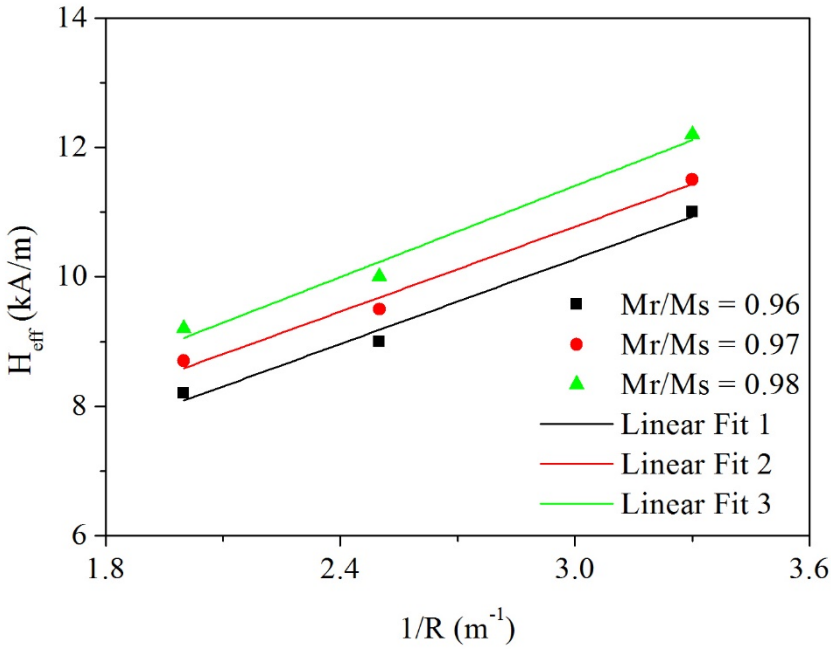

Fig. 4.23 The variation of the H_{eff} as a function of the 1/R at M_r/M_s = 0.96, 0.97 and 0.98, respectively. A linear was fitted for the calculation of $dH_{eff}/d(1/R)$ by the Originpro 8 software.

Then the gradient of each line was determined after the linear fit process, as shown in the **Table 4.2**. The average value of $dH_{eff}/d(1/R)$ was calculated. Finally, the λ was determined from [36,37]

$$\lambda = \frac{dH_{eff}}{d(1/R)} \frac{2\mu_o M_s(1-{v_s}^2)}{3t_s Y_s} \tag{4.7}$$

Where the saturation induction $\mu_o M_s$ was 2.4 T [38]. The Poisson ratio v_s and Young's modulus Y_s for (100) Si substrate were 0.28 and 130 GPa [39,40]. The Si substrate thickness t_s was 380 ± 50 μm. This method has been shown to produce accurate measurements of the effective magnetostriction constant of magnetic films [36,41].

Table 4.2 The results from the linear fit process by the Originpro 8 software.

Mr/Ms	**$dH_{eff}/d(1/R)$**	**Standard Error**
0.96	2.19	0.24
0.97	2.19	0.24
0.98	2.35	0.31

4.4 High Voltage Set-Up for the Converse ME effect

To study the converse ME coupling effect, a high voltage (a maximum of 850 V) was applied to the piezoelectric PMN-PT substrate so that a large strain was created in the sample. Then the effect of the strain on the magnetic properties of the thin films were investigated. Therefore, for this project, a high voltage set-up was built up within the MOKE magnetometer. As shown in **Fig. 4.24**, the H-field was applied along the in plane direction of the PMN-PT, while the voltage was applied along the out of plane direction of the sample.

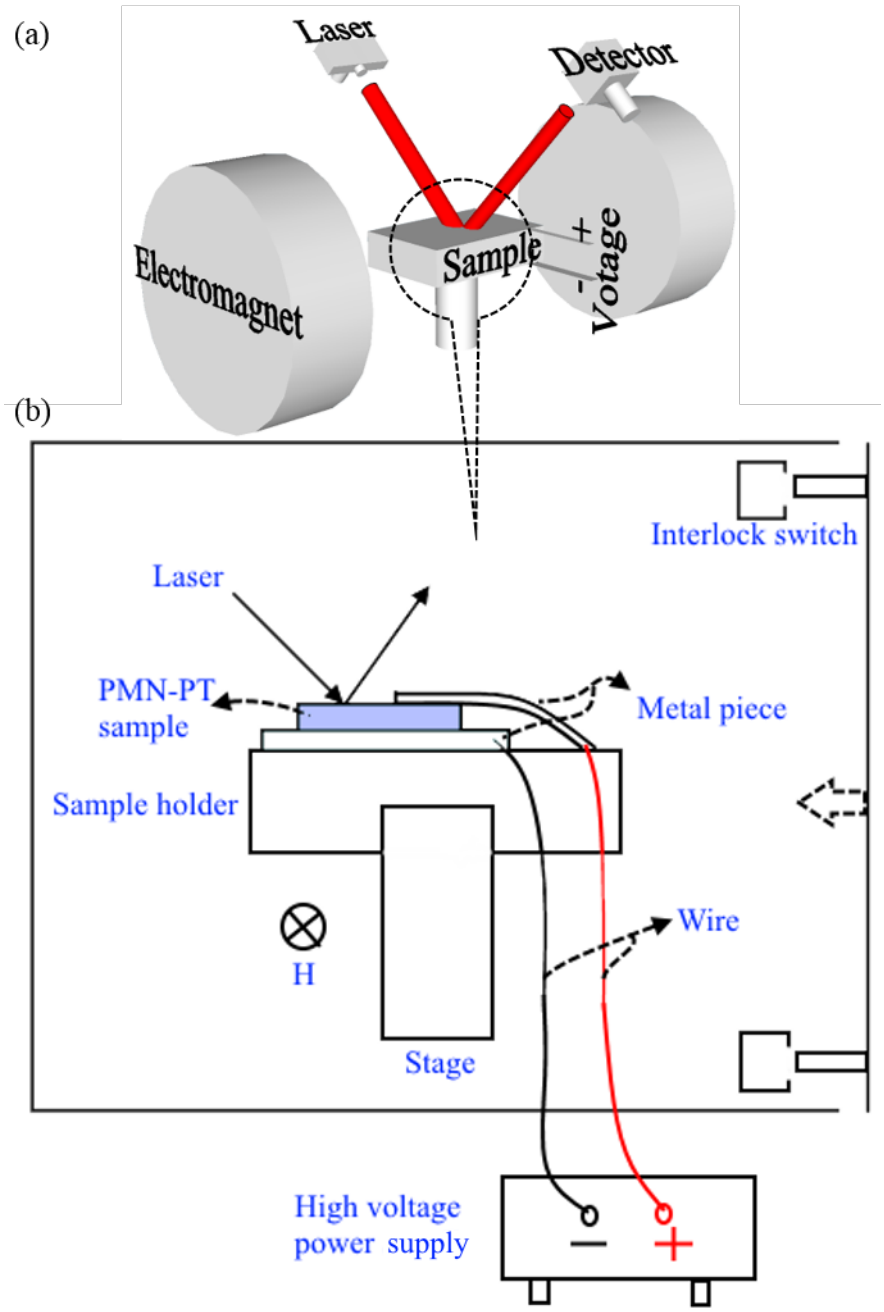

Fig. 4.24 (a) A simplified schematic (not to scale) of High-field transverse geometry MOKE system. A voltage was applied on the sample when the converse ME effect was characterized. (b) A schematic of high-voltage set-up designed in the high H-field MOKE magnetometer.

Fig. 4.24 (b) shows a detailed diagram which explains how the high voltage was applied to the sample safely for a hysteresis loop to be measured. A custom made plastic sample holder sat on the metal columnar stage. Two thin metal pieces were fitted on the sample holder and used as two electrodes. Then the sample was clamped firmly between them so that a good contact was obtained between the sample surfaces and the electrodes. Before loading the sample into the MOKE, a multimeter was used to check all connections. Finally, these two electrodes were connected with a high voltage supply (Model: PS310/1250 V-25 W). For safety reasons, the sample could only be accessed from the back side of the MOKE where a wooden safety shield was positioned. The power supply could only be turned on when the shield was put in place by an interlock switch.

4.5 References

[1] L.H. Luo, H.X. Wang, Y.X. Tang, X.Y. Zhao, Z.Y. Feng, D. Lin, H.S. Luo, J. Appl. Phys. 99 (2006) 024104.

[2] P. Han, W. Yan, J. Tian, X. Huang, H. Pan, Appl. Phys. Lett. 86 (2005) 052902.

[3] Y. Chen, T. Fitchorov, Z. Cai, K.S. Ziemer, C. Vittoria, V.G. Harris, J. Phys. D. Appl. Phys. 43 (2010) 155001.

[4] M.T. Ceramics, Http://www.morgantechnicalceramics.com.

[5] L. Atom Optics Co., Http://www.atomoptics-Sh.com.

[6] C.A. Materials, Http://www.hcmat.com.

[7] K.S.S. Harsha, Principles of Physical Vapor Deposition of Thin Films, Amsterdam ; Oxford : Elsevier, 2006.

[8] M. Ohring, Materials Science of Thin Films : Deposition and Structure, 2nd ed. San Diego, CA : Academic Press, 2002.

[9] N. Matsunami, Y. Yamamura, Y. Itikawa, N. Itoh, Y. Kazumata, S. Miyagawa, K. Morita, R. Shimizu, H. Tawara, At. Data Nucl. Data Tables 31 (1984) 1–80.

[10] M. Nastasi, J. Mayer, J.K. Hirvonen, Ion-Solid Interactions Fundamentals and Applications, Cambridge University Press, 1996.

[11] K. Kawabata, T. Tanaka, A. Kitabatake, K. Yamada, Y. Mikami, H. Kajioka, K. Toiyama, J. Vac. Sci. Technol. A Vacuum, Surfaces, Film. 19 (2001) 1438–1441.

[12] C. Hudson, R.E. Somekh, Mater. Res. Soc. Symp. Proc. 239 (1992) 145–150.

[13] J.A. Thornton, Annu. Rev. Mater. Res. 7 (1977) 239–260.

[14] A. Javed, Magnetic Properties of Fe-Ga Thin Films, University of Sheffield (Thesis (Ph.D.)), 2010.

[15] H.T. Savage, M.L. Spano, J. Appl. Phys. 53 (1982) 8092–8097.

[16] J.M. Balthazar, A.M. Tusset, S.L.T. de Souza, A.M. Bueno, Proc. Inst. Mech. Eng. Part C-Journal Mech. Eng. Sci. 227 (2013) 1730–1741.

[17] Veeco, A Practical Guide to SPM Scanning Probe Microscopy, 2005.

[18] P. Eaton, Atomic Force Microscopy, Oxford : Oxford University Press, 2010.

[19] H.S. Jung, W.D. Doyle, J.E. Wittig, J.F. Al-Sharab, J. Bentley, Appl. Phys. Lett. 81 (2002) 2415–2417.

[20] R. Guinebretière, X-Ray Diffraction by Polycrystalline Materials, London ; Newport Beach, CA : ISTE, 2007.

[21] J.P. Glusker, Crystal Structure Analysis, Oxford University Press, 2010.

[22] J. Mayer, L. a Giannuzzi, T. Kamino, J. Michael, MRS Bull. 32 (2007) 400–407.

[23] Y.J. Xiao, F.Z. Fang, Z.W. Xu, X.T. Hu, Appl. Surf. Sci. 343 (2015) 56–69.

[24] Z. Huang, J. Microsc. 215 (2004) 219–223.

[25] N.I. Kato, J. Electron Microsc. (Tokyo). 53 (2004) 451–458.

[26] L.A. Giannuzzi, F.A. Stevie, Introduction to Focused Ion Beams : Instrumentation, Theory, Techniques, and Practice, New York : Springer,

2005.

[27] P.J. Goodhew, J. Humphreys, R. Beanland, Electron Microscopy and Analysis, Taylor & Francis, 2001.

[28] P. Goodhew, Http://www.matter.org.uk/tem/default.htm.

[29] C. Colliex, Comptes Rendus Phys. 15 (2014) 101–109.

[30] U. Shmueli, Theories and Techniques of Crystal Structure Determination, Oxford University Press, 2007.

[31] D.A. Allwood, G. Xiong, M.D. Cooke, R.P. Cowburn, J. Phys. D-APPLIED Phys. 36 (2003) 2175–2182.

[32] N.A. Morley, M.R.J. Gibbs, E. Ahmad, I. Will, Y.B. Xu, J. Magn. Magn. Mater. 300 (2006) 436–444.

[33] J. McCord, J. Phys. D. Appl. Phys. 48 (2015) 333001.

[34] A.C. Tam, H. Schroeder, IEEE Trans. Magn. 25 (1989) 2629–2638.

[35] A. Raghunathan, J.E. Snyder, D.C. Jiles, IEEE Trans. Magn. 45 (2009) 3269–3273.

[36] A. Javed, N.A. Morley, M.R.J. Gibbs, J. Magn. Magn. Mater. 321 (2009) 2877–2882.

[37] N.A. Morley, A. Javed, M.R.J. Gibbs, J. Appl. Phys. 105 (2009) 07A912.

[38] S. Rengarajan, E.J. Yun, W.S. Kang, R.M. Walser, J. Appl. Phys. 81 (1997) 4761–4763.

[39] D.R. França, a Blouin, Meas. Sci. Technol. 15 (2004) 859–868.

[40] S. Lampenscherf, W. Pompe, D.S. Wilkinson, J. Am. Ceram. Soc. 83 (2000) 1333–1340.

[41] N.A. Morley, A.C. Finkel, W. Yang, N. Reeves-mclaren, IEEE Trans. Magn. 50 (2014) 2503704.

Chapter 5

5 Giant electric field tunable magnetic properties in $Co_{50}Fe_{50}$/lead magnesium niobate-lead titanate multiferroic heterostructure

In this chapter, the effect of magnetic layer thickness on magnetoelectric (ME) coupling in $Co_{50}Fe_{50}$/PMN-PT heterostructures was investigated over a wide thickness range from 30 nm to 100 nm. CoFe film was chosen to be the ferromagnetic (FM) layer due to its excellent soft magnetic properties, relatively high magnetostriction [1,2] and large saturated magnetization [3]. The (011) oriented PMN-PT [4] was chosen as the ferroelectric (FE) substrate due to its large in-plane anisotropic strains. The effect of magnetic layer thickness on the ME coupling in the heterostructures was studied independently, due to almost constant magnetostriction constant ($\lambda = 40 \pm 5$ ppm) and similar as-grown magnetic anisotropy for all studied magnetic layer thicknesses in this chapter. A high remanence ratio (M_r/M_s) tunability of 95% was demonstrated in the 65 nm CoFe/PMN-PT heterostructure, corresponding to a α value of 2.5×10^{-6} s/m, ten times larger than that in the CoPd/(001) PMN-PT system [5].

5.1 Sample Preparation and characterization process

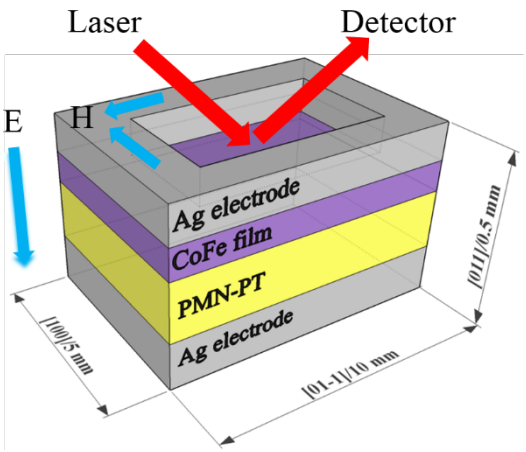

Fig. 5.1 Schematic of CoFe/500 μm (011) PMN-PT heterostructure. Magnetic properties were measured by the MOKE system.

CoFe films of 30 nm, 45 nm, 65 nm and 100 nm thickness were deposited on the (011) PMN-28% PT (i.e. PMN-PT2, see for **Table 4.1** the substrate's more information) at room temperature by RF sputtering in a Nordiko NM2000 RF deposition system (see section 4.1.1 for further details). An in-situ H-field of 65.3 kA/m was applied along the [100] or [01-1] crystallographic direction of the PMN-PT substrate during the growth of the CoFe film. The PMN-PT was prepoled through the thickness (i.e. along the [011] direction) at an E-field of 5 kV/cm for 10 minutes before being used as a substrate. The prepoling processing was to align most dipoles along the poling direction rather than randomly arrange, which provided the material with the piezoelectric effect. Magneto-Optical Kerr Effect (MOKE) measurements were used to investigate the magnetic properties when a series of dc E-fields were applied to MF heterostructures (see section 4.3 and 4.4). The MOKE H-field was applied along the [100] or [01-1] direction of the PMN-PT, while the E-field was applied along [011] direction of the PMN-PT, as shown in **Fig. 5.1**. The effective saturation magnetostriction constants (λ_{eff}) were measured using a

technique [6,7] based on the Villari effect described in section 4.3.1. The magnetostriction constants were measured for the different thickness CoFe grown on Si, as it was difficult to measure the magnetostriction constant of CoFe when grown on PMN-PT.

To investigate the microstructure of the heterostructure, X-ray diffraction (XRD) measurements were made on the sample without the top Ag electrode by using a Siemens D5000 X-ray diffractometer with CuK_α radiation (λ = 1.54056 Å) (See section 4.2.2 for further details). Cross-sectional transmission electron microscopy (TEM) specimens were prepared by Focused Ion Beam (FIB) in FEI Quanta 200 3D (See section 4.2.3 for further details). The fabricated TEM specimens were observed on both FEI Tecnai T20 and Jeol 2010F operating at 200 kV (See section 4.2.4 for further details).

5.2 An optimal sputtering power

In this section, the optimal RF sputtering power (P) for soft magnetic properties was explored in the CoFe/Si heterostructure while other sputtering parameters (working pressure, sputtering temperature and target-substrate distance) were held constant. Many publications [8–11] have shown a large influence of the P on the microstructure and magnetic properties of thin films. Here, a soft and highly magnetostrictive CoFe thin film is desired to be fabricated by the optimal RF P, so that a large magnetoelectric coupling is obtained when the film is grown onto the PMN-PT substrate.

The effect of the sputtering power on the coercive field (H_c) and the effective saturated magnetostriction constant (λ_{eff}) is shown in **Fig. 5.2** for 65 nm and 30 nm CoFe films. In **Fig. 5.2**, when the P increases from 75 W to 200 W, the H_c increases

from 1 kA/m to 3.3 kA/m, while the λ_{eff} decreases slightly from 37.2 ± 1.4 ppm to 33.3 ± 2.4 ppm for 65 nm CoFe film. It is noted that the H_c increases obviously at the power of 200W compared to the H_c at the lower powers. The reason may be that more defects (like voids) are produced within the films and they have a pinning effect on the magnetization process. For the 30 nm CoFe, the H_c is lower than the 65 nm CoFe film at both 75 W and 200 W. These results indicate the effect of sputtering power on the magnetic softness is important for the thicker film at the higher deposition power.

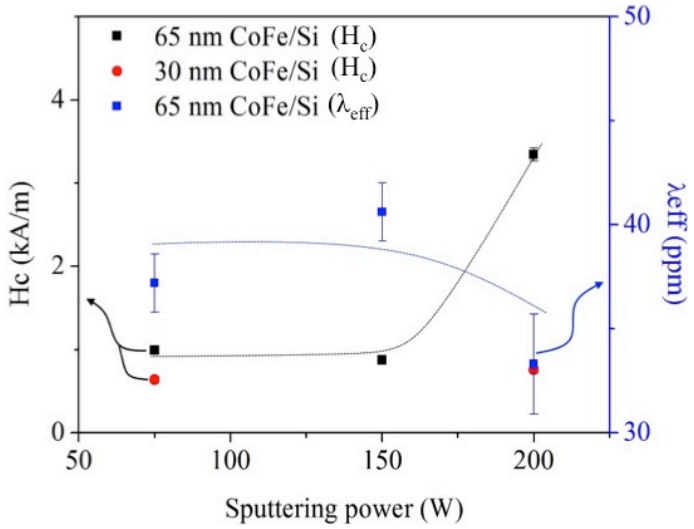

Fig. 5.2 An effect of the sputtering power (75 W, 150W and 200 W) on H_c measured along easy axis and λ_{eff} in 65 nm/Si heterostructure. The H_c of 30 nm CoFe/Si heterostructure is also shown.

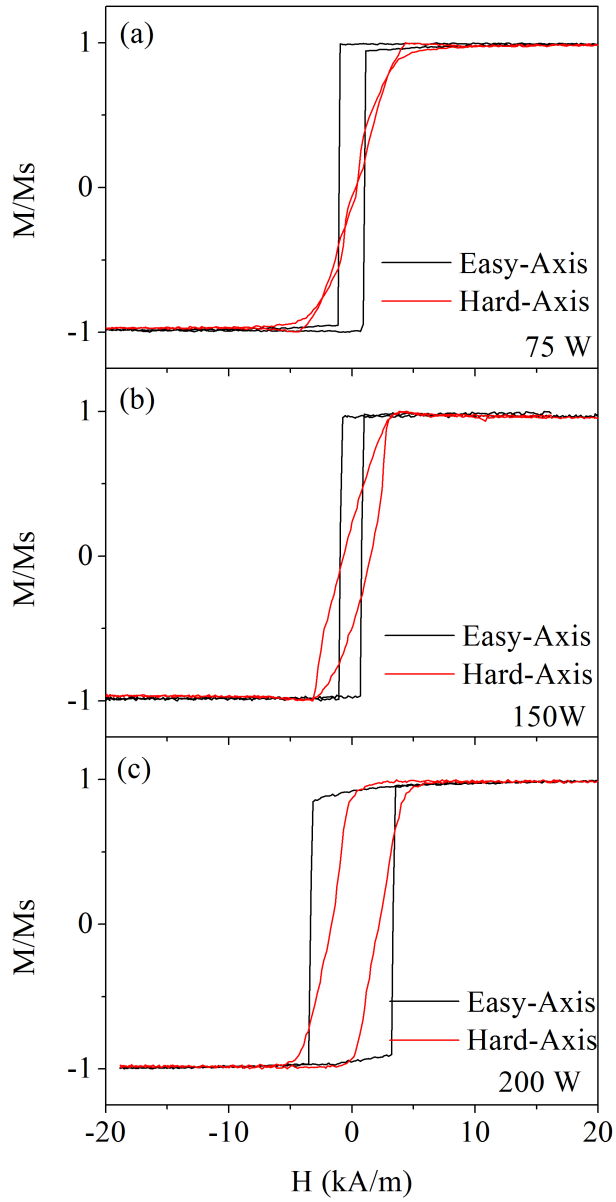

Fig. 5.3 The easy and hard axis loops of 65 nm CoFe grown on Si at the different powers.

In addition, the effect of the P on the film's in-plane anisotropy was also investigated. **Fig. 5.3** shows the in-plane magnetic anisotropy of 65 nm CoFe thin film sputtered at 75 W, 150 W and 200 W, respectively. It is clear that the anisotropy induced during deposition decreases gradually as the P increases. The anisotropy field H_k is reduced from 7 kA/m to 5.5 kA/m when the P increases from 75 W to 200 W. This may be

explained in terms of film growth mechanisms [12,13]. The higher P will induce a higher kinetic energy of the target atoms and thus increase the mobility of the atoms, which helps overcome the effect of the in-situ H-field on the orientation of atoms at the substrate. In the converse magnetoelectric coupling study, the in-situ H-field was used to control an as-grown anisotropy of thin films on the PMN-PT. Therefore, the lowest P of 75 W was chosen for this project. Moreover the soft magnetism and moderate magnetostriction were also obtained at the power of 75 W.

5.3 Microstructure of CoFe films and interface

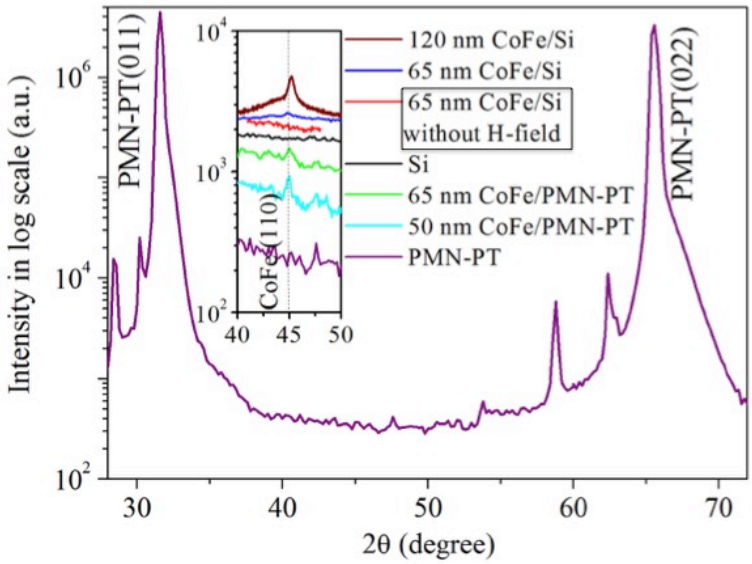

Fig. 5.4 XRD spectra of PMN-PT and Si substrates. The inset shows an enlarged part around the (110) diffraction peak of the CoFe films grown on the PMN-PT and Si substrates.

Fig. 5.4 shows the XRD result of both PMN-PT and Si substrates. It shows strong diffraction peaks for the (011) of PMN-PT substrate, respectively, which indicates the crystalline orientation of the substrates used in this study. The weak diffraction

peak (110) of CoFe film is seen only on a much smaller scale of intensity, as shown in the inset. This indicates the films are not grown epitaxially on both substrates as expected. In addition, 50 nm CoFe on the PMN-PT was scanned at a speed of 0.23 degree/min while all the rest of samples were scanned at the speed of 0.5 degree/min. There is no obvious difference for the 2θ position (2θ = 44.9^{o}, cited from PDF#04-003-5514) and the intensity of the (110) peak between 50 nm and 65 nm CoFe film grown on the PMN-PT. However, the (110) peak for the 65 nm CoFe grown on the Si is broader than its counterpart on the PMN-PT, which may be due to a non-uniform strain contribution, as discussed in section 4.2.2. Here, a difference between film growth with and without the in-situ H-field was also observed. The films grown with in-situ H-field show a stronger (110) diffraction peak than those without the in-situ H-field, which suggests the in-situ H-field applied in the process of the film growth induces a preferred orientation in the film and thus an anisotropy within the magnetic properties. When the film thickness is up to 120 nm, the (110) peak can be observed clearly due to a greater contribution from the thick film to the XRD. In the inset, the XRD results of only Si and PMN-PT substrates around 2θ of 45 degrees are also shown for a comparison with the films and to show the signal to noise ratio (SNR) of the data.

To further understand in more detail microstructure and interface in the heterostructure, cross-sectional TEM images obtained on FEI Tecnai T20 are shown in **Fig. 5.5** (a) and (b) and high-resolution transmission electron microscopy (HRTEM) images obtained on Jeol 2010F are shown in **Fig. 5.5** (c) and (d). Selected area electron diffraction (SAED) pattern are shown in **Fig. 5.5** (e) and (f). In **Fig. 5.5** (a), a native 1-2 nm thick SiO_2 layer present on the Si substrate can be clearly seen, which results in an increase of surface roughness. The 50 nm CoFe film's growth

structure (typically, a columnar growth) are not observed. In **Fig. 5.5** (b), the uniform columnar growth structure of 65 nm CoFe film is observed with an average columnar grain size of 3.3 ± 0.5 nm, which is comparable with that of ~5 nm in the Fe-Ga/PMN-PT system [14]. In addition, the cross-sectional TEM image of 50 nm CoFe grown on the PMN-PT was also done (not shown here but in Chapter **7**) and the film also shows the uniform columnar growth structure with the almost same average columnar grain size of 3.6 ± 0.5 nm. The columnar growth structure can be explained in term of the zone models [13]. The incident atoms shadow those atoms which already have incorporated into the growing thin film [8] at the low power sputtering with the low mobility of the atoms. In **Fig. 5.5** (c) and (d), the heterostructures show a well-defined interface between 65 nm CoFe film and the substrates. The films are not grown epitaxially on both substrates due to a large lattice misfit (CoFe (a_{CoFe} = 2.858 Å [15]), Si (a_{Si} = 5.43 Å) and PMN-PT (a_{PMN-PT} = 4.021 Å [16])), which is consistent with the XRD results (**Fig. 5.4**). The SAED patterns in **Fig. 5.5** (e) and (f) show the single crystalline structure of the PMN-PT and the polycrystalline structure of 65 nm CoFe film. In **Fig. 5.5** (f), it is observed that there are some spots on the diffraction ring, which suggests that the columnar grains are composed of randomly oriented nanocrystals. The crystal line plane of (110) in CoFe film shows the strongest diffraction, which is consistent with XRD results of CoFe film.

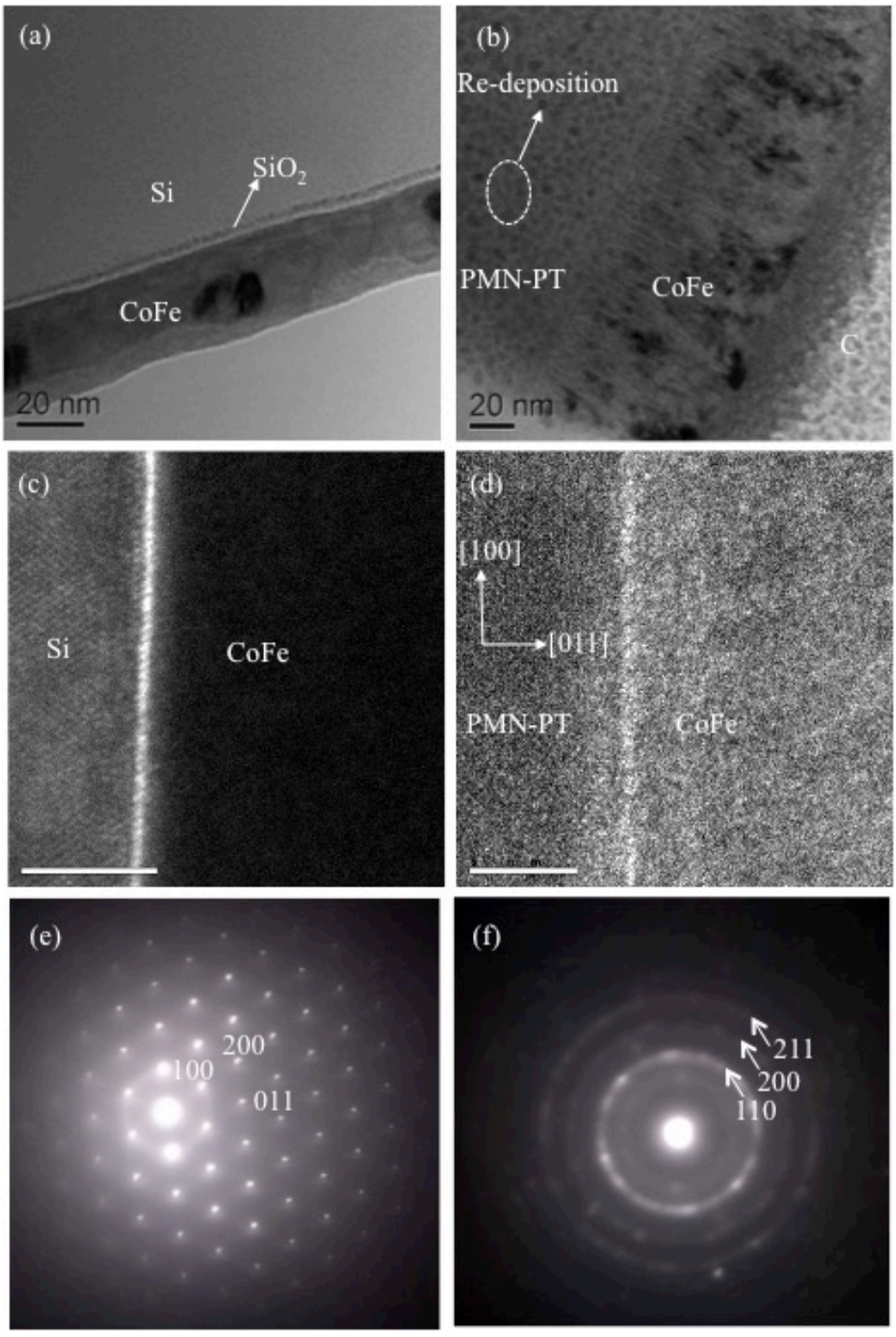

Fig. 5.5 (a) and (b) cross-sectional TEM image of the 50 nm CoFe/Si and 65 nm CoFe/PMN-PT heterostructures. (c) and (d) cross-sectional HRTEM image of 65 nm CoFe/Si and 65 nm CoFe/PMN-PT heterostructures. (e) and (f) show the SAED patterns of PMN-PT and 65 nm CoFe film, respectively.

5.4 Electric field controlled magnetic properties

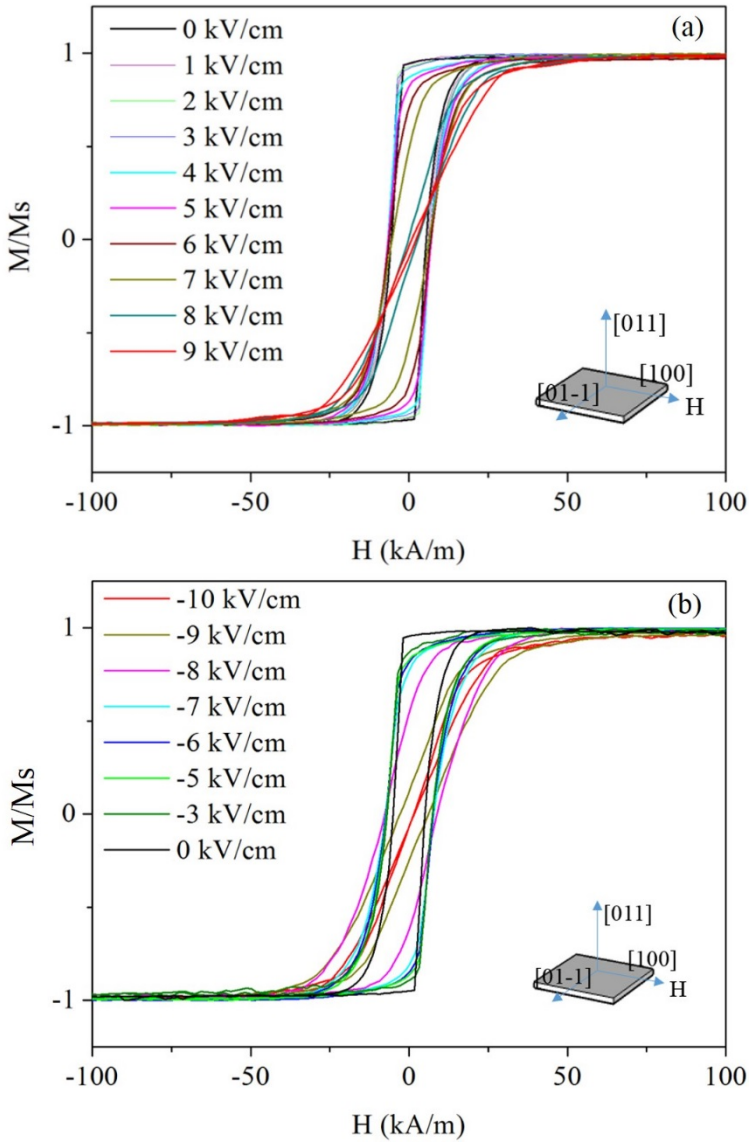

Fig. 5.6 Electric dependence of magnetic hysteresis loops measured along [100] in 65 nm CoFe /(011)PMN-PT heterostructure when the positive (a) and negative (b) E-fields were applied.

The E-field controlled magnetic properties were first investigated on the 65 nm CoFe/(011) PMN-PT heterostructure. The E-field was applied from -10 kV/cm to 9

kV/cm on this heterostructure, for each E-field a MOKE loop was taken, as shown in **Fig. 5.6**. **Fig. 5.6** shows the detailed electrical dependence on the magnetic hysteresis loops along [100] direction in 65 nm CoFe/(011) PMN-PT heterostructure. Both positive (**Fig. 5.6** (a)) and negative (**Fig. 5.6** (b)) E-fields were applied through the substrate thickness and induced a large magnetization change. It can be observed that the squareness decreased dramatically and conversely the saturation field (H_s) increased gradually with the increasing magnitude of the E-field. The changes in the magnetic properties and magnetic anisotropy induced by the positive and negative E-fields were similar, which indicates an almost symmetric piezoelectric strain variation against the E-field.

Fig. 5.7 shows the detailed variation in the M_r/M_s, H_s and H_c taken from the magnetic hysteresis loops (**Fig. 5.6**) at each applied E-field in the 65 nm CoFe/PMN-PT heterostructure. With increasing the E-field strength from 0 kV/cm to 9 kV/cm, the M_r/M_s decreases from 95.5% to 0.5%, while the H_s increases from 25.5 kA/m to 63.7 kA/m. Here, when the H_s is taken from a hard-axis loop, the anisotropy field H_k is believed to be equal to H_s. Thus, the experimentally measured E-field induced effective anisotropy field ($\Delta H_{keff} = H_{keff}$ (E = 9 kV/cm) - H_{keff} (E = 0 kV/cm)) is 38.2 kA/m. The [100] direction is changed fully from an easy axis to a standard hard axis on the application of an E-field of 9 kV/cm.

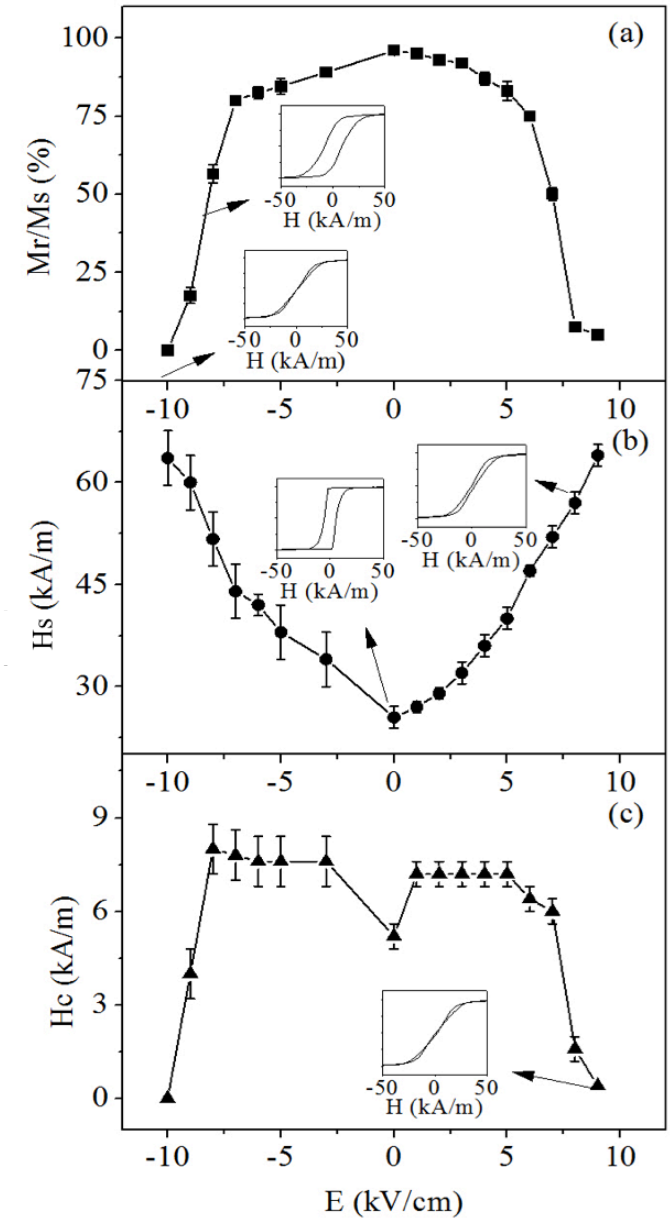

Fig. 5.7 The normalized remanent magnetization (M_r/M_s) (a), saturation field (H_s) (b) and coercive field (H_c) (c) measured along the [100] direction as a function of applied E-field in the 65 nm CoFe/PMN-PT heterostructure, respectively.

The E-field induced effective anisotropy field can also be expressed as [17]:

$$H_{keff} = \frac{3\lambda_s Y(d_{32} - d_{31})E}{M_s(1+\nu)} \tag{5.1}$$

where saturation magnetostriction λ_s of $Co_{50}Fe_{50}$ is taken to be 65 ppm [18], saturation magnetization M_s is 1900 kA/m, Young's modulus Y is 250 GPa, [15] Poisson's ratio ν is 0.26 [19] and E represents the applied E-field. When the applied E-field strength is 9 kV/cm, the calculated H_{keff} is 495 ± 15 Oe (i.e., 39.4 ± 1.2 kA/m), which is in good agreement with the experimental result. Compressive strain is created along [100] because of the negative piezoelectric coefficient (d_{31} = -1500 ~ -2000 pC/N), which causes the increase in H_k due to the positive magnetostriction constant of CoFe. The increased H_k forces the in-plane magnetization to rotate from the direction of [100] to [01-1] and thus leads to the reduction of M_r/M_s along [100]. Interestingly, the H_k is changed almost linearly with E-field, while the M_r/M_s and H_c are changed significantly from 6 kV/cm to 8 kV/cm, which is attributed to a high transverse strain from orthorhombic to rhombohedral (R) phase transition induced by E-field [20].

For the thinner film sample (45 nm), the magnetic property variation with the E-field shows a different trend. **Fig. 5.8** shows the detailed variation in the M_r/M_s, H_s and H_c taken from the magnetic hysteresis loops (**Fig. 5.9** (b)) at each applied E-field ranging from 0 to 7 kV/cm in the 45 nm CoFe/PMN-PT heterostructure. The M_r/M_s and H_s show an almost opposite variation trend. The former firstly decreases linearly from 75 ± 2.5 % to 45 ± 2.5 % and then keeps constant around 50 ± 2.5 %, while the later almost increases linearly from 25 ± 2 kA/m to 53 ± 2 kA/m and then keeps constant around 55 ± 2 kA/m. In contrast, the H_c increases continuously 3.5 ± 0.25 kA/m to 21 ±0.25 kA/m. The changes of M_r/M_s and H_s can be explained by a correlation between the stress and magnetic anisotropy [21], as discussed above in the 65 nm

CoFe/PMN-PT heterostructure. Here, the increased Hc is attributed to an irreversible rotation or domain wall displacement [22] induced by the compressive strain along [100].

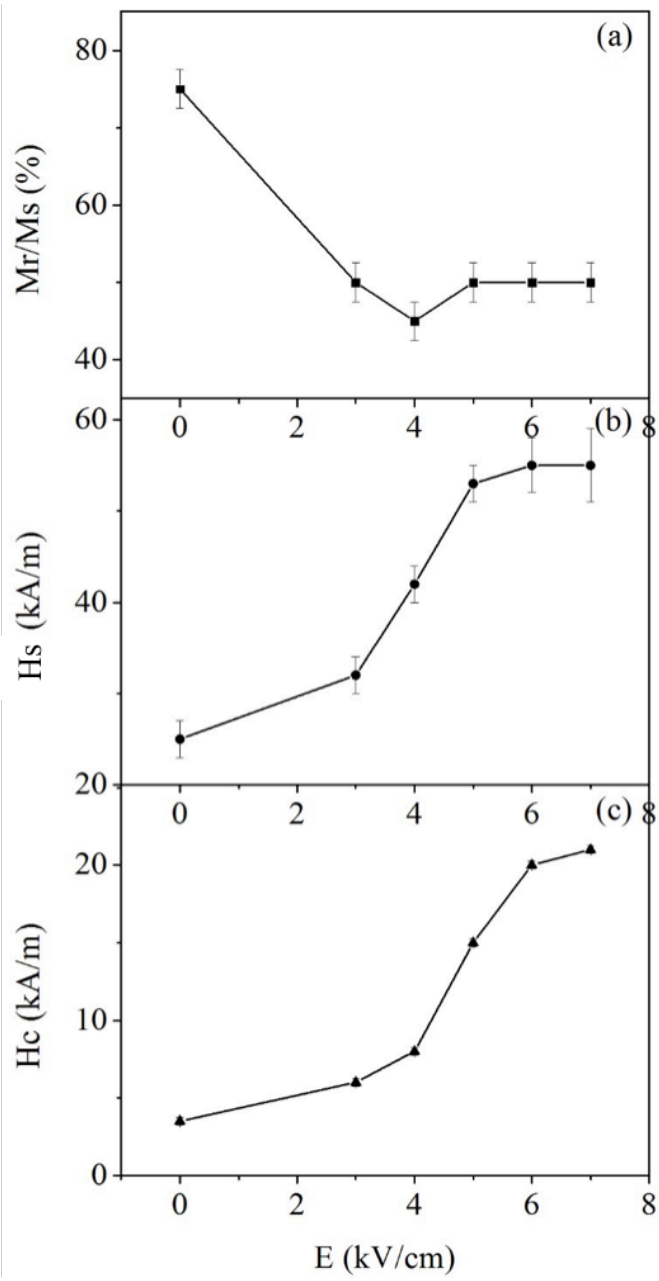

Fig. 5.8 The M_r/M_s (a), H_s (b) and H_c (c) measured along the [100] direction as a function of applied E-field in the 45 nm CoFe/PMN-PT heterostructure, respectively.

For such strong strain-mediated magnetization, the origin from the large magnetostriction effect is widely reported now for thick monolayer metal film on a FE substrate (PMN-PT). However, there may be another potential contribution from the strain effect on interfacial coupling [16] in the system based on orbital hybridization. In the CoFe/PMN-PT heterostructure, a large lattice mismatch (~ 28.9 %) exists due to the distinct in-plane lattice parameters of a_{CoFe} = 2.858 Å [15] and a_{PMN-PT} = 4.021 Å [16]. The polycrystalline CoFe films grown on PMN-PT are likely to be under weak tensile strain. When the compressive strain induced by the E-field is applied it will partly release the tensile strain, which may result in stronger orbital hybridization between the atoms and thus stronger interfacial coupling [16]. For example, the *d* orbital hybridization between Ti and Fe reported in Fe/$BaTiO_3$ system [23] was enhanced when the E-field was applied. This was due to the displacements of atoms at the interface created by FE instability, which changed the overlap between atomic orbitals at the interface and thus changed the interfacial magnetization [23]. However, in most cases, the strain effects on interfacial coupling mechanism is used to explain epitaxial ultrathin magnetic film system (< 5 nm) because the interfacial contribution to the magnetization is known to be very weak in bulk like films. More work on strain effect on interfacial coupling mechanism in polycrystalline thick films system remains to be done.

5.5 Thickness dependence of magnetoelectric coupling

In this section the thickness dependence is investigated for an optimization of ME coupling strength.

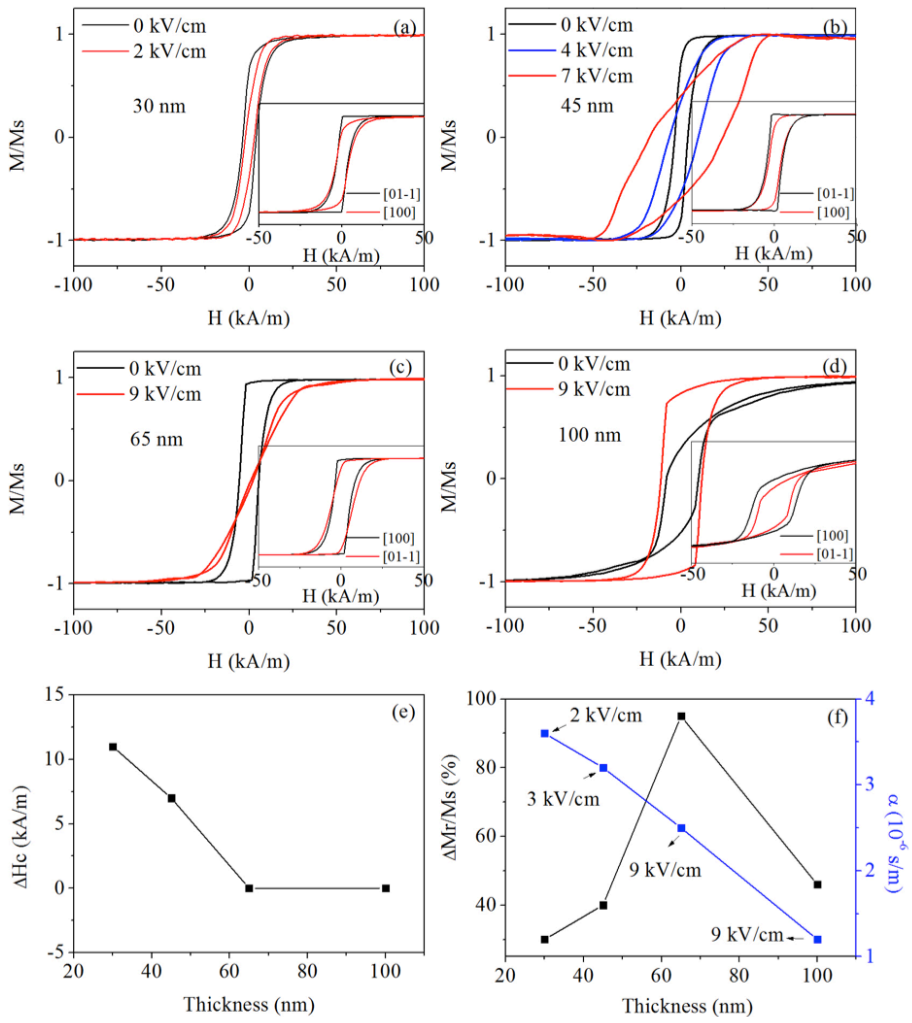

Fig. 5.9 (a)-(d) Electric dependence of magnetic hysteresis loops in CoFe/(011)PMN-PT heterostructure with thickness of CoFe layer. The insets show easy and hard axis loops of as-grown samples without the E-field. (e) Absolute values of coercive field (H_c) changes with CoFe thickness when the E-field of 3 kV/cm was applied. (f) Absolute maximum values of remanence ratios (M_r/M_s) and ME constant (α) change with CoFe thickness.

Fig. 5.9 (a)-(d) show the electrical dependence on the magnetic hysteresis loops of CoFe/(011) PMN-PT heterostructures for the series of CoFe thicknesses. In **Fig. 5.9** (a)-(c), the hysteresis loops were measured along [100] direction of PMN-PT, while in **Fig. 5.9** (d), the hysteresis loops were measured along [01-1] due to stronger

coupling along this direction than [100]. For the 100 nm thick CoFe film, it is observed that the H_k is increased greatly compared with the other films. Therefore, it may be easier to reduce the H_k by the tensile strain along [01-1] than to increase the H_k further by the compressive strain along [100], which may explain why the stronger ME coupling is along [01-1] for the 100 nm thick sample. The insets show the similar in-plane magnetic anisotropy for all the samples' thicknesses.

The initial in-plane magnetic anisotropy was induced by the in-situ H-field applied during growth. When the E-field-induced strains were applied on the magnetic film, strain-induced anisotropy change can be described as [5]:

$$\Delta K = -\frac{3\lambda\varepsilon Y}{2(1-v)} \tag{5.2}$$

Where *v* and Y are the Poisson's ratio and Young's modulus of the FM film. The λ is magnetostriction constant about 40 ± 5 ppm, as shown in **Fig. 5.10**. The compressive strain ε created along [100] is cited from [24], about - 2000 ppm. Therefore, the E-field induced anisotropy energy is positive along the [100]. In other words, anisotropy energy increases during applying the E-field, which consequently hinders magnetization alignment along [100] direction, i.e. magnetic hard axis. To the contrary, the tensile strain ε created along [01-1] induces negative anisotropy energy, which favours magnetization alignment along [01-1] direction, i.e. magnetic easy axis. The change of magnetic remanence ratio (M_r/M_s) induced by the E-field of 9 kV/cm is greatly enhanced from 46% to 95% by reducing the thickness of CoFe layer from 100 nm to 65 nm, as shown in **Fig. 5.9** (f). However, when CoFe layer thickness is further reduced to 45 nm and 30nm, the maximum changes of M_r/M_s are induced at the E-fields of 3 kV/cm and 2 kV/cm, respectively.

For both thinner CoFe layers, when the E-field increases further, the H_c are increased

significantly, but M_r/M_s stays almost constant. As shown in **Fig. 5.9** (e), the change of H_c (ΔH_c) is up to11 kA/m (138 Oe) at the E-field of 3 kV/cm for 30 nm thickness. Also, the H_c continues to increases as the E-field increases further.

A maximum ΔH_c achieves 17.5 kA/m (220 Oe) at the E-field of 7 kV/cm in the 45 nm thick sample, which is five times larger than the H_c of 3.5 kA/m (44 Oe) without E-field. The value of ΔH_c is also much larger than 3.5 Oe and 22.93 Oe reported previously in CoFe/PZT system [25] and CoFeB/SiO_2/PMN-PT system [26], respectively. The reason is attributed to the larger piezoelectric response of PMN-PT than that of PZT and the direct deposition of CoFe on the PMN-PT substrate rather than on a buffer layer of SiO_2.

The ME coupling constant α can be defined as $\alpha = \mu_o \Delta M_r/E$ where μ_o is the permeability of free space [27]. The value of ΔM_r is estimated from the experimental result of E-field induced M_r/M_s change ($\Delta M_r/M_s$) and saturated magnetization M_s (~ 1900 emu/cm^3) taken from the reference [3,19]. For example, for CoFe layer thickness of 65 nm, ME coupling constant $\alpha = \mu_o \Delta M_r/E = 4\pi \times 10^{-7} \times$ (1900 emu/cm^3) $\times$ 0.95 / (9 kV/cm) = 2.5 $\times$ 10^{-6} s/m. To understand the effect of magnetic layer thickness on α, it is described as[5]:

$$\alpha = \frac{\mu_o \Delta M_r}{E} = \frac{\varepsilon_{FM}}{\varepsilon_{FE}} \times \frac{\mu o \Delta M_r}{\varepsilon_{FM}} \times \frac{\varepsilon_{FE}}{E} = n \times \frac{\varepsilon_{FM}}{\varepsilon_{FE}} \times \lambda \times d_{ij} \qquad (5.3)$$

where ε_{FM} and ε_{FE} represent strains of the FM and FE layers, respectively. The d_{ij} is the in-plane piezoelectric constant of the FE layer and n is a constant.

The experimental magnetostriction constant λ measured based on the villari effect (see section 4.3.1 in details) remains almost constant at about 40 ± 5 ppm for these bulk like films (> 20 nm), such that λ of 29 ± 7 ppm, 35 ± 3 ppm and 40 ± 3 ppm for

the thickness 30 nm, 35 nm and 65 nm respectively (**Fig. 5.10**), which is almost consistent with λ of 47 ± 4 ppm reported for 50 nm CoFe film [2]. The trends show the value of λ gradually gets close to that of bulk as shown in the formula $\lambda = \lambda_b + \lambda_i/t$ above due to the reduction in the interfacial contribution with the increasing film thickness [28]. The last term of equation (4.3) d_{ij} is also constant due to the same PMN-PT substrates used. Therefore, α is eventually determined by the term of $\varepsilon_{FM}/\varepsilon_{FE}$ which increases with FM layer thickness decreasing due to the reduced relaxation of ε_{FM} in the thin FM layer. In **Fig. 5.9** (f), α increases from 1.2×10^{-6} s/m to 2.5×10^{-6} s/m at 9 kV/cm when CoFe thickness reduces from 100 nm to 65 nm, which is consistent with the equation 4.3. When the CoFe thickness continues to reduce to 45 nm and 30 nm, α increases only at a lower E-field strength of 3 kV/cm and 2 kV/cm, respectively. The reason for this is that the giant ε_{FM} in the thinner CoFe layers created by the FE layer results in domain wall pinning [29], which causes the significant increase on the H_c.

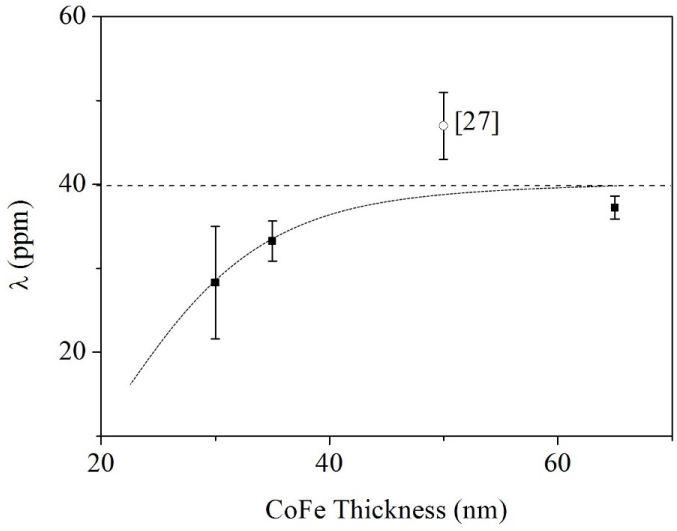

Fig. 5.10 The CoFe film thickness dependence of the effective saturated magnetostriction constant λ_{eff}.

In this study, α is two orders larger than that of 6×10^{-8} s/m in the epitaxial $La_{0.67}Sr_{0.33}$ MO_3/(001) PMN-PT system [30]. Although, recently some large ME coupling constants α of 8×10^{-7} s/m and 4.55×10^{-7} s/m were reported in a CoPd/PMN-PT system [5] and Fe-Ga/PMN-PT system [14], respectively. The giant coupling constant is attributed to the combination of a few crucial properties: a thin film thickness (≤ 100 nm), large magnetostriction constant, saturation magnetization and M_r/M_s in the sputtered $Co_{50}Fe_{50}$ film and the high in-plane piezoelectric coefficient PMN-PT substrate with smooth surface, which provides an effective elastic coupling at the interface between the CoFe film and the PMN-PT substrate.

5.6 Summary

Cross-sectional high-resolution transmission electron microscopy (HRTEM) image showed a uniform columnar growth structure of the 65 nm CoFe film and an average columnar grain size of 3.3 ± 0.5 nm. Selected area electron diffraction (SAED) pattern showed the CoFe polycrystalline structure, with columnar grains composed of randomly oriented nanocrystals. Giant magnetoelectric (ME) coupling was observed in the heterostructure. A large remanence ratio (M_r/M_s) tunability of 95% has been demonstrated, corresponding to a giant ME constant (α) of 2.5×10^{-6} s/m, when an external electric field (E-field) of 9 kV/cm was applied. A large E-field induced effective magnetic anisotropy field (H_{eff}) of 38.2 kA/m was also observed. The reason can be attributed to a combination of several main factors. Firstly, large transverse anisotropic strains produced in (011) PMN-PT by the E-field, which significantly contributes to the change of in-plane magnetic anisotropy of magnetic layer. Secondly, a weak magnetic anisotropy was obtained in the CoFe film and thus a low magnetic anisotropy energy was needed to be overcome by the elastic stress.

Finally, the relatively thin film thickness (< 100 nm) reduces a strain relaxation existing in the heterostructure. Such MF heterostructure provides considerable opportunities for E-field controlled multifunctional devices.

5.7 References

[1] R.C. Hall, J. Appl. Phys. 31 (1960) S157–S158.

[2] H.S. Jung, W.D. Doyle, J.E. Wittig, J.F. Al-Sharab, J. Bentley, Appl. Phys. Lett. 81 (2002) 2415–2417.

[3] S. Rengarajan, E.J. Yun, W.S. Kang, R.M. Walser, J. Appl. Phys. 81 (1997) 4761–4763.

[4] S.H. Baek, J. Park, D.M. Kim, V. a. Aksyuk, R.R. Das, S.D. Bu, D. a. Felker, J. Lettieri, V. Vaithyanathan, S.S.N. Bharadwaja, N. Bassiri-Gharb, Y.B. Chen, H.P. Sun, C.M. Folkman, H.W. Jang, D.J. Kreft, S.K. Streiffer, R. Ramesh, X.Q. Pan, S. Trolier-McKinstry, D.G. Schlom, M.S. Rzchowski, R.H. Blick, C.B. Eom, Science 334 (2011) 958–961.

[5] J.H. Kim, K.S. Ryu, J.W. Jeong, S.C. Shin, Appl. Phys. Lett. 97 (2010) 252508.

[6] A. Javed, N.A. Morley, M.R.J. Gibbs, J. Magn. Magn. Mater. 321 (2009) 2877–2882.

[7] N.A. Morley, A. Javed, M.R.J. Gibbs, J. Appl. Phys. 105 (2009) 07A912.

[8] K. Srinivas, M. Manivel Raja, D.V. Sridhara Rao, S.V. Kamat, Thin Solid Films 558 (2014) 349–355.

[9] B. Wang, W. Huang, S. Cao, Y. Du, Y. He, B. Huang, Rare Met. 29 (2010)

583–588.

[10] M. Grigoras, N. Lupu, H. Chiriac, IEEE Trans. Magn. 47 (2011) 3886–3888.

[11] Q. Luo, L. Liu, G. Xiao, Y. Li, J. Supercond. Nov. Magn. 27 (2014) 1419–1424.

[12] G.S. Bales, A. Zangwill, J. Vac. Sci. Technol. A 9 (1991) 145–149.

[13] J.A. Thornton, Annu. Rev. Mater. Res. 7 (1977) 239–260.

[14] Y. Zhang, Z. Wang, Y. Wang, C. Luo, J. Li, D. Viehland, J. Appl. Phys. 115 (2014) 084101.

[15] V.A. Vas'ko, J.O. Rantschler, M.T. Kief, IEEE Trans. Magn. 40 (2004) 2335–2337.

[16] S. Das, A. Herklotz, E. Pippel, E.J. Guo, D. Rata, K. Dörr, Phys. Rev. B 91 (2015) 134405.

[17] M. Liu, O. Obi, J. Lou, Y.J. Chen, Z.H. Cai, S. Stoute, M. Espanol, M. Lew, X. Situ, K.S. Ziemer, V.G. Harris, N.X. Sun, Adv. Funct. Mater. 19 (2009) 1826–1831.

[18] B.M. Bozorth, Ferromagnetism, IEEE, New York, 1997.

[19] T.L. Jin, L. Hao, J.W. Cao, M.F. Liu, H.G. Dang, Y. Wang, D.P. Wu, J.M. Bai, F.L. Wei, Appl. Phys. Express 7 (2014) 043002.

[20] L.H. Luo, H.X. Wang, Y.X. Tang, X.Y. Zhao, Z.Y. Feng, D. Lin, H.S. Luo, J. Appl. Phys. 99 (2006) 024104.

[21] D. Sander, Reports Prog. Phys. 62 (1999) 809–858.

[22] Y. Chen, T. Fitchorov, Z. Cai, K.S. Ziemer, C. Vittoria, V.G. Harris, J. Phys. D. Appl. Phys. 43 (2010) 155001.

[23] C.G. Duan, S.S. Jaswal, E.Y. Tsymbal, Phys. Rev. Lett. 97 (2006) 047201.

[24] T. Fitchorov, Y. Chen, B. Hu, S.M. Gillette, A. Geiler, C. Vittoria, V.G. Harris, J. Appl. Phys. 110 (2011) 123916.

[25] N. Moutis, D. Suarez-Sandoval, D. Niarchos, J. Magn. Magn. Mater. 320 (2008) 1050–1055.

[26] G.D. Zhu, K.L. Wong, J. Zhao, P.K. Amiri, K.L. Wang, J. Hockel, G.P. Carman, J. Zhu, I. Krivorotov, J. Appl. Phys. 112 (2012) 033916.

[27] W. Eerenstein, M. Wiora, J.L. Prieto, J.F. Scott, N.D. Mathur, Nat. Mater. 6 (2007) 348–351.

[28] H. Fukuzawa, Y. Kamiguchi, K. Koi, H. Iwasaki, M. Sahashi, J. Appl. Phys. 91 (2002) 3120–3124.

[29] C.C.H. Lo, S.J. Lee, L. Li, L.C. Kerdus, D.C. Jiles, IEEE Trans. Magn. 38 (2002) 2418–2420.

[30] C. Thiele, K. Dörr, O. Bilani, J. Rödel, L. Schultz, Phys. Rev. B 75 (2007) 054408.

Chapter 6

6 Electric field-controlled magnetization in bilayered magnetic films

In Chapter 5, large volatile magnetization changes were demonstrated in single layer $Co_{50}Fe_{50}$ films with different thicknesses. In this chapter, E-field-controlled non-volatile magnetization changes in bilayered ferromagnetic films were studied for the application in magnetoelectric random access memory (MERAM). Bilayered magnetic films $Co_{50}Fe_{50}$/Metglas ($Fe_{81}B_{13.5}Si_{3.5}C_2$) were RF sputtered on both (001)-oriented and (011)-oriented PMN-PT (lead magnesium niobate-lead titanate) substrates. The bilayered films show excellent soft magnetic properties with high magnetostriction due to the Metglas layer having an extremely low coercive field (H_c ≈ 1.13 Oe [1] or 0.09 kA/m) and relatively high magnetostriction constant ($\lambda \approx 35$ ppm [1]). The H_c of 65 nm CoFe film on (001) Si substrate is reduced from ~ 1 kA/m to ~ 0.24 kA/m when a 24 nm thick Metglas layer is introduced (**Fig. 6.1**). Meanwhile, the λ is also improved from 35 ± 5 ppm to 60 ± 10 ppm (**Fig. 6.7** (c)). Such bilayered films with low H_c and high λ provide great opportunities to control magnetization direction with low power in magnetoelectric heterostructures. In addition, a large lattice mismatch (~ 28.9%) between the CoFe (a_{CoFe} = 2.858 Å [2]) and the PMN-PT (a_{PMN-PT} = 4.021 Å [3]) may induce a weak tensile strain in the film layer, hence the introduction of the amorphous Metglas layer should eliminate this potential strain.

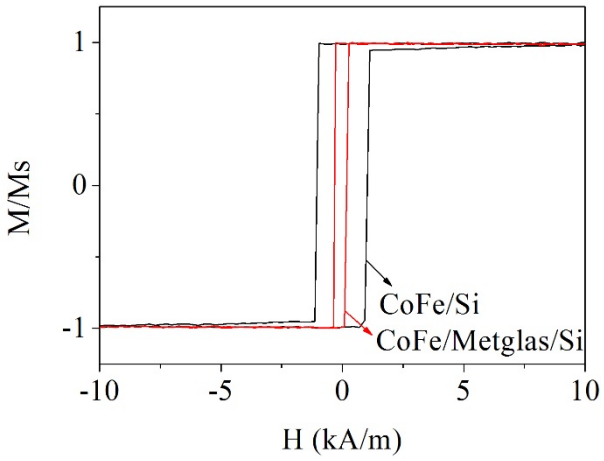

Fig. 6.1 The magnetic hysteresis loops measured along the easy axis of 65 nm CoFe on Si and 65 nm CoFe on 24 nm Metglas/Si by MOKE at room temperature.

Electric field-controlled magnetization changes were observed in all these samples: 65 nm CoFe/24 nm Metglas/(001) PMN-PT, 65 nm CoFe/24 nm Metglas/(011) PMN-PT and 30 nm CoFe/12 nm Metglas/(011) PMN-PT. The maximum magnetic remanance ratio change ($\Delta M_r/M_s$) was 46% for 65 nm CoFe/24 nm Metglas/(001) PMN-PT. In this heterostructure, the electric-field created two new non-volatile remanance states and the as-grown remanance state was altered permanently. In the 30 nm CoFe/12 nm Metglas/(011) PMN-PT sample, a large $\Delta M_r/M_s$ of 80% along the [100] direction was measured, while the $\Delta M_r/M_s$ along the [01-1] direction was 60% at the applied electric field of 5 kV/cm, corresponding to a giant ME coupling constant $\alpha = \mu_o \Delta M_r/E = 2.9 \times 10^{-6}$ s/m.

6.1 Sample fabrication and measurements

Bilayered ferromagnetic films of CoFe/Metglas were directly deposited onto both (001) and (011)-oriented PMN-PT substrates (i.e. PMN-PT1 and PMN-PT2 (see **Table 4.1**)) without breaking the vacuum by RF sputtering in a Nordiko NM2000 RF

deposition system (see section 4.1.1). These growth parameters (the sputtering power 75W, working pressure 5.0 ± 0.1 mTorr and base pressure $1.2 \pm 0.2 \times 10^{-3}$ mTorr) were chosen based other experimental results, where the CoFe thin film sputtered at higher sputtering power (P) 150 W and 200 W and with the Metglas underlayer sputtered at only 75 W showed a larger coercive field, as shown in **Fig. 6.2**. The coercive field (H_c) was increased significantly from 0.24 kA/m to 5.89 kA/m when the P for the CoFe thin film was increased from 75 W to 200 W. Moreover, the magnetic anisotropy induced by an in-situ H-field was weakened when the higher P (200 W) was used, as shown in **Fig. 6.3**. These results are consistent with those for only CoFe films without the underlayers in **Fig. 5.3** (Chapter 5). Magneto-optical Kerr effect (MOKE) measurements were used to investigate magnetic properties when a series of dc E-fields were applied to the substrates, as shown in the schematic in **Fig. 6.4** (and described in section 4.4). The normalized remanent magnetization (M_r/M_s) and anisotropic field (H_k) were taken from the magnetic hysteresis loops. The H_k was taken at the $M/M_s = 1$. The effective saturation magnetostriction constants (λ) were measured using a technique [4] based on the Villari effect (section 4.3.1). Cross-sectional transmission electron microscopy (TEM) specimens were prepared by Focused Ion Beam (FIB) in FEI Quanta 200 3D and observed on both FEI Tecnai T20 and Jeol 2010F operating at 200 kV (section 4.2.3and 4.2.4).

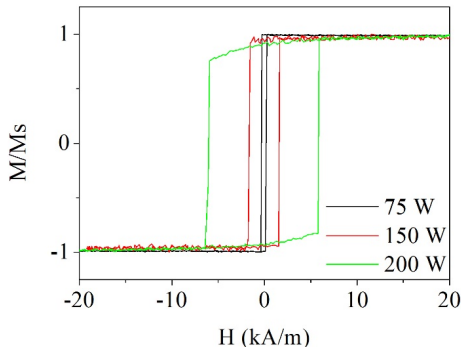

Fig. 6.2 The magnetic hysteresis loops measured along the easy axis of 65 nm CoFe sputtered at 75W, 150W and 200W respectively and with a 24 nm thick Metglas underlayer on the Si substrates.

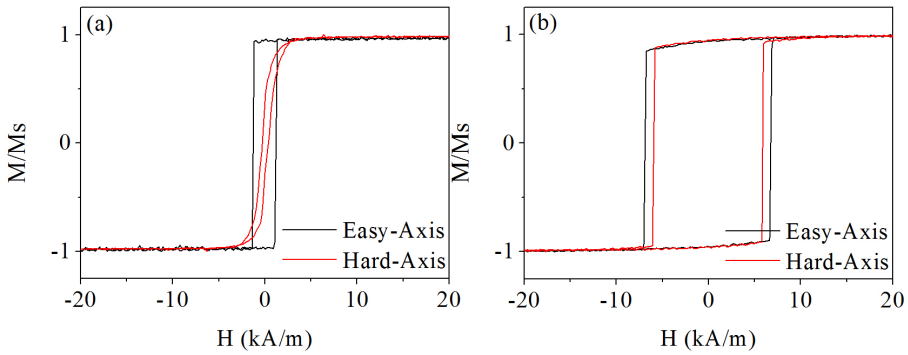

Fig. 6.3 The magnetic anisotropy of 65 nm CoFe sputtered at 75W (a) and 200W (b) with 30 nm Metglas underlayer on the Si substrates.

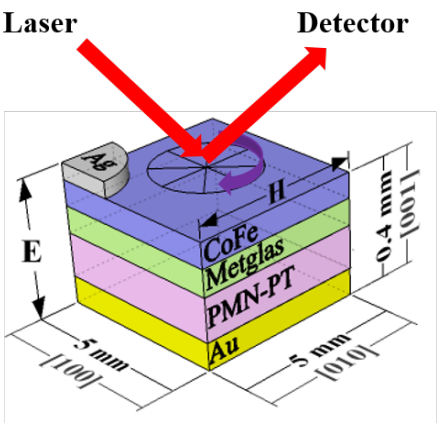

Fig. 6.4 A schematic (not to scale) of 65 nm CoFe/24 nm metglas/400 μm (001) PMN-PT heterostructure. Magnetic properties were measured by MOKE system. Magnetic field (H-field) was fixed and applied in plane, while the E was applied through the thickness. The sample was measured as a function of rotating angle.

6.2 Microstructure of bilayered films and interface

To investigate an effect of the sputtering power P on the microstructure of CoFe thin film grown on the Metglas layer, the sample with the Si substrate was first investigated. **Fig. 6.5** shows the XRD spectra of these samples using the Si substrate. In **Fig. 6.5**, all samples show a stronger (110) diffraction peak of the CoFe thin film, compared with that of the only CoFe thin film without Metglas underlayer (**Fig. 5.4**). Moreover, for the sample sputtered at 200 W, when the Metglas thickness is increased from 24 nm to 30 nm, the (110) diffraction peak becomes stronger. All these results indicate the underlayer induces the stronger (110) texture in the 65 nm CoFe film. Similarly, the increased P also favors the strengthened (110) texture. However, as shown in **Fig. 6.3**, the in-plane anisotropy for the sample sputtered at 200 W almost disappears, which suggests that the enhancement of out-of-plane

texture with the increasing power (**Fig. 6.5**) does not affect the in-plane magnetic anisotropy. The reason may be understood that domain wall pinning is dominating the magnetization process. At the P of 75 W, the (110) peak shows the weakest strength and the (200) peak can be also observed. However, the (200) peak disappears and the (110) peak becomes stronger as the P increases to 150 W and 200 W. In addition, the (110) peak shifts towards a higher 2θ degree compared to the standard diffraction pattern position (cited from PDF#04-003-5514), which suggests that a compressive strain exists in the film based on the Bragg law $2d\sin\theta = \lambda$. In addition, the minimum grain size (t) can be estimated by the Scherrer formula [5] (equation 3.1, Chapter 4): $t = 0.9\lambda/(B\cos\theta_B)$, where B is almost same for these samples, at about 0.0087 (in radians) (0.5^o) and θ_B is slightly different but around 22.5 ± 0.1 degrees. Therefore, the calculated gain size is about 17.2 ± 0.1 nm.

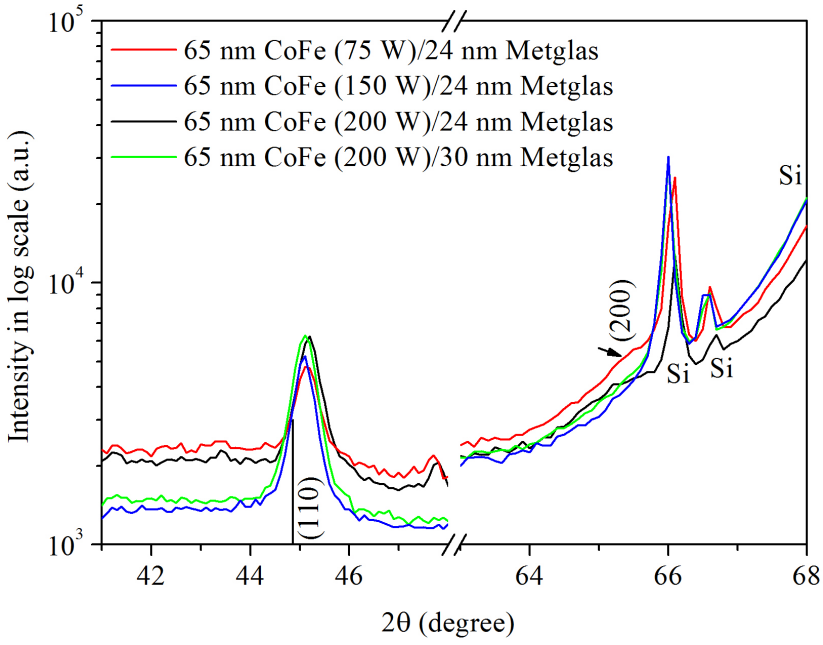

Fig. 6.5 XRD spectra of 65 nm CoFe sputtered at 75W, 150W and 200W respectively and with a 24 nm and 30 nm thick Metglas underlayer on the Si substrates.

To understand the microstructure of the magnetic films and interfaces in the heterostructures, cross-sectional TEM was undertaken. **Fig. 6.6** (a) gives a bright field TEM image of the cross-section for the 65 nm CoFe/24 nm Metglas/PMN-PT heterostructure, while **Fig. 6.6** (b) and (c) give high-resolution TEM (HRTEM) images and selected area electron diffraction (SAED) pattern (d) for the 65 nm film. **Fig. 6.6** (e)-(h) give both HRTEM and TEM images for the 65 nm CoFe/24 nm Metglas/Si heterostructure. In **Fig. 6.6**, a uniform Metglas underlayer thickness is observed. The interface between the amorphous Metglas film and the PMN-PT (**Fig. 6.6** (b)) is well-defined and smooth while that between the Metglas film and the CoFe film (**Fig. 6.6** (c)) is much rougher with about 1-2 nm roughness. The CoFe film still shows a polycrystalline structure with an out-of plane [110] texture even on the amorphous layer, as shown in **Fig. 6.6** (d). To compare, the same films were also deposited on the Si substrate and observed using TEM. As shown in **Fig. 6.6** (e) and (f), the interface between the Si substrate and the Metglas layer is not as sharp as that between the PMN-PT and the Metglas layer due to the native 1-2 nm thick oxide layer in position on the Si substrate which is also observed in **Fig. 5.5** (a) (Chapter 5). In **Fig. 6.6** (h), the amorphous morphology is seen between the Metglas layer. The non-uniform thickness of CoFe layer was produced artificially by the final milling (see section 4.2.3) during the TEM sample fabrication.

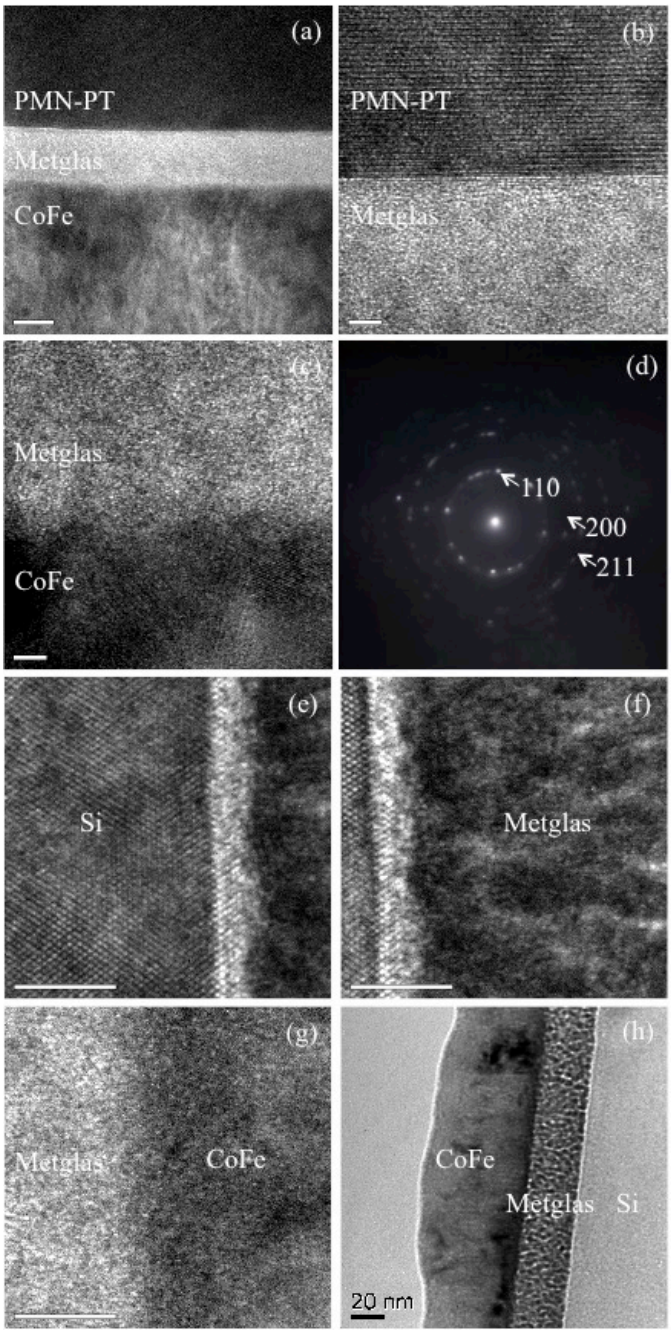

Fig. 6.6 Cross-sectional bright field TEM image (a) and HRTEM images (b) and (c) of the 65 nm CoFe/24 nm Metglas/PMN-PT heterostructure. The SAED pattern (d) of 65 nm CoFe film in the CoFe/Metglas/PMN-PT heterostructure. Cross-sectional HRTEM images (e) and (f) and bright field TEM images (g) and (h) of the 65 nm CoFe/24 nm Metglas/Si heterostructure.

6.3 Non-volatile magnetization change by the electric field

In this section, three samples 65 nm CoFe/24 nm Metglas/(001) PMN-PT, 65 nm CoFe/24 nm Metglas/(011) PMN-PT and 30 nm CoFe/12 nm Metglas/(011) PMN-PT are characterised. Especially, in 65 nm CoFe/24 nm Metglas/(001) PMN-PT sample, a non-volatile magnetization change is obtained.

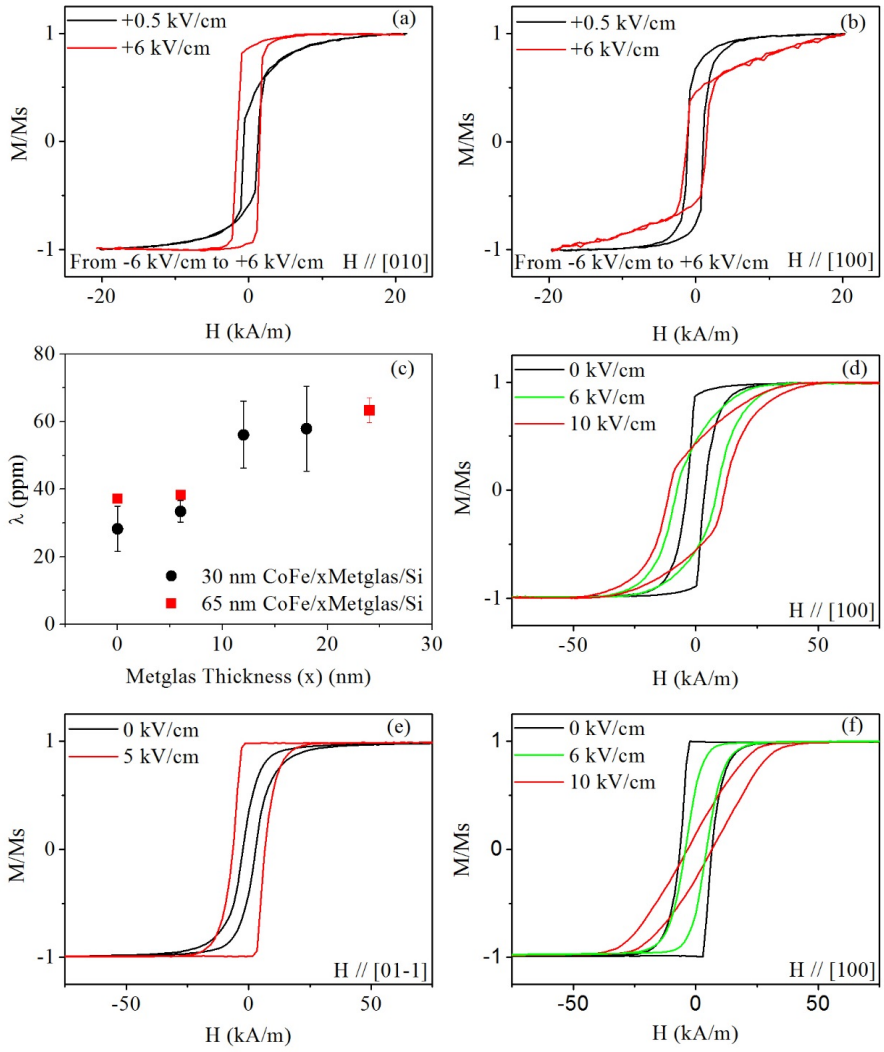

Fig. 6.7 Electric-field dependence of magnetic hysteresis loops in 65 nm CoFe/24 nm Metglas/(001) PMN-PT (a) and (b), in 65 nm CoFe/24 nm Metglas/(011) PMN-PT (d) and

in 30 nm CoFe/12 nm Metglas/(011) PMN-PT (e) and (f). The variation of effective saturation magnetostriction constants (λ) with Metglas thickness (x) (c).

Fig. 6.7 shows a strong magnetoelectric (ME) coupling in all samples of both (001)-oriented and (011)-oriented PMN-PT substrates. For the [100] crystallographic direction (**Fig. 6.7** (b), (d) & (f)), when the applied E-field increases, the M_r/M_s reduces and H_k increases. In contrast, M_r/M_s increases and H_k reduces along either direction [010] (**Fig. 6.7** (a)) or [01-1] (**Fig. 6.7** (e)) due to a compressive strain along [100] and positive magnetostriction constant (λ) for the bilayered thin films. As shown in **Fig. 6.7** (c), the λ increases from 35 ± 5 ppm to 60 ± 10 ppm when the Metglas thickness is greater than 6 nm. The reason may be attributed to a negative interface effect [6] removed by Metglas underlayer between CoFe and substrate. In addition, the λ for the bilayered magnetic films of 65 nm CoFe/24 nm Metglas and 30 nm CoFe/12 nm Metglas is similar at around 60 ppm. However, the thinner bilayered films show stronger ME coupling than the thicker bilayered films, as shown in **Fig. 6.7** (d) and (f), which is consistent with the previous investigation [7] on the effect of magnetic layer thickness on ME coupling. Reducing the magnetic layer thickness can cause a reduction in the strain relaxation and thus increase the ME coupling. In the 30 nm CoFe/12 nm Metglas/(011) PMN-PT sample, a maximum $\Delta M_r/M_s$ is 80 % measured along the [100] direction at the applied E-field of 10 kV/cm (**Fig. 6.7** (f)), while along the [01-1] direction $\Delta M_r/M_s$ is 60% at the applied E-field of only 5 kV/cm (**Fig. 6.7** (e)), corresponding to a giant ME coupling constant [8] $\alpha = \mu_o \Delta M_r/E = 2.9 \times 10^{-6}$ s/m, which is much larger than 1.6×10^{-7} s/m [9], 4.55×10^{-7} s/m [10] and 8×10^{-7} s/m [7] reported in monolayer magnetic film systems. In addition, it is noted that the H_c increases significantly by a factor of three

when the E-field of 10 kV/cm was applied to the 65 nm CoFe/24 nm Metglas/(011) PMN-PT sample (**Fig. 6.7** (d)). For (001)-oriented PMN-PT's heterostructure, more detailed magnetization change induced by the E-field is discussed as follows from **Fig. 6.8** to **Fig. 6.13**.

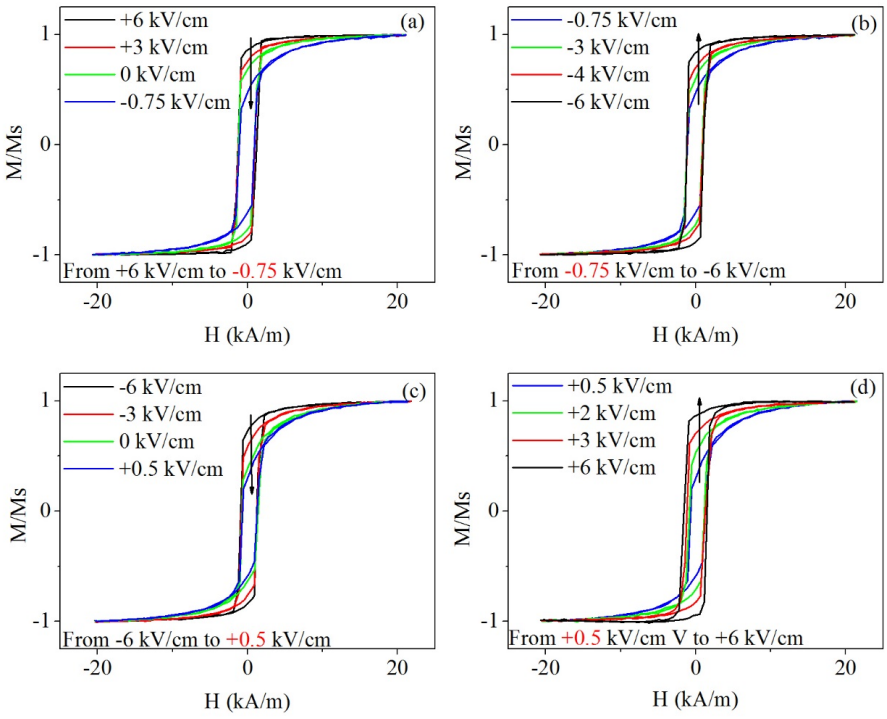

Fig. 6.8 Selection of magnetic hysteresis loops of 65 nm CoFe/24 nm Metglas/(001) PMN-PT heterostructure measured along [010] at different applied electric field.

Fig. 6.8 (a)-(d) show the normalized hysteresis loops measured along [010] with the varying E-field. All loops measured are clear and symmetric. Only some selected loops are shown in **Fig. 6.8** to avoid too much confusion. The arrows indicate the variation trend of M_r/M_s with the varying E-field magnitude and direction. The squareness of the hysteresis loops first reduces as the E-field reduces from +6 kV/cm

to -0.75 kV/cm (**Fig. 6.8** (a)) and then increases as the E-field increases from -0.75 kV/cm to -6kV/cm (**Fig. 6.8** (b)). The similar changes are also observed in **Fig. 6.8** (c) and **Fig. 6.8** (d). In addition, when the squareness reduces, the saturation field increases correspondingly, and vice versa, which suggests that the magnetization along [010] becomes alternatively easy and hard with the varying E-field.

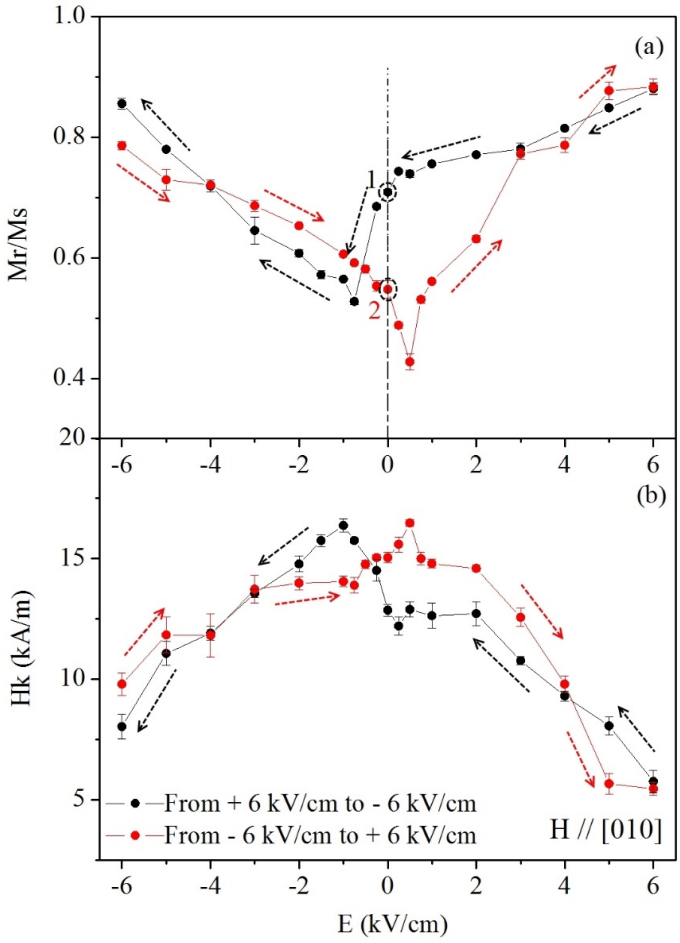

Fig. 6.9 Electrical dependence of the M_r/M_s (a) and H_k (b) along [010] with different E sweeping directions in 65 nm CoFe/24 nm Metglas/(001) PMN-PT heterostructure. The arrows indicate the E-field sweeping direction.

Fig. 6.9 (a) and (b) show the electrical dependence of the M_r/M_s and H_k along [010] direction with two opposite sweeping fields from + 6 kV/cm to – 6 kV/cm and from - 6 kV/cm to + 6 kV/cm, respectively. Both M_r/M_s and H_k are taken from the hysteresis loops (**Fig. 6.8**). The M_r/M_s is taken at H-field = 0 kA/m, while H_k is taken at M_r/M_s = 1. The arrows indicate the E-field sweeping direction. The changes in M_r/M_s and H_k show typical "butterfly" curves dependence on the E-field, which resembles curves of piezoelectric strains against the E-field change (**Fig. 6.10**), suggesting that piezoelectric strains induce the strong ME coupling through the inverse magnetostrictive effect.

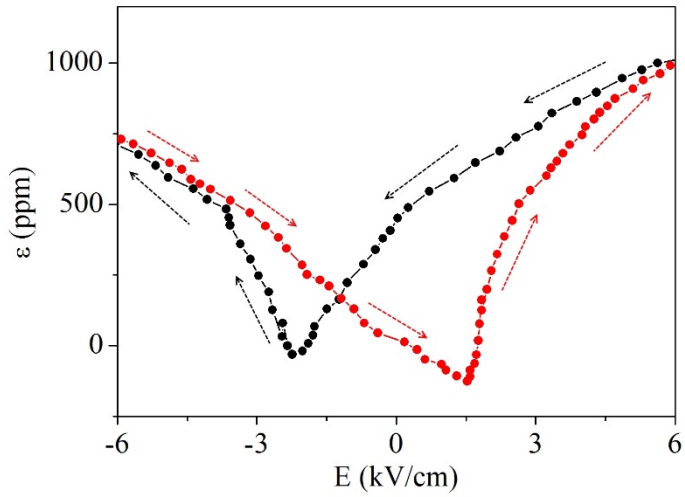

Fig. 6.10 The in-plane piezoelectric strains (ε) against the applied E-field curve cited from [13]

The sharp valleys and peaks of the curves in **Fig. 6.9** are caused by a large nonlinear strain jump below the ferroelectric coercive field ($E_c \approx 2$ kV/cm), which is attributed to the reorientation of non-180° ferroelectric polarization [11]. When the E-field

changes from +6 kV/cm to -6 kV/cm, the nonlinear strain jump happens at -0.75 kV/cm, while when the E-field changes from -6 kV/cm to +6 kV/cm, the strain jump happens at +0.5 kV/cm. Both M_r/M_s and H_k are altered at the same E-field. The comparable change ratios of M_r/M_s, H_k and H_c to the initial values are 71%, 76% and 69%, respectively. In addition, a non-volatile magnetization change of 16.1% is demonstrated, as shown in **Fig. 6.9** (a). Two distinct bistable magnetization states "1" and "2" are created by the different sweeping E-field direction and can be also controlled reversibly by the E-field. Therefore, theoretically, these can be directly read out electrically by magneto-transport measurements [12], which demonstrates the potential for the MERAM memory cell application. A short voltage impulse can change the magnetization without needing a continuous E-field and an opposite voltage signal can return the magnetization to the other state. This may be typically utilized to develop fast, low-power and high-density information storage device by E-field instead of the H-field generated by bulky and energy-consumed electromagnets.

For investigating ME coupling dependence of in-plane crystallographic orientations, the measurements of magnetic properties were also carried out along the [100] direction. **Fig. 6.11** (a) and (b) show the electrical dependence of M_r/M_s along [100] with the different E-field sweeping direction. The arrows indicate the E-field sweeping direction. The results along [010] are also plotted in **Fig. 6.11** for comparison and contrast. The opened symbols (square and circle) represent the as-grown M_r/M_s along [010] and [100], respectively. The as-grown M_r/M_s are taken from magnetic hysteresis loops measured along [100] and [010] before any applied E-field. It is seen that the results between the two directions of [100] and [010] show an opposite variation trend, which is consistent with previous reports [7,14,15]. The

positions of valleys and peaks along [100] and [010] are the same, with +0.5 kV/cm in **Fig. 6.11** (a) and -0.75 kV/cm in **Fig. 6.11** (b). The M_r/M_s along [100] and [010] for the as grown sample are 0.67 and 0.69, respectively.

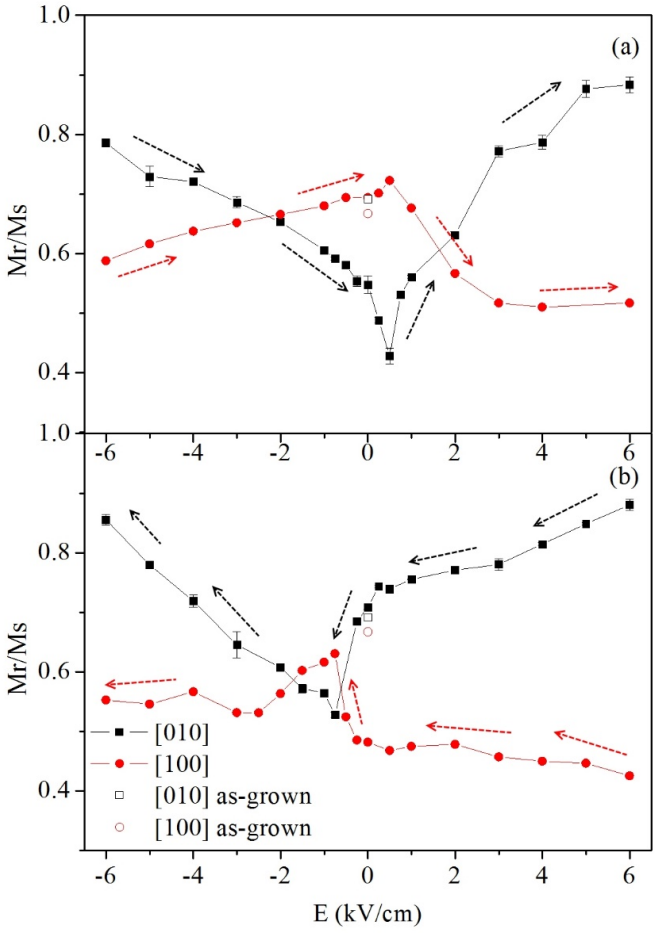

Fig. 6.11 Electrical dependence of the M_r/M_s along [100] and [010] with different E-field sweeping directions (a) from -6 kV/cm to +6 kV/cm and (b) from +6 kV/cm to -6 kV/cm in 65 nm CoFe/24 nm Metglas/(001) PMN-PT heterostructure. The arrows indicate the direction of the E-field sweeping. The M_r/M_s along [100] and [010] for the as grown sample was also plotted.

When the E-field sweeps from -6 kV/cm to 0 kV/cm, the M_r/M_s along [100] and

[010] become 0.69 and 0.55, while when the E-field sweeps from +6 kV/cm to 0 kV/cm, the M_r/M_s along [100] and [010] become 0.48 and 0.71. This suggests that the M_r/M_s does not return to the as-grown state after removing the E-field regardless of the E-field direction, but remains a permanent change in magnetization state and anisotropy. The reason is that the E-field creates two stable remaining strain states which are transferred to the bilayered magnetic films due to the elastic coupling.

6.4 Magnetic anisotropy change by the electric field

To investigate a more detailed magnetic anisotropy change in the multiferroic heterostructure, magnetization changes were measured along a series of different angular directions (0^o-360^o).

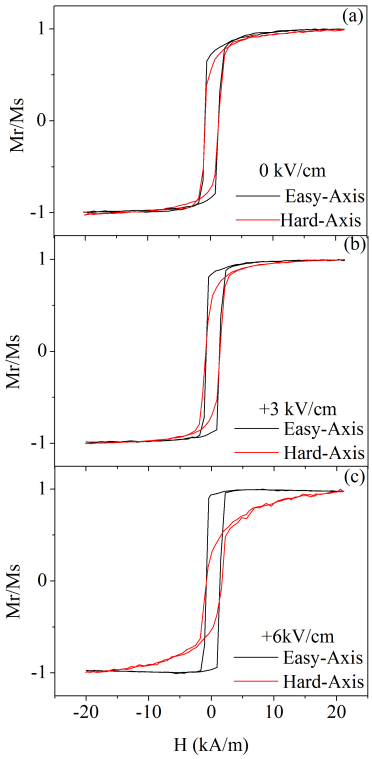

Fig. 6.12 Easy axis and hard axis magnetic hysteresis loops of CoFe/metglas/(001) PMN-PT heterostructure measured at different applied electric field.

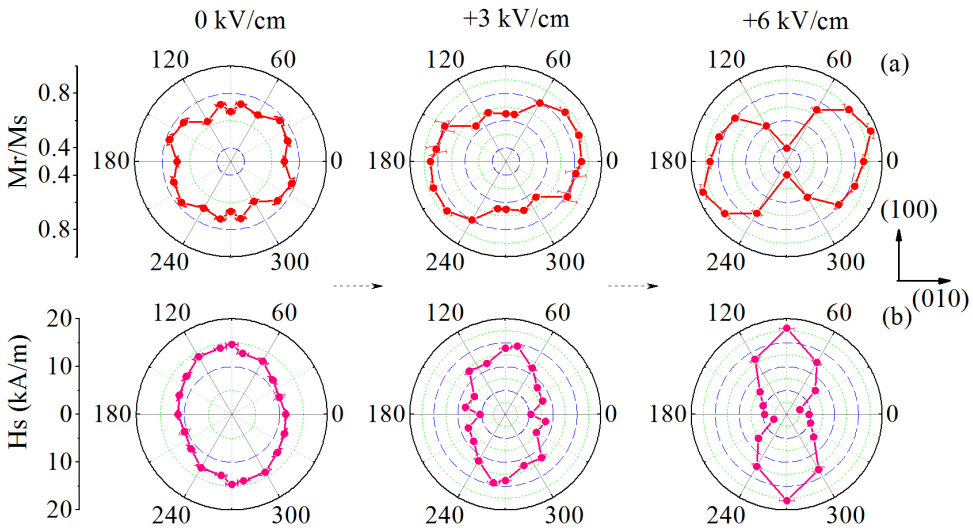

Fig. 6.13 The angular dependence of the M_r/M_s (a) and H_s (b) with the increasing applied E: 0 kV/cm, +3 kV/cm and +6 kV/cm in in 65 nm CoFe/24 nm Metglas/(001) PMN-PT heterostructure

An obvious change in the strength of anisotropy can be seen directly from some magnetic hysteresis loops selected, as shown in **Fig. 6.12**. **Fig. 6.13** shows an angular dependence of the M_r/M_s and H_k in the 65 nm CoFe/24 nm Metglas/(001) PMN-PT sample. The 0^o corresponds to the [010] direction of PMN-PT substrate. The magnetic anisotropy in both M_r/M_s and H_s is weak uniaxial almost isotropic without the applied E-field. With the increasing E-field to +3 kV/cm and +6 kV/cm, the anisotropy is steadily strengthened. At the maximum E-field of +6 kV/cm, the bilayered magnetic films show uniaxial anisotropy. The magnetization becomes easy along [010], while it becomes hard along [100] due to the E-field inducing positive effective H_k along [100] and negative effective H_k along [010].

The results are consistent with the previous reports in CoPd/(001) PMN-PT system [7] and $NiFe_2O_4$/(001) PMN-PT system [14]. Similarly, for Fe_3O_4/PZT ($d_{31} = d_{32} < 0$)

system[16], a large change M_r of 44 % was also observed when an external magnetic field was along the in-plane direction. However, the reason why the in-plane biaxial strain can induce the large in-plane anisotropy change was not explained in these reports.

Here, the magnitude of the compressive strains along [100] and [010] is thought to be different, which leads a total compressive strain along a sole direction. The reason may be attributed to some factors. For example, the crystal is not perfectly grown or cut. Therefore, the uniaxial anisotropy is induced by the biaxial compressed strains [3] with an estimated total compressive strain ($\Delta \varepsilon$= -0.07% cited from [14,15]) along [100] at applied E-field of 6 kV/cm.

6.5 Magnetoelectric memory

A hysteresis loop of the MR measured along [100] as a function of the applied E-field is demonstrated in **Fig. 6.14**. When the E-field changes from -2 kV/cm to 1.75 kV/cm or from -0.75 kV/cm to -1.75 kV/cm, the magnetization is along [100], while when the E-field changes from 6 kV/cm to -0.75 kV/cm or from 1.75 kV/cm to 6 kV/cm, the magnetization is along [010]. Based on the anisotropic magnetoresistance effect (AMR) [17], when the magnetization is parallel to a test current, a low MR is measured, while when the magnetization is perpendicular to the test current, a high MR is measured.

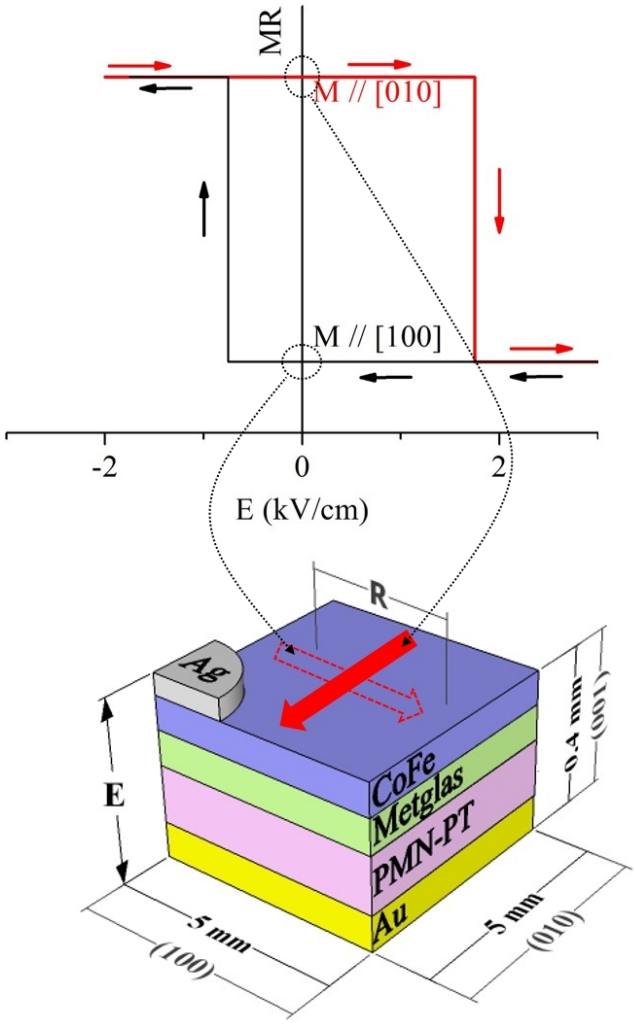

Fig. 6.14 A hysteresis loop of MR as a function of the applied E with magnetization change.

On the other hand, when a non-magnetic metal layer is introduced between the two magnetic films, with the bottom film magnetisation pinned in a fixed direction, then based on the GMR effect, the low MR is measured when magnetization in the free magnetic layer is parallel to that in the pinned magnetic layer, while the high MR is measured, when magnetization in free magnetic layer is anti-parallel to that in pinned magnetic layer. The parallel and anti-parallel magnetization between the free layer and the pinned layer is easy to achieve by choosing ferromagnetic films with obvious different λ. For example, when the pinned magnetic layer has a small λ, a

piezoelectric strain will not cause an obvious magnetization and magnetic anisotropy change in this layer. In contrast, when the same amount of strain is applied on the free layer with a much larger λ, it will cause the obvious magnetization and magnetic anisotropy change. Initially, the magnetization between two layers is assumed to be parallel. Then, when the strain is applied, the magnetization between them can be anti-parallel. In this chapter, the work is focused on E-field controlled magnetization change for bilayered magnetic films, the real either AMR or GMR change remains to be done.

6.6 Summary

In summary, HRTEM images show a sharp and smooth interface between Metglas and substrate and conversely a rougher interface was observed between Metglas and CoFe films. Strong ME coupling was observed in all these heterostructures: 65 nm CoFe/24 nm Metglas/(001) PMN-PT, 65 nm CoFe/24 nm Metglas/(011) PMN-PT and 30 nm CoFe/12 nm Metglas/(011) PMN-PT based strain mediated mechanism. The giant ME coupling constant $\alpha = 2.9 \times 10^{-6}$ s/m was demonstrated in 30 nm CoFe/12 nm Metglas/(011) PMN-PT heterostructure due to the improved λ and reduced magnetic layer thickness. The non-volatile magnetization change was shown in 65 nm CoFe/24 nm Metglas/(001) PMN-PT heterostructure. Two new created bistable magnetization states could be reversibly controlled by an E-field, while the as-grown state was permanently altered. Based on GMR or AMR, the MERAM memory cell was proposed for the fast, low-power and high-density information storage.

6.7 References

[1] Y. Chen, T. Fitchorov, Z. Cai, K.S. Ziemer, C. Vittoria, V.G. Harris, J. Phys.

D. Appl. Phys. 43 (2010) 155001.

[2] V.A. Vas'ko, J.O. Rantschler, M.T. Kief, IEEE Trans. Magn. 40 (2004) 2335–2337.

[3] S. Das, A. Herklotz, E. Pippel, E.J. Guo, D. Rata, K. Dörr, Phys. Rev. B 91 (2015) 134405.

[4] A. Javed, N.A. Morley, M.R.J. Gibbs, J. Magn. Magn. Mater. 321 (2009) 2877–2882.

[5] B. Cullity, Elements of X Ray Diffraction, Addison-Wesley Publishing Company, Inc., 1956.

[6] S. Kotapati, A. Javed, N. Reeves-Mclaren, M.R.J. Gibbs, N.A. Morley, J. Magn. Magn. Mater. 331 (2013) 67–71.

[7] J.H. Kim, K.S. Ryu, J.W. Jeong, S.C. Shin, Appl. Phys. Lett. 97 (2010) 252508.

[8] W. Eerenstein, M. Wiora, J.L. Prieto, J.F. Scott, N.D. Mathur, Nat. Mater. 6 (2007) 348–351.

[9] Y. Chen, T. Fitchorov, C. Vittoria, V.G. Harris, Appl. Phys. Lett. 97 (2010) 052502.

[10] Y. Zhang, Z. Wang, Y. Wang, C. Luo, J. Li, D. Viehland, J. Appl. Phys. 115 (2014) 084101.

[11] T. Wu, A. Bur, P. Zhao, K.P. Mohanchandra, K. Wong, K.L. Wang, C.S. Lynch, G.P. Carman, Appl. Phys. Lett. 98 (2011) 012504.

[12] S.U. Jen, J.Y. Huang, C.T. Wei, J. Magn. Magn. Mater. 174 (1997) 33–39.

[13] S.W. Yang, R.C. Peng, T. Jiang, Y.K. Liu, L. Feng, J.J. Wang, L.Q. Chen, X.G. Li, C.W. Nan, Adv. Mater. 26 (2014) 7091–7095.

[14] J.H. Park, Y.K. Jeong, S. Ryu, J.Y. Son, H.M. Jang, Appl. Phys. Lett. 96 (2010) 192504.

[15] C. Thiele, K. Dörr, O. Bilani, J. Rödel, L. Schultz, Phys. Rev. B 75 (2007) 054408.

[16] M. Liu, O. Obi, J. Lou, Y.J. Chen, Z.H. Cai, S. Stoute, M. Espanol, M. Lew, X. Situ, K.S. Ziemer, V.G. Harris, N.X. Sun, Adv. Funct. Mater. 19 (2009) 1826–1831.

[17] H. Yako, T. Kubota, K. Takanashi, IEEE Trans. Magn. 51 (2015) 403.

Chapter 7

7 Strain-mediated converse magnetoelectric coupling strength manipulation by a thin titanium layer

In this chapter, the effect of the introduction of a thin Ti buffer layer (0-10 nm) on the ME coupling strength in CoFe/PMN-PT heterostructures was investigated. The effect of the underlayer on magnetic thin films has been widely studied [1–6] in the past few decades. The thin underlayer could lead a change of the texture and the stress in the magnetic thin films. Jung et al. [3] found a thin Cu underlayer changed the preferred orientation from (200) to (110) in the CoFe films and thus improved the magnetic softness. In this chapter, a record high remanance ratio (M_r/M_s) tunability of 100% has been demonstrated in a 50 nm CoFe/8 nm Ti/PMN-PT heterostructure. Magnetic energies were calculated to explain the experimental results.

7.1 Sample fabrication and measurements

50 nm thick CoFe/x nm Ti films (x = 0, 2, 4, 6, 8, 10) were RF sputtered on the (011) oriented PMN-30%PT substrate with mean surface roughness 1.31±0.08 nm at room temperature (see section 3.1.1). The polished substrate [7] was cleaned prior to use with n-Butyl acetate, acetone and IPA. An in-situ magnetic field (H-field) of 65.3 kA/m was applied along the [100] crystallographic direction of the PMN-PT substrate during the growth of the CoFe film for obtaining a maximum normalized

remanence (M_r/M_s) ratio (~ 1) and thus maximum variation in M_r/M_s. The (011) PMN-PT (PMN-PT3, see **Table 4.1**) was used in this study due to its large anisotropic strains. The piezoelectric constant d_{33} was measured to be 400 ± 10 pC/N for all these substrates on a d_{33} testing meter in the Functional Ceramic Lab, University of Sheffield. The difference between all PMN-PT substrates used in this work was ~2.5% arising from the d_{33} measurement. The polarization (P) and out of plane piezoelectric strain (ε_z) of the (011) PMN-PT substrate as a function of the E-field was measured [1] using triangular voltage waveforms by a ferroelectric hysteresis measurement tester (National Physics Laboratories, UK) [8]. The piezoelectric strain was converted to a voltage signal by a pair of NXB2-AL nanosensors and sent to a digital voltmeter for acquiring data [9]. When the overall volume of the substrate is kept constant, the in-plane piezoelectric strain (ε_{x+y}) is $-\varepsilon_z$. Magneto-Optical Kerr Effect (MOKE) measurements (see section 4.3) were used to investigate the magnetic properties when a large range dc E-fields (0-17 kV/cm) were applied to the MF heterostructures (see section 4.4). The CoFe film and the bottom Au on the PMN-PT surface were used as the electrodes. To test the CoFe electrode, the electric capacity was measured to be about 3000 pF using an impedance analyzer, which is comparable to a sample with two Au electrodes. The effective saturation magnetostriction constants (λ_{eff}) (see section 4.3.1) were measured using a technique [7,10] based on the Villari effect. To investigate the microstructure of the heterostructure, X-ray diffraction (XRD) measurements (see 4.2.2) were made on the samples using a Siemens D5000 X-ray diffractometer with CuK_α radiation. Cross-

[1] This measurement was carried out by Dr. Tian Ye in School of Engineering and Materials Science, Queen Mary University of London.

sectional transmission electron microscopy (TEM) (see section 4.2.4) specimens were prepared by Focused Ion Beam (FIB) in FEI Quanta 200 3D (see section 4.2.3). The fabricated TEM specimens were observed on a JEOL R005 operating at 300 kV.

7.2 Microstructure of the heterostructures

Fig. 7.1 (a) shows the XRD patterns of the 50 nm CoFe/x nm Ti/PMN-PT heterostructures at a scan speed of 0.23 degree/min and the 65 nm CoFe/PMN-PT heterostructures at a scan speed of 0.5 degree/min. It shows strong (011) and (022) diffraction peaks for the PMN-PT substrate. The vertical lines indicate the 2θ position of the standard diffraction peaks (110) and (002) (cited from PDF#04-003-5514) for the CoFe film. The weak (110) diffraction peak of CoFe film at $2\theta = 44.9^{o}$ is only seen on a smaller intensity scale (**Fig. 7.1** (c)), while the (002) diffraction peak at $2\theta = 65.3^{o}$ overlaps with the strong PMN-PT (022) peak at $2\theta = 65.5^{o}$ and thus it is hard to observed, as shown in **Fig. 7.1** (b). The (110) peak of CoFe is clearly observed for 50 nm CoFe without Ti, however, the peak disappears when the Ti layer was added, with all data being taken at the same scan conditions. This suggests that the Ti layer promotes random orientation of the CoFe grains, which is helpful to reduce the magnetocrystalline anisotropy energy contribution to total magnetic energy and thus makes the magnetoelastic energy dominant.

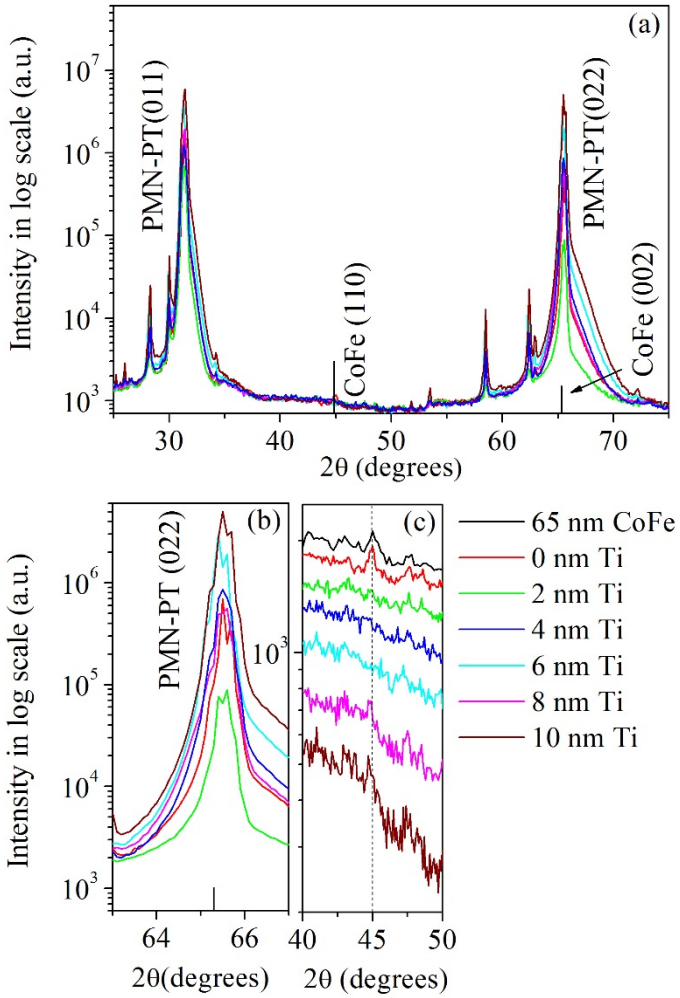

Fig. 7.1 (a) XRD spectra of 50 nm CoFe/x nm Ti/PMN-PT and 65 nm CoFe/PMN-PT heterostructures. (b) and (c) show the enlarged parts around the (002) and (110) diffraction peaks of the CoFe film, respectively.

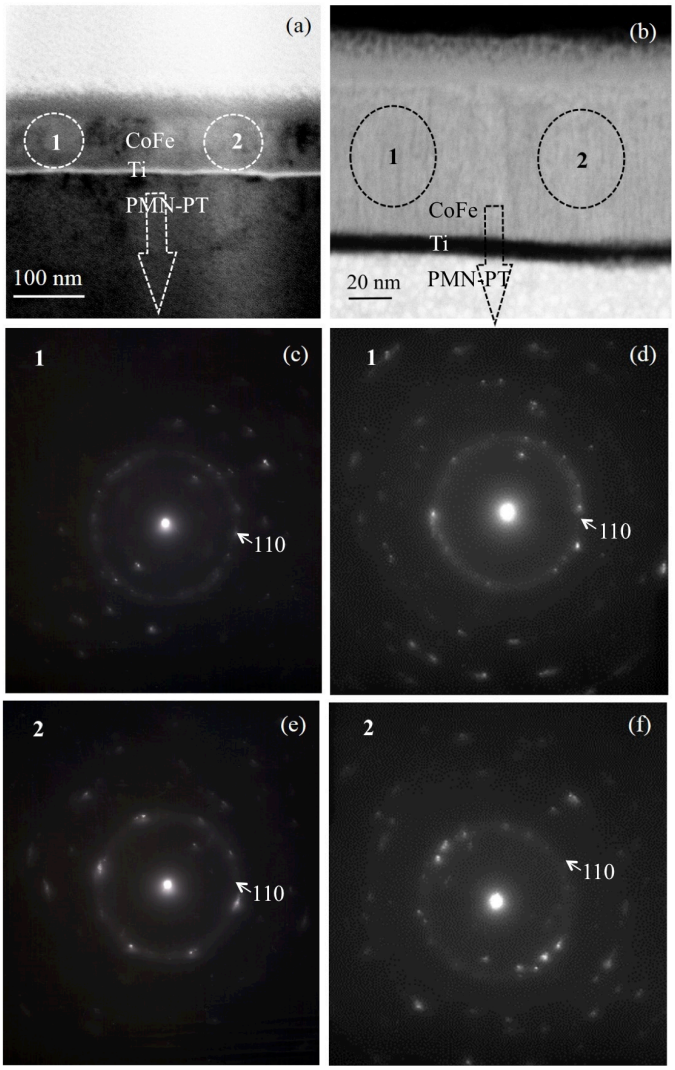

Fig. 7.2 [2] (a), (c) and (e) The BF STEM image and SAED pattern of CoFe/2 nm Ti/PMN-PT heterostructure. (b), (d) and (f) The HAADF image and SAED pattern of the CoFe/8 nm Ti/PMN-PT heterostructure. "1" and "2" refer to the different selected diffraction areas.

In **Fig. 7.2** (a), the bright field (BF) scanning TEM (STEM) image shows a uniform thickness for both CoFe and Ti layers. In **Fig. 7.2** (b), the High Angle Annular Dark Field (HAADF) image shows columnar growth structure of CoFe film, with an

[2] This work was carried out with help from Dr. Joanne Sharp on a JEOL R005.

average columnar grain size of 3.6 ± 0.5 nm in the CoFe/8 nm Ti/PMN-PT heterostructure, which is almost same as that of 3.3 ± 0.5 nm in the CoFe/ PMN-PT heterostructure[7].

Selected area electron diffraction (SAED) pattern (**Fig. 7.2** (c)-(f)) show the polycrystalline structure of CoFe film. The areas "1" and "2" show almost the same diffraction pattern for both heterostructures, which suggests the films were grown uniformly as expected. However, the crystalline plane of (110) in CoFe film for the CoFe/2 nm Ti/PMN-PT and the CoFe/8 nm Ti/PMN-PT heterostructures shows weaker diffraction than that for the CoFe/ PMN-PT heterostructure [7], which is consistent with XRD results of CoFe film. It is also observed that there are some spots on the diffraction ring, which suggests that the columnar grains are composed of randomly oriented nanocrystals.

7.3 Piezoelectric strain and ferroelectric measurement

Fig. 7.3 shows the P and ε of (011) PMN-PT substrate as a function of the E-field. The ferroelectric and piezoelectric properties were studied at an alternating E-field with a maximum amplitude of 16 kV/cm and a frequency of 0.5 Hz. The ε-E loop was measured with applying three different E-field ranges, as shown in **Fig. 7.3** (a). The range "1" and "3" includes both the positive and negative E-field directions, hence the ε-E loop is called a bipolar loop, while the range "2" is only the positive E-field direction, hence, the loop is a unipolar loop [11].

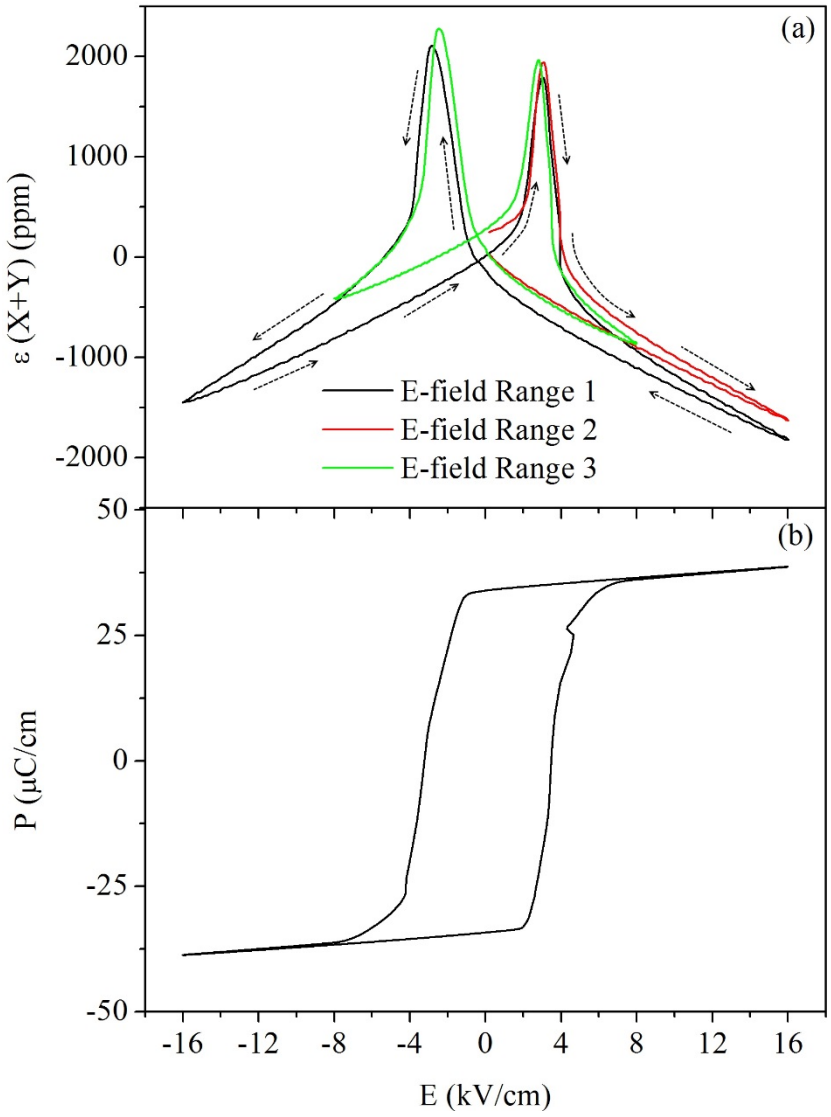

Fig. 7.3 [3] (a) In-plane piezoelectric strain loop of (011) oriented PMN-PT with the applied different E-field ranges: range 1 between -16 kV/cm and +16 kV/cm, range 2 between 0 kV/cm to +16 kV/cm and range 3 between – 8 kV/cm and + 8 kV/cm. (b). Ferroelectric hysteresis loop.

It is seen that the unipolar and bipolar ε-E loops depend on the applied E-field range. The strain value at the same E-field is different for the three different ranges. It also

[3] Data courtesy of Dr. Tian Ye

shows an obvious hysteresis characterization. Therefore, in this chapter, all samples were measured with the same applied E-field range (Range 2) to rule out any effect of the E-field range on the strain. In **Fig. 7.3** (b), the ferroelectric coercive field taken from the P-E loop is ~3.5 kV/cm and slightly higher compared to ~2 kV/cm reported previously [11], which results in the larger operational E-field up to around 16 kV/cm compared with the reported [12,13] 10 kV/cm for PMN-PT single crystal.

7.4 Electric field controlled magnetic properties

Fig. 7.4 and **Fig. 7.5** show the strong E-field dependence of the hysteresis loops measured along [01-1] and [100] in the 50 nm CoFe/x nm Ti/PMN-PT heterostructure (x = 0, 2, 4, 6, 8, 10), respectively. As we can see, the magnetization process along [01-1] becomes easy (**Fig. 7.4**), while the magnetization process along [100] becomes hard with the applied E-field (**Fig. 7.5**) in all samples.

The results can be qualitatively analysed by the strain induced domain wall motion. The magnetoelastic energy can be described as [14]:

$$E_{me} = (-3/2)\lambda\sigma\cos^2\theta \qquad (7.1)$$

Where λ and σ are the magnetostriction constant and stress, while θ is the angle between the saturation magnetisation (M_s) and σ. For minimizing the E_{me} in the system, the external E-field induces tensile strain (i.e. $\sigma > 0$) along [01-1], causing more magnetic moments to align along this tensile stress direction due to the positive λ. When the H-field is applied along [01-1], a lower H-field will be required to saturate the sample due to the relatively easy 180^o wall motion [14]. In contrast, the compressive stress ($\sigma < 0$) along [100] causes more magnetic moments to align

perpendicular to [100]. Thus, when the H-field is applied along [100], a higher H-field is required to rotate the magnetic moments 90^{o} into the [100] direction.

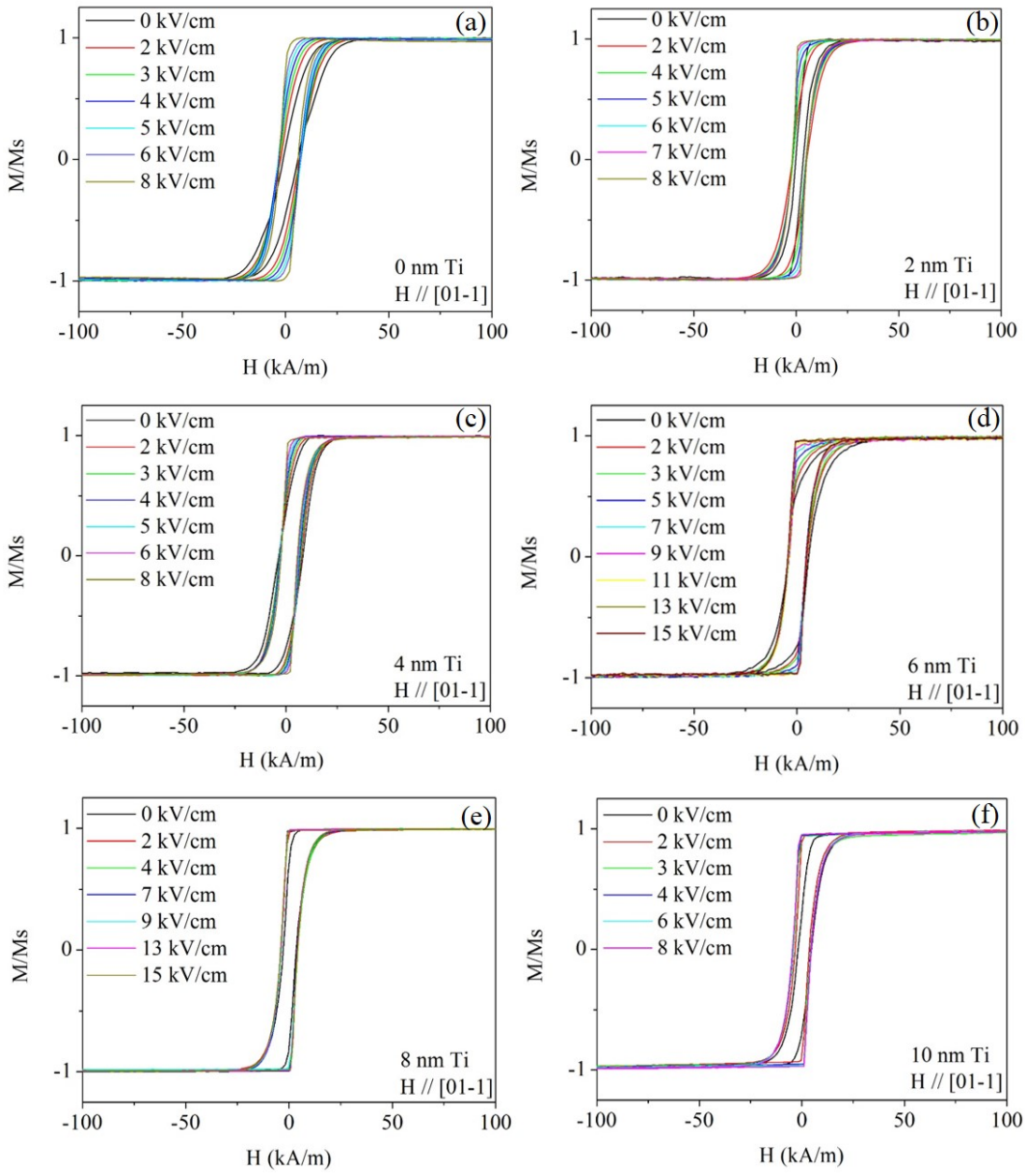

Fig. 7.4 Electric dependence of magnetic hysteresis loops measured along [01-1] in 50 nm CoFe/x nm Ti/PMN-PT heterostructures.

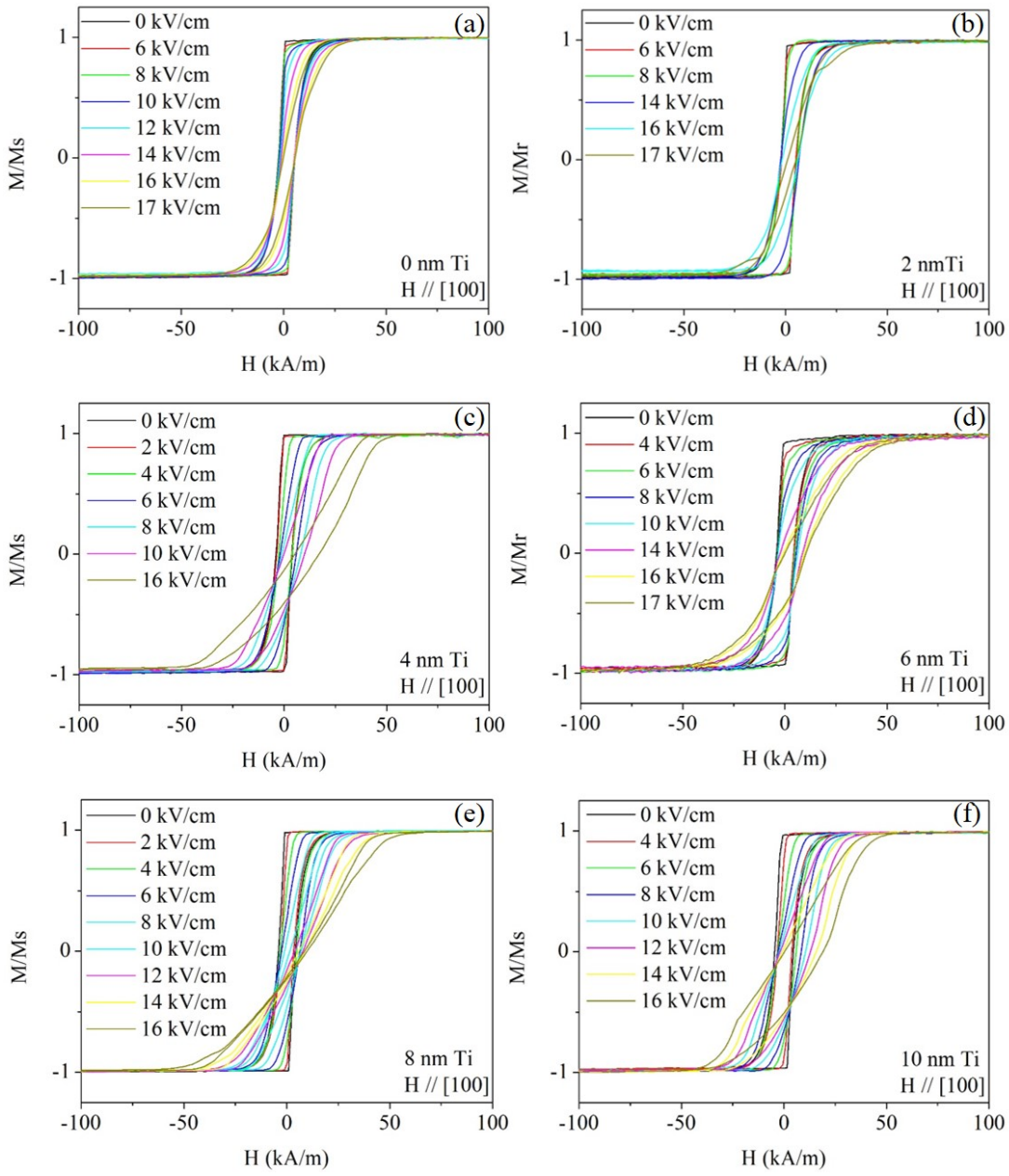

Fig. 7.5 Electric dependence of magnetic hysteresis loops measured along [100] in 50 nm CoFe/x nm Ti/PMN-PT heterostructures.

It is also seen that the magnetoelectric coupling strength (i.e. E-field induced magnetization change magnitude) depends on the different Ti layer thickness. Briefly, with increasing Ti layer thickness, the coupling strength increases gradually and achieves a maximum. In **Fig. 7.5**, it is clear that the E-field of 16 kV/cm or 17

kV/cm induced the higher and higher saturated field along [100] as the Ti layer thickness increases from 0 nm to 4 nm. More detailed analysis was carried out in **Fig. 7.6** & **Fig. 7.8**.

7.5 Magnetoelectric coupling strength manipulation

Fig. 7.6 shows the detailed variation in the M_r/M_s taken from the magnetic hysteresis loops (**Fig. 7.4** & **Fig. 7.5**) measured along [01-1] and [100] at each applied E-field in these heterostructures. When the E-field is increased, the M_r/M_s is increased along the [01-1] direction towards 1 and reduced along the [100] direction towards 0 in all the samples. As the E-field is increased further, the M_r/M_s along [01-1] is almost constant close to 1, while the M_r/M_s along [100] is decreased as the E-field is increased. At the E-field of 17 kV/cm, the maximum M_r/M_s change along [100] is 72% for the sample without Ti layer, corresponding the α of 1.0×10^{-6} s/m, while a larger M_r/M_s change of 100% is reached at the E-field of 16 kV/cm for the sample with 8 nm Ti layer, corresponding the α of 1.5×10^{-6} s/m. This suggests the addition of a Ti layer significantly improves the converse ME coupling strength.

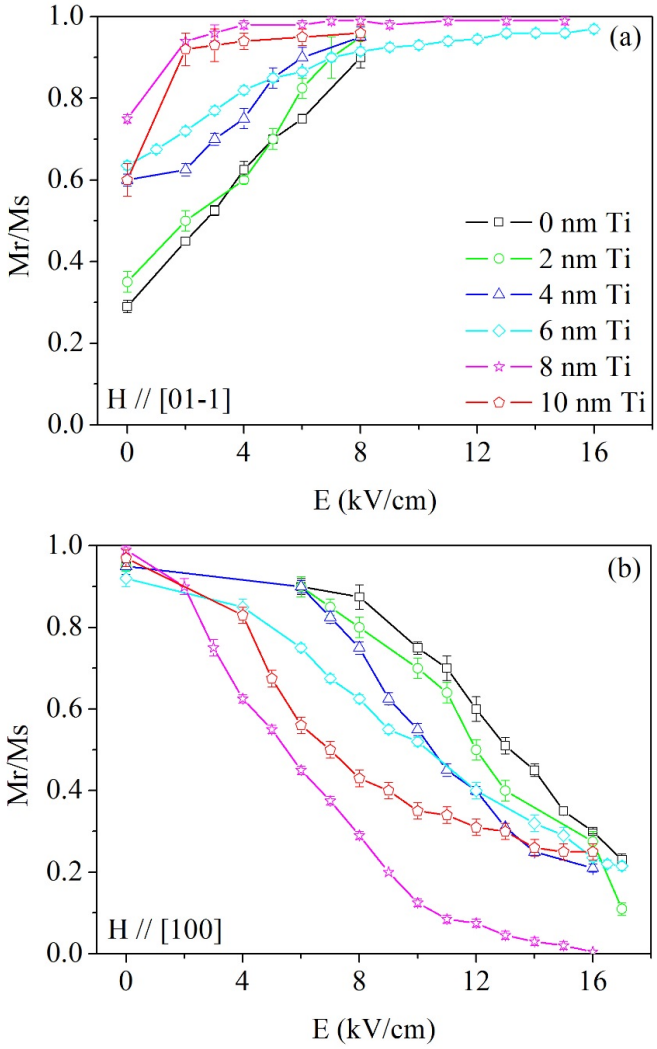

Fig. 7.6 (a) and (b) The normalized remanance (M_r/M_s) as a function of applied E-field in 50 nm CoFe/x nm Ti/PMN-PT heterostructure along [01-1] and [100], respectively.

In **Fig. 7.7**, the magnetoelectric coupling constant α at 9 kV/cm is shown for comparison and contrast with the results in Chapter 4. The maximum α of 2.1×10^{-6} s/m in the 50 nm CoFe/8 nm Ti/PMN-PT3 heterostructure is slightly smaller than that of 2.5×10^{-6} s/m in the 65 nm CoFe/PMN-PT2 (see section 4.5). The reason is due to a lower piezoelectric coefficient d_{31} of the PMN-PT3 substrate (see **Table 4.1**).

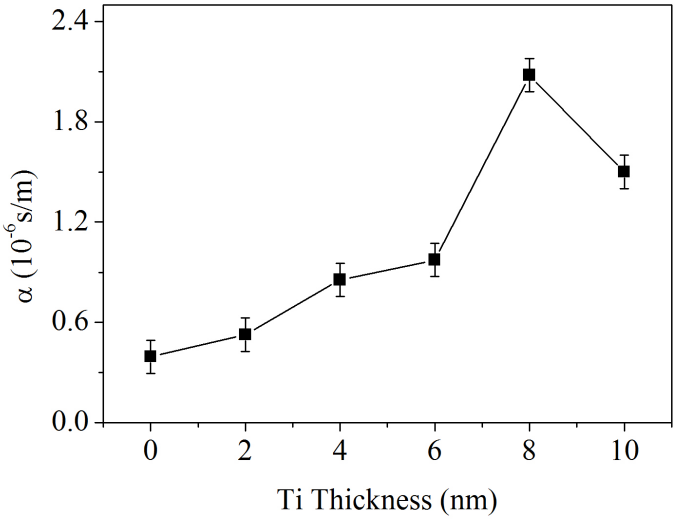

Fig. 7.7 The calculated magnetoelectric coupling constant α at 9 kV/cm for different Ti thickness. More information about α calculation can be found in section 5.5.

It is also observed that the E-field induced magnetization change difference between [01-1] and [100] under the E-field ranging from 0 kV/cm to 16 kV/cm due to the anisotropic strains along these two in-plane directions. In the low applied E-field range (i.e. 0-2 kV/cm), the M_r/M_s change is relatively larger along [01-1] than that along [100]. In 50 nm CoFe/10 nm Ti/PMN-PT heterostructure, the M_r/M_s measured along [01-1] increases from 0.6 to 0.9, while that change along [100] is the decrease from 0.98 to 0.9. The reason is that a tensile strain jump occurs at the 2 kV/cm, as shown in **Fig. 7.3** (a). In contrast, when the E-field is in the higher range from 4 kV/cm to 16 kV/cm, the total in-plane piezoelectric strain ε_{X+Y} becomes a compressive strain. Therefore, the M_r/M_s decrease along [100] is larger from 0.82 to 0.25 in this E-field range in the 50 nm CoFe/10 nm Ti/PMN-PT heterostructure.

The total magnetic energy (E_{total}) of the samples can be described as [13]:

$$E_{total} = E_{zeeman} + E_{ms} + E_{me} + E_{charge} + E_{uni} \quad (7.2)$$

where E_{zeeman}, E_{ms}, E_{me}, E_{charge} and E_{uni} are the Zeeman energy, magnetostatic energy, magnetoelastic energy, charging induced surface anisotropy energy and uniaxial magnetic anisotropy energy. In the present work, only the last three energy terms are changed.

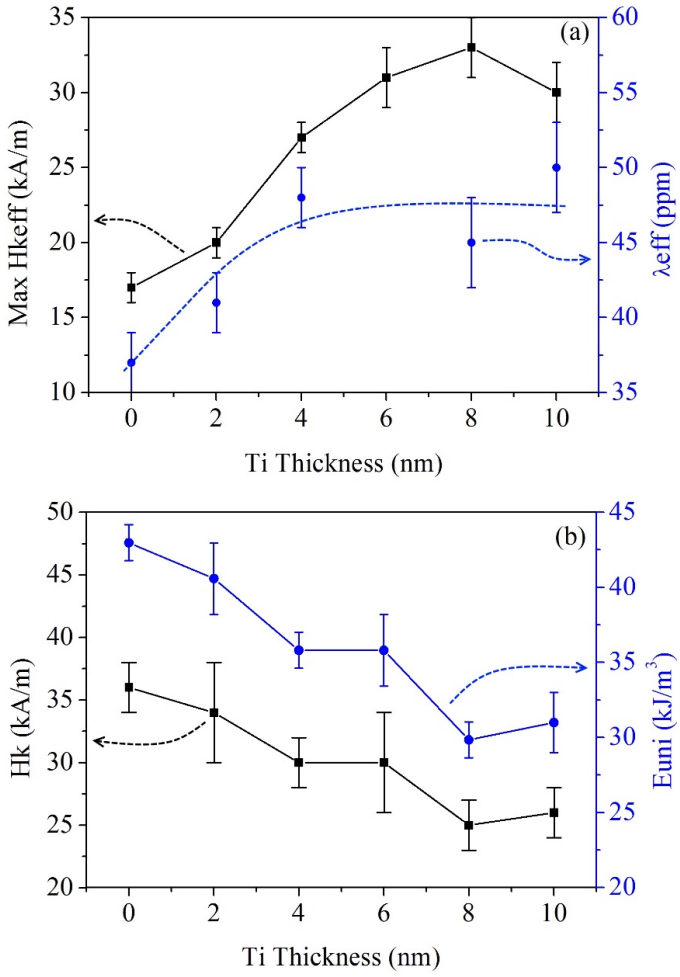

Fig. 7.8 (a) The E-field induced maximum effective anisotropy field H_{keff} and the effective saturation magnetostriction constant λ_{eff}. (b) The anisotropy field H_k without the applied E-field and the calculated E_{uni} for the different Ti thickness.

Firstly, when the conductive Ti layer is introduced into the interface between the CoFe and the PMN-PT substrate, the charge accumulation is hindered on the interface due to the metallic short charge screening length [13]. Therefore, E_{charge} is reduced in the sample with the addition of the Ti layer. Next, the E_{uni} without E-field can be calculated as [15]: $E_{uni} = (1/2)H_kM_s$, where the anisotropy field H_k is taken from the measured hysteresis loop at the $M/M_s = 1$ and shown in **Fig. 7.8** (b) and M_s is 1900 emu/cm^3 taken from the reference [16]. As shown in **Fig. 7.8** (b), when the Ti thickness increases, the E_{uni} is gradually reduced. For the sample without a Ti layer, the E_{uni} is 43 ± 1 kJ/m^3, while the E_{uni} is 29.8 ± 1 kJ/m^3 in the sample with 8 nm Ti. Therefore, the E_{uni} is reduced by 13.2 kJ/m^3 in the 8 nm Ti sample. The anisotropy change also can be clearly observed in **Fig. 7.9**, which shows the M_r/M_s measured along a series of angles between 0^o to 360^o for the 0 nm and 8 nm Ti samples.

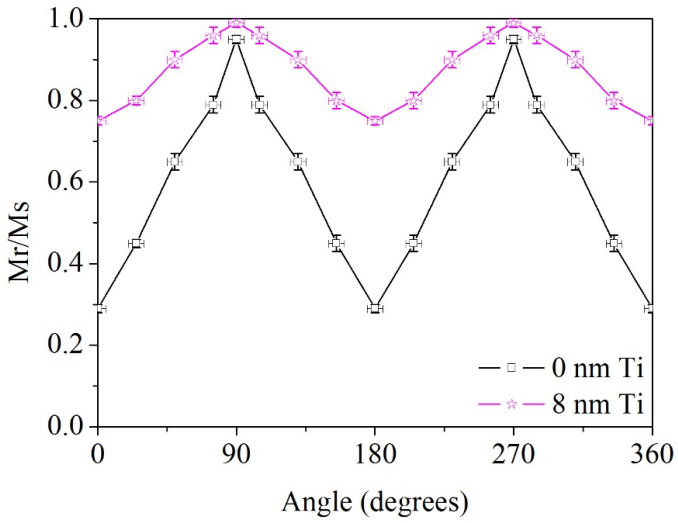

Fig. 7.9 The angular dependence of Mr/Ms for 0 nm Ti and 8 nm Ti. The 0^o corresponds to the [01-1] direction of PMN-PT substrate.

The other contribution to the ME coupling strength change by the Ti layer is the increasing E_{me} due to the varying λ with the varying Ti thickness. In a (110) textured film, the λ is given by $\lambda_{(110)} = (1/5)\lambda_{100} + (4/5)\lambda_{111} = 54$ ppm [10], while in a randomly orientated polycrystalline film, the λ is given by $\lambda_{isotropic} = (2/5)\lambda_{100} + (3/5)\lambda_{111} = 78$ ppm [10], where λ_{100} and λ_{111} are magnetostriction constant along the [100] and [111] of a single crystal, 150 ppm and 30 ppm respectively [17]. As discussed in the XRD results (**Fig. 7.1** (c)), the (110) texture exists in the sample without Ti layer, while the texture disappears in the sample with a Ti layer. Therefore, the λ can be altered due to the texture change in the CoFe film. The λ is estimated by measuring the same grown films on the Si substrate. As shown in **Fig. 7.8** (a), the effective saturation magnetostriction constant λ_{eff} increases from 37 ± 2 ppm to 48 ± 2 ppm, as the Ti layer thickness increases from 0 nm to 4 nm, similar to the increase in λ from (100) to random orientation as given above. However, when the thickness increases further, the λ_{eff} is almost constant. Based on the measured λ, the E_{me} can be deduced to be increase as $E_{me} = 3/2\lambda\varepsilon Y$ [15] , where Y is Young's modulus of CoFe. Therefore, the energy reduction of E_{charge} and E_{uni} and meanwhile the increase of E_{me} make the E_{me} contribution to the E_{total} dominant, thus produces the stronger converse ME coupling. Here, the E_{me} is only qualitatively discussed rather than precisely calculated because the ε measured in **Fig. 7.3** (a) is the total in-plane strain, i.e. ε_{x+y} but the separate ε_x and ε_y are needed to know for the calculation in the biaxial strain system.

7.6 The repeatability of the E-field controlled magnetization

To investigate the repeatability of the ME coupling, **Fig. 7.11** (a) & (b), only first 16 times magnetic hysteresis loops measured at the either 12 kV/cm or 14 kV/cm are

demonstrated because the other measured results are the same. Each magnetic hysteresis loop measurement takes about 30 seconds in the high H-field MOKE.

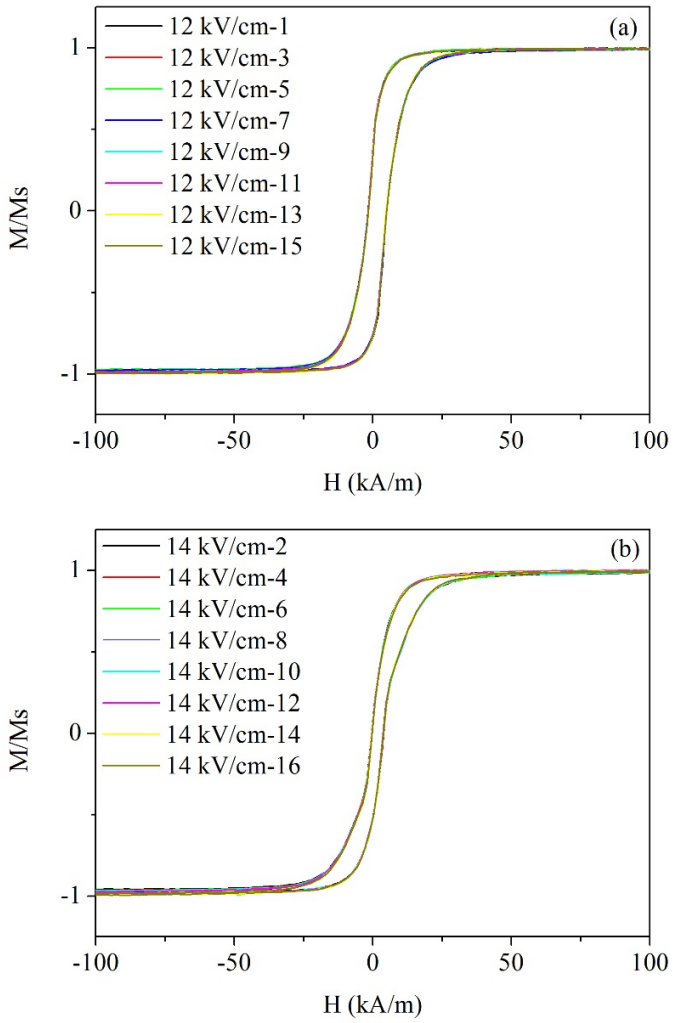

Fig. 7.10 Magnetic hysteresis loops measured repeatedly along [100] in the 50 nm CoFe/PMN-PT heterostructure when the alternative 12 kV/cm (a) and 14 kV/cm (b) were applied for 16 times.

The heterostructure shows a stable magnetization change between these high E-fields. In **Fig. 7.10**, the measured magnetic hysteresis loops at the either 12 kV/cm or 14

kV/cm are overlapped under more than ten times measurements. Firstly, it means that the strain hysteresis effect is almost negligible at the high E-field range, which is also observed in **Fig. 7.3** (a). Secondly, it suggests that the elastic coupling between the film and the substrate is strong and the strain is not relaxed gradually within many times repeated measurements, which can be attributed to a high-quality interface existing between the film and the substrate.

Fig. 7.11 (a)-(d) shows the magnetic properties change (taken from the magnetic hysteresis loops, as shown in **Fig. 7.10**) induced by E-field in the 50 nm CoFe/PMN-PT heterostructure, when the E-field is applied at 12 kV/cm, then at 14 kV/cm and repeated for 30 measurements. Other heterostructures with the Ti layer also show a similar repeatability.

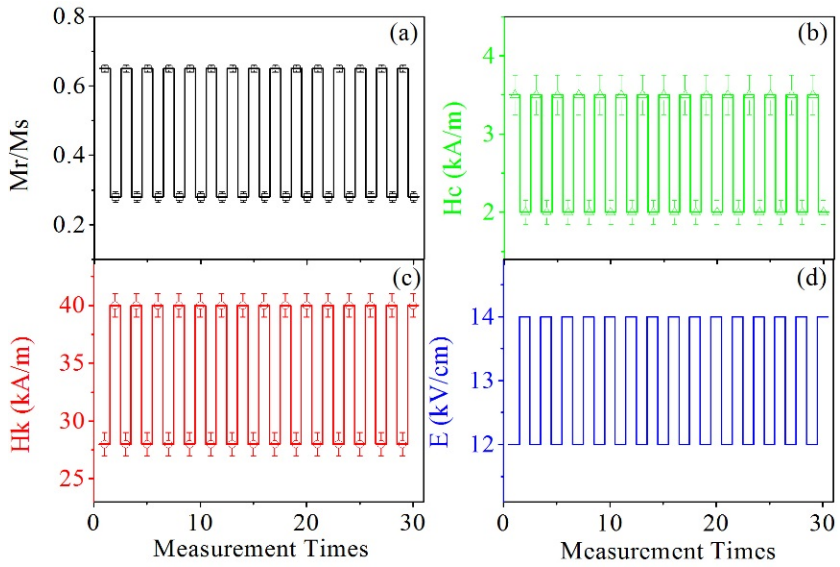

Fig. 7.11 Reproducible and quick magnetic property changes: M_r/M_s (a), H_c (b) and H_k (c) with the change of E-field (d).

Previously, the most dynamic E-field impulse induced magnetization change [13,18] was carried out at fields lower than 8 kV/cm for PMN-PT substrates due to the poor FE stability at the high E-field range. The results in this work suggests potential applications in high voltage handling capability and high output power devices [19].

7.7 Summary

In summary, the effect of the introduction of a Ti layer (0-10 nm) between a 50 nm $Co_{50}Fe_{50}$ layer and a (011) oriented PMN-PT substrate on the converse ME coupling strength was investigated. Both the interface structure and the film structure were altered by the Ti layer. A record high remanance ratio (M_r/M_s) tunability of 100% has been demonstrated in the 50 nm CoFe/8 nm Ti/PMN-PT heterostructure, when an E-field of 16 kV/cm was applied. Magnetic energy calculation showed that with increasing the Ti layer thickness the uniaxial magnetic anisotropy energy (E_{uni}) was reduced from 43 ± 1 kJ/m^3 to 29.8 ± 1 kJ/m^3. The reduction of E_{uni} makes the strain effect dominant in the total magnetic energy, thus gives an obvious enhanced ME coupling strength. In addition, these heterostructures also show good high-voltage stability suggesting potential applications in high voltage handling capability and high output power devices.

7.8 References

[1] S.X. Wang, N.X. Sun, M. Yamaguchi, S. Yabukami, Nature 407 (2000) 150–151.

[2] N.X. Sun, S.X. Wang, J. Appl. Phys. 92 (2002) 1477–1482.

[3] H.S. Jung, W.D. Doyle, IEEE Trans. Magn. 38 (2002) 2015–2017.

[4] J. Sayama, K. Mizutani, T. Asahi, T. Osaka, Appl. Phys. Lett. 85 (2004)

5640–5642.

[5] L.N. Zhang, J.F. Hu, J.S. Chen, J. Ding, J. Appl. Phys. 105 (2009) 07A743.

[6] A.V. Svalov, G.V. Kurlyandskaya, B. González Asensio, J.M. Collantes, A. Larrañaga, Mater. Lett. 152 (2015) 159–162.

[7] W.-G. Yang, N.A. Morley, J. Sharp, W.M. Rainforth, J. Phys. D. Appl. Phys. 48 (2015) 305005.

[8] H. Yan, F. Inam, G. Viola, H. Ning, H. Zhang, Q. Jiang, T. Zeng, Z. Gao, M.J. Reece, J. Adv. Dielectr. 01 (2011) 107–118.

[9] G. Viola, T. Saunders, X. Wei, K.B. Chong, H. Luo, M.J. Reece, Y. H, J. Adv. Dielectr. 3 (2013) 1350007.

[10] A. Javed, N.A. Morley, M.R.J. Gibbs, J. Magn. Magn. Mater. 321 (2009) 2877–2882.

[11] T. Wu, P. Zhao, M. Bao, A. Bur, J.L. Hockel, K. Wong, K.P. Mohanchandra, C.S. Lynch, G.P. Carman, J. Appl. Phys. 109 (2011) 124101.

[12] T. Fitchorov, Y. Chen, B. Hu, S.M. Gillette, A. Geiler, C. Vittoria, V.G. Harris, J. Appl. Phys. 110 (2011) 123916.

[13] T. Nan, Z. Zhou, M. Liu, X. Yang, Y. Gao, B.A. Assaf, H. Lin, S. Velu, X. Wang, H. Luo, J. Chen, S. Akhtar, E. Hu, R. Rajiv, K. Krishnan, S. Sreedhar, D. Heiman, B.M. Howe, G.J. Brown, N.X. Sun, Sci. Rep. 4 (2014) 3688.

[14] B.D. Cullity, C.D. Graham, Introduction to Magnetic Materials, Hoboken : Wiley, 2009.

[15] C.-J. Hsu, J.L. Hockel, G.P. Carman, Appl. Phys. Lett. 100 (2012) 092902.

[16] T.L. Jin, L. Hao, J.W. Cao, M.F. Liu, H.G. Dang, Y. Wang, D.P. Wu, J.M. Bai, F.L. Wei, Appl. Phys. Express 7 (2014) 043002.

[17] R.C. Hall, J. Appl. Phys. 31 (1960) S157–S158.

[18] M. Liu, Z.Y. Zhou, T.X. Nan, B.M. Howe, G.J. Brown, N.X. Sun, Adv. Mater. 25 (2013) 1435–1439.

[19] Z. Hu, T. Nan, X. Wang, M. Staruch, Y. Gao, P. Finkel, N.X. Sun, Appl. Phys. Lett. 106 (2015) 022901.

Chapter 8

8 Summary and Future Work

An optimal RF sputtering power (P) for soft magnetic properties was explored in both CoFe/Si heterostructures and CoFe/Metglas/Si heterostructures. The coercive field was increased when the sputtering power P increased from 75 W to 200 W in both heterostructures. Therefore, the sputtering power 75 W was used in the rest of the work.

Firstly, a single layer CoFe film was deposited on the (011) PMN-PT substrate. The CoFe film thickness (from 30 nm to 100 nm) effect on the magnetoelectric coupling was investigated. The magnetoelectric constant (α) has been improved by reducing the magnetic layer thickness in the multiferroic heterostructures. A large remanance ratio (M_r/M_s) tunability of 95% has been demonstrated in the 65 nm CoFe/(011) PMN-PT heterostructure, corresponding to a giant magnetoelectric constant α of 2.5 × 10^{-6} s/m, when an external electric field (E-field) of 9 kV/cm was applied. Moreover, a large E-field induced effective magnetic anisotropy field (H_{eff}) of 38.2 kA/m was also observed in this heterostructure.

Secondly, bilayered magnetic films (CoFe/Metglas) were deposited on either (001) PMN-PT or (011) PMN-PT substrate. A larger magnetoelectric constant α = 2.9 × 10^{-6} s/m was demonstrated in the 30 nm CoFe/12 nm Metglas/(011) PMN-PT heterostructure due to the improved λ and reduced magnetic layer thickness. More interestingly, a non-volatile magnetization change was demonstrated in the 65 nm CoFe/24 nm Metglas/(001) PMN-PT heterostructure. Two bistable magnetization

states could be reversibly controlled by an E-field. Based on the giant magnetoresistance (GMR) effect or anisotropic magnetoresistance (AMR) effect, the magnetoelectric random access memory (MERAM) memory cell was proposed for the fast, low-power and high-density information storage.

Finally, a thin Ti buffer layer (0-10 nm) effect on the magnetoelectric coupling was investigated. A record high remanence ratio (M_r/M_s) tunability of 100% was demonstrated in the 50 nm CoFe/8 nm Ti/(011) PMN-PT heterostructure, when a total in-plane piezoelectric strain of -1821ppm was applied at an E-field of 16 kV/cm. Magnetic energy calculation showed that with increasing the Ti layer thickness the uniaxial magnetic anisotropy energy (E_{uni}) was reduced from 43 ± 1 kJ/m^3 to 29.8 ± 1 kJ/m^3. The reduction of E_{uni} made the strain effect dominant in the total magnetic energy, thus gave an enhancement in the ME coupling strength.

The following future work has been proposed:

- ✓ More mechanism studies of magnetization change by the E-field is required. In this thesis, film thickness is above 10 nm, but for films thinner than 10 nm, the interfacial coupling mechanism can be not negligible. Hence other coupling mechanisms need to be taken into account.
- ✓ Electric field controlled magnetization change within nanostructured patterns still has to be investigated for practical applications. For example, is it feasible to control magnetic properties of each pattern independently? If so, this will be a big progress for really magnetoelectric memory.
- ✓ In this thesis, the non-volatile magnetization change was demonstrated. However, the magneto-transport measurements have not been done for electrically reading out the magnetization change within practical applications.

Hence, the magnetoresistance measurements (GMR or AMR) have to be done in future.